UNIVERSITY OF CALIFORNIA

Los Angeles

Exploring Novel Uses of Size-Fractionated Nanoemulsions

A dissertation submitted in partial satisfaction of the

requirements for the degree Doctor of Philosophy

in Chemistry

by

Matthew James Pagenkopp

2019

ABSTRACT OF THE DISSERTATION

Exploring Novel Uses of Size-Fractionated Nanoemulsions

by

Matthew James Pagenkopp

Doctor of Philosophy in Chemistry

University of California, Los Angeles, 2019

Professor Thomas G. Mason, Chair

Oil-in-water nanoemulsions are aqueous dispersions of oil which have $a < 100$ nm and are an intriguing model system to study fundamental chemical and physical science. Nanoemulsions have a broad range of utilities and applications, not only in academic research, but in industry as well. Due to the small size of droplets inherent in nanoemulsions, they have an incredibly large surface area-to-volume ratio. This small droplet size also leads to decreased multiple scattering, even at large volume fractions, which can yield translucent elastic solids. In this dissertation, we present methods to measure the thermodynamic partitioning of sodium dodecyl sulfate molecules in nanoemulsions between the aqueous phase and oil-water interface, as well as an exciting novel route to produce crystalline and non-crystalline photonic size-fractionated nanoemulsions. Both

gravimetric and electrical conductivity measurement analyses have been developed which can accurately determine what fraction of the total surfactant in both unfractionated and size-fractionated nanoemulsion resides on the oil-water interface or in the bulk continuous phase as either monomer or micelles. A theory of this partitioning, based off the Langmuir isotherm, has been developed and is presented in terms relevant to emulsion science. Furthermore, through a process of both hot emulsification and competitive surfactant exchange, we have developed methods where poorly screened ultrastable nanoscale liquid droplets can self-assemble to form brilliant opals, where the Debye layer λ_D is greater than the diameter of the droplet ($a/\lambda_D < 1$). This poorly screened ultrastable nanoemulsion can also form non-crystalline hyperuniform structures where intense monochromatic colors are observed in backscatter, without the addition of any optically absorbing chemicals or compounds.

The dissertation of Matthew James Pagenkopp is approved.

Dolores Bozovic

James W. Gober

Thomas G. Mason, Committee Chair

University of California, Los Angeles

2019

To my fiancée Laura, family, friends, and people who have supported me.

TABLE OF CONTENTS

LIST OF FIGURES viii

LIST OF TABLES xi

ACKNOWLEDGMENTS xii

VITA xiv

PUBLICATIONS xv

Chapter 1 – Introduction 1

1.1 Emulsification and Nanoemulsions 1

1.2 Reducing Nanoemulsion Size Polydispersity 2

1.3 Advantages of Monodisperse Nanoemulsions 3

1.3.1 Surfactant Adsorption 3

1.3.2 Photonic Nanoemulsions 5

References 7

Chapter 2 – Surfactant Partitioning in Nanoemulsions 10

2.1 Introduction 10

2.2 Theory 15

2.3 Materials and Methods 19

2.3.1 Common Procedures 19

2.3.2 Procedures for Fractionated Nanoemulsions 21

2.3.3 Procedures for Unfractionated Nanoemulsions 26

2.3.4 Interfacial Tension Measurements 28

2.4 Results 28

2.4.1 Gibbs Isotherm 28

2.4.2 Adsorption Isotherm: Fractionated NEMs 30

2.4.3 Adsorption Isotherm: Unfractionated NEMs 31

2.5 Discussion 35

2.6 Conclusion 44

References 47

Chapter 3 – Hyperuniform Photonic Nanoemulsions and Biliquid Opals 51

3.1 Introduction 51

3.2 Results 52

3.3 Discussion 63

3.4 Methods 65

Appendix A – Supplementary Information for Chapter 3 79

Additional Discussion 79

Extended Data Figures and Table 83

References 93

Chapter 4 – Summary and Future Directions 97

LIST OF FIGURES

Figure 2.1. Schematics of analytical procedures used to measure the final bulk surfactant concentration, $C_{b,f}$, of an ionic amphiphile in oil-in-water nanoemulsions. 23

Figure 2.2. Calibration results for the massing of precipitated $Sr(DS)_2$ and the conductivity of dissociated SDS in aqueous solution. 25

Figure 2.3. Interfacial tension measurements of PDMS oil and aqueous SDS solutions. 29

Figure 2.4. Raw and adjusted equilibrium adsorption isotherm of dodecyl sulfate anions onto water–silicone oil (poly(dimethylsiloxane)) interfaces obtained from the final surface concentration $C_{s,f}$ and final bulk concentration $C_{b,f}$ measured using a fractionated nanoemulsion. 31

Figure 2.5. Partitioning of DS^- to droplet interfaces in unfractionated PDMS oil/water nanoemulsions after HFRE and equilibration. 33

Figure 2.6. Comparison of equilibrium adsorption isotherms for dodecyl sulfate anions onto PDMS silicone oil–water interfaces for both fractionated and nonfractionated NEM systems. 34

Figure 2.7. Final bulk DS^- concentration, $C_{b,f}$, calculated using eq 2.7 as a function of the bulk initial DS^- concentration, $C_{b,i}$. K and $C_s°$ values are from the fit to the adjusted isotherm in Figure 2.4. 41

Figure 2.8. Adsorbed fraction f_{ads} of DS^- on PDMS oil/water droplet interfaces after HFRE calculated using eq 2.7 and $f_{ads} = 1 - (C_{b,f}/C_{b,i})$ for fixed $C_{b,i} = C^* = 8.1$ mM and values of K and $C_s°$ from the fit to the adjusted isotherm in Figure 2.4. 43

Figure 3.1 Photonic crystalline and non-crystalline hyperuniform structures of ultrastable fractionated ionic oil-in-water (O/W) nanoemulsions. 53

Figure 3.2 Controlling backscattered colors of crystalline biliquid opals through the volume fraction ϕ and average droplet radius $<a>$ of fractionated nanoemulsions. 57

Figure 3.3 Tuning photonic nanodroplet structures through ionic strength I and pH in the aqueous continuous phase of ultrastable fractionated nanoemulsions. 59

Figure 3.4 Kinetics of crystallite formation in monochromatic and bichromatic biliquid opals following dilution and ultrasonic mixing. 61

Figure S3.1 Centrifugal deionization probes nanodroplet stability against coalescence for sodium alkylsulfates having different carbon-numbers. 83

Figure S3.2 Centrifugal deionization decreases the electrical conductivity σ_e of nanoemulsions and their continuous phase solutions. 84

Figure S3.3 Iridescence of biliquid opals. 85

Figure S3.4 Repeated centrifugal fractionation reduces the polydispersities of nanoemulsions produced by multi-pass high flow-rate emulsification. 86

Figure S3.5 Optical backscattering spectrum of a biliquid opal showing a hyperuniform crystalline peak in the ultraviolet. 87

Figure S3.6 Ultrasonic destruction of nanoemulsion crystallites in a biliquid opal and subsequent crystallite regrowth. 88

Figure S3.7 Out-of-equilibrium temporal evolution of a deionized fractionated nanoemulsion concentrate that is added to deionized water. 89

Figure S3.8 Uniform structural colors of polydisperse unfractionated photonic nanoemulsions that remain disordered despite deionization. 90

Figure S3.9 Color mixing rules for non-crystalline hyperuniform photonic nanoemulsions violate mixing rules commonly taught for absorbing colors. 91

LIST OF TABLES

TABLE S3.1 Characteristics of deionized nanoemulsion concentrates. 92

ACKNOWLEDGMENTS

This dissertation and the research required to complete it would not have been possible without the support of people close to me. As my graduate studies come to an end, I would like to take this opportunity to show my appreciation to those who have inspired and encouraged me through this lengthy process.

I would like to start by thanking my advisor, Dr. Thomas G. Mason. I cannot overstate his help in my graduate career. The vast majority of the knowledge and practical skills I have learned at UCLA have come from our countless discussions and conversations over the years. I would not be here without his insight, encouragement, and guidance. I am grateful for all of our discussions on research, life, and physical chemistry. I truly appreciate the time he has taken to help better my critical thinking, scientific writing, and figure preparation. His attention to detail and standards has given me the opportunity to grow and better myself as a person and scientist. I am very honored to have been a part of his research group.

I want to thank Dr. Dolores Bozovic, Dr. Jeffrey I. Zink, and Dr. James W. Gober for serving on my committee and for their insightful comments and questions pertaining to my research. I would like to thank Dr. James W. Gober and Dr. Anne Hong-Hermesdorf for requesting me as a TA during the majority of my summer sessions and regular school year respectively. Not only was teaching for both of you very instructive and I learned a lot, it was also incredibly fun and I have enjoyed it immensely.

I am honored to have had the opportunity to work with the amazing lab members from Tom's group. I will always cherish the amazing times we had whether it was grabbing a bite to eat, working in lab, or discussing our latest research results. I would like to thank Prof. Manas

Khan, Dr. Ha Seong Kim, Dr. Dimitri Bikos, Dr. Po-Yuan Wang, Mr. Orin Yue, Miss Yixuan Xu, Mr. Tianren Yu, Mr. Edgar Elias, and Mr. Sean Tsai. I would like to extend a special thanks to Dr. Ha Seong Kim for being an amazing friend and our countless discussions which have been of great benefit to me and my research.

I would also like to thank my parents, brother, sister, and grandparents who have supported and encouraged me throughout this process. I would like to extend my sincerest love and appreciation to my fiancée, Laura, whose constant support and understanding have been very appreciated throughout this process. Without any of these people in my life, I would not have been able to complete my doctoral degree.

VITA

2011-2013 Cooperative education intern, The Metropolitan Water District of Southern California, La Verne, California

2013 Bachelor of Science, Chemistry, California State Polytechnic University Pomona, Pomona, California

2015 Masters of Science, University of California Los Angeles, Los Angeles California

PUBLICATIONS

1. **Pagenkopp, M. J.**, Mason, T.G. Hyperuniform Photonic Nanoemulsions and Biliquid Opals, submitted to *Nature*
2. **Pagenkopp, M. J.**, Mason, T. G. Surfactant Partitioning in Nanoemulsions, *Langmuir*, **34**, 10309-10320 (2018).
3. Rogers, M. C., Chen, K., **Pagenkopp, M. J.**, Mason, T. G., Narayanan, S., Harden, J. L., Leheny, R. L. Microscopic Signatures of Yielding in Concentrated Nanoemulsions under Large-Amplitude Oscillatory Shear. *Physical Review Materials* **2**, (2018).
4. Braibanti, M., Kim, H. S., Senbil, N., **Pagenkopp, M. J.**, Mason, T. G., Scheffold, F. The Liquid-Glass-Jamming Transition in Disordered Ionic Nanoemulsions. *Scientific Reports* **7**, (2017).

Chapter 1 – Introduction

1.1 Emulsification and Nanoemulsions

Emulsions have found their way into everyday life and can be found in items such as medication, cosmetics, and food. Emulsions are produced by dispersing one immiscible liquid, called the dispersed phase, in another liquid, called the continuous phase.[1] Unlike lyotropic liquid crystals, swollen micelles, and other microemulsions; emulsions do not form spontaneously and are not thermodynamically stable.[1-4] The droplets in an emulsion are able to coalesce (at least two droplets combine to form one larger droplet) and if enough of these coalescence events occur, the disperse phase and continuous phase will macroscopically separate. In order to prevent coalescence, surfactants (amphiphilic molecules) are added to the emulsion which provide a repulsive force to the droplet interfaces and kinetically stabilize the droplets. These surfactants can also lower the interfacial tension, by adsorbing onto the interface, which facilitates droplet rupturing and smaller droplet formation.

By increasing the shear while emulsifying and having a sufficient amount of surfactant molecules available to adsorb onto newly formed interfaces, droplets with radii $a < 100$ nm (nanoemulsions, NEMs) can be produced. These large shear forces are typically achieved by using a high flow rate emulsification techniques (HFRE, homogenizer[5-8] and ultrasonication[9,10]). There are other methods to form nanoscale droplets (e.g. evaporative ripening[5] and phase inversion temperature method[11,12]) however, HFRE tends to be the simplest and most direct route to make nanoemulsions. While there are many combinations of disperse phase liquids, continuous phase liquids, and surfactants which can be used to construct stable nanoemulsions, this thesis will focus

on oil-in-water (O/W) nanoemulsions where 10 cSt poly(dimethylsiloxane) (PDMS) oil is dispersed in a surfactant solution (single chain alkylsulfate with the general formula $C_xH_ySO_4^-$).

1.2 Reducing Nanoemulsions Size Polydispersity

The nanoemulsions created by HRFE techniques are polydisperse, the standard deviation of the size distribution δa divided by the average hydrodynamic radii $\langle a \rangle$ is typically $0.5 \leq \delta a/\langle a \rangle \leq 0.7$.[6] This initial polydispersity can be decreased by multiple passes through a homogenizer, where the droplets will be constantly ruptured and coalesced with each pass, however $\delta a/\langle a \rangle > 0.5$.[6] While other technologies exist which can produce highly monodisperse droplets (e.g. microfluidic devices[13,14]), these droplets are micron sized and would therefore only be able to make monodisperse emulsions, not nanoemulsions.

In order to decrease the size polydispersity of nanoemulsions, centrifugal fractionation can be used. First described by Perrin[15], centrifugal fractionation (what Perrin called fractional centrifugation) takes advantage of the fact that droplets with different a will have different sedimentation rates (or creaming rates if the disperse phase has a smaller density ρ than the continuous phase) which are related to the droplet's a. This leads to a gradient in droplet a for the resulting cream (solid elastic plug which forms at the top of the centrifuge tube for PDMS O/W NEMs, $\rho_{PDMS} < \rho_{water}$) which is physically cut to select for droplets with a specific a.[3] Through subsequent fractionation steps, the size polydispersity is reduced and nanoemulsions with low polydispersity ($0.07 \leq \delta a/\langle a \rangle \leq 0.2$ for three or more fractionation steps, see Chapter 3 Table S3.1) can be produced.

1.3 Advantages of Monodisperse Nanoemulsions

Due to the lengthy process and specialized equipment needed to size-fractionate nanoemulsions, many studies have been done with polydisperse nanoemulsions. The physical phenomena discussed in this dissertation would not have been possible without the ability to size fractionate nanoscale droplets and greatly reduce the droplets size polydispersity. By decreasing the size distribution, a measured $\langle a \rangle$ can be used to reasonably calculate the total interfacial area of the nanoemulsion. This allowed for a more accurate study and an intriguing look at surfactant partitioning during emulsification. These monodisperse nanodroplets are also used to create brilliant biliquid opalescent crystals, similar in brilliance to colloidal crystals made from charge stabilized polymer nanoparticles. Many more interesting physical properties of this size-fractionated high surface area material have yet to be explored and studied.

1.3.1 Surfactant Adsorption

The continuous phase is often viewed as a reservoir which contains the majority of the surfactant molecules after emulsification, however this assumption may not hold true for nanoemulsions. During HFRE, when micron-sized droplets are ruptured to the nanoscale, there is a large increase in both the number of droplets and interfacial area of the newly formed nanoemulsion. This increase in interfacial area could potentially affect the thermodynamic partitioning of surfactant molecules as monomers and micelles in the continuous phase as well as surfactant molecules that have adsorbed onto droplet interfaces. Depending on the amount of interfacial area created, the final surfactant concentration in the bulk, $C_{b,f}$, could be vastly lower than the initial surfactant concentration, $C_{b,i}$. By conserving the mass of the surfactant throughout the emulsification process, the amount of surfactant on the droplet interfaces at equilibrium must

be: $C_{s,f} = [(C_{b,i}-C_{b,f})V_b]/A_{s,f}$, where V_b is the volume of the continuous phase in which all of the nonadsorbed surfactant is assumed to reside and $A_{s,f}$ is the total interfacial area of all of the nanodroplets after HFRE.

Many methods have been created and used to measure surfactant adsorption onto different liquid-liquid interfaces Neutron reflection has been used to measure the surface concentration of fatty acids and triblock copolymers on a flat hexane-water interface.[16] Small-angle neutron scattering has been used to probe the surface densities of micron-sized droplets which is related to the surface concentration.[17] Another method to measure surfactant adsorption is measuring the interfacial tension of the macroscopic liquid-liquid interface as a function of surfactant concentration then determine the surface coverage through the Gibb's derivative.[18,19] A significant drawback of this methods is its deviation at large concentrations of surfactant where chemical potential and concentration diverge.

Surfactant adsorption on the highly curved interface of nanodroplets could differ from a relatively flat interface, especially if the droplet's *a* approaches the effective size of the surfactant. A method which can be applied to smaller droplets and does not rely on beam-line access or the Gibb's derivative is a methylene blue dye complexation method. An emulsion is filtered and the anionic surfactant (sodium dodecyl sulfate, SDS) in the droplet-free continuous phase is complexed with the cationic methylene blue dye.[20] The charge neutral methylene blue-dodecyl sulfate complex is extracted into chloroform where its concentration is determined by visible spectroscopy.[21-24] This method has its drawbacks as it uses a polydisperse (unfractionated) nanoemulsion, droplets have a broad size distribution, which decreases the ability to accurately determine the total interfacial area.

We have designed a new experimental method to measure surfactant adsorption and partitioning of the anionic surfactant sodium dodecyl sulfate on the interfaces of O/W nanoemulsions which have been made by HFRE and size-fractionated. Size-fractionated nanoemulsions have a better characterized total interfacial area due to having a lower polydispersity than unfractionated nanoemulsions. Furthermore we used gravimetric and electrical conductivity analyses to directly measure the total amount of surfactant (combined $C_{b,f}$ and $C_{s,f}$) and the amount of surfactant in the droplet-free continuous phase ($C_{b,f}$) respectively. We show that sodium dodecyl sulfate adsorption onto nanoemulsion water-silicone oil interfaces can be described by a Langmuir isotherm yielding a maximum surface concentration, C_s^o, and an equilibrium constant, K. The combination of relatively simple macroscopic bulk measurements can be used to determine useful information about the thermodynamic energetics and equilibrium adsorption reaction of amphiphiles on oil-water interfaces.

1.3.2 Photonic Nanoemulsions

In typical oil-in-water nanoemulsions, surfactant molecules that adsorb onto the oil-in-water interface are in thermodynamic equilibrium with the surfactant molecules in the continuous phase. If there is a significant decrease in the continuous phase's surfactant concentration, then the amount of surfactant which remains on the interface will not be large enough to prevent coalescence. By using surfactants with a more hydrophobic chain (e.g. increasing the chain length) the adsorption equilibrium will shift towards surfactants adsorbing onto the oil-water interface. An issue with this approach is the surfactant molecule needs to be dissolved in the aqueous continuous phase to adsorb onto the oil-in-water interface. This can be overcome by heating the emulsion components during emulsification and homogenization (as long as the surfactant dissolves below the boiling point of the aqueous or oil phase). Another potential route is to replace a short aliphatic

carbon chain surfactant, in a size-fractionated nanoemulsion, with a longer aliphatic carbon chain surfactant is through a process of competitive adsorption. The nanoemulsion is heated to dissolve the long chain surfactant which can then readily adsorb onto the oil-water interface, displacing some of the short chain surfactant. The nanoemulsion is then allowed to cool to room temperature. The long chain surfactants are effectively prevented from desorbing due to the decrease in desorption rate caused by the decrease in temperature. The short aliphatic chain surfactant can be removed by repeated dilutions, leaving only the poorly soluble long aliphatic chain surfactant on the interface.

The combination of low polydispersity size-fractionated nanoemulsions and a low ionic strength continuous phase provides a unique opportunity to study a new material. We observe unique and interesting photonic properties of this ultra-stable nanoemulsion after substantial deionizing and diluting with deionized water. The monodisperse poorly screened droplets are able to assemble to form millimeter scale crystallites which scatter light akin to natural gemstone opals[25,26] (which are an ordered array of silica spheres). Furthermore, non-crystalline hyperuniform[27] states are also observed where the nanoemulsion has an intense monochromatic visible color in backscatter.

References

1 Fryd, M. M. & Mason, T. G. Advanced Nanoemulsions. *Annu. Rev. Phys. Chem.* **63**, 493-518, (2012).

2 McClements, D. J. Nanoemulsions *versus* Microemulsions: Terminology, Differences, and Similarities. *Soft Mater.* **8**, 1719-1729 (2012).

3 Mason, T. G., Wilking, J. N., Meleson, K., Chang, C. B. & Graves, S. M. Nanoemulsions: Formation, Structure, and Physical Properties. *J. Phys.: Condens. Matter* **18**, R635-R666 (2006).

4 Anton, N. & Vandamme, T. F. Nono-Emulsions and Micro-Emulsions: Clarifications of the Critical Differences. *Pharm. Res.* **28**, 978-985 (2010).

5 Fryd, M. M. & Mason, T. G. Time-Dependent Nanoemulsion Droplet Size Reduction by Evaporative Ripening. *J. Phys. Chem. Lett.* **1**, 3349-3353 (2010).

6 Meleson, K., Graves, S. & Mason, T. G. Formation of Concentrated Nanoemulsions by Extreme Shear. *Soft Mater.* **2**, 109-123, (2004).

7 Lee, S. J. & McClements, D. J. Fabrication of Protein-Stabilized Nanoemulsions Using a Combined Homogenization and Amphiphilic Solvent Dissolution/Evaporation Approach. *Food Hydrocoll.* **24**, 560-569 (2010).

8 Wooster, T. J., Golding, M. & Sanguansri, P. Impact of Oil Type on Nanoemulsion Formation and Ostwald Ripening. *Langmuir* **24**, 12758-12765 (2008).

9 Abismail, B., Canselier, J. P., Wilhelm, A. M. & Gourdon, C. Emulsification by Ultrasound: Drop Size Distribution and Stability. *Ultrason. Sonochem.* **6**, 75-83 (1999).

10 Leong, T. S. H., Wooster, T. J., Kentish, S. E. & Ashokkumar, M. Minimizing Oil Droplet Size Using Ultrasonic Emulsification. *Ultrason. Sonochem.* **16**, 721-727 (2009).

11 Izquierdo, P. *et al.* Formation and Stability of Nano-Emulsions Prepared Using the Phase Inversion Temperature Method. *Langmuir* **18**, 26-30 (2002).

12 K., S. H. S. The Stability of O/W Type Emulsions as Functions of Temperature and the HLB of Emulsifiers: The Emulsification by PIT-Method. *J. Colloid Interface Sci.* **30**, 258-263 (1969).

13 Anna, S. L., Bontoux, N. & Stone, H. A. Formation of Dispersions Using "Flow Focusing" in Microchannels. *Appl. Phys. Lett.* **82**, 364-366 (2003).

14 Zhu, P. & Wang, L. Passive and Active Droplet Generation with Microfluidics: A Review. *Lab Chip* **17**, 34-75 (2016).

15 Perrin, J. *Atoms*. (D. Van Nostrand Company, 1916).

16 Cosgrove, T., Phipps, J. S. & Richardson, R. M. Neutron reflection from a liquid/liquid interface. *Colloids Surf. A* **62**, 199-206 (1992).

17 Staples, E., Penfold, J. & Tucker, I. Adsorption of Mixed Surfactants at the Oil-Water Interface. *J. Phys. Chem. B* **104**, 606-614 (2000).

18 Kanellopoulos, A. & Owen, M. Adsorption of Sodium Dodecyl Sulphate at Silicone Fluid/Water Interface. *Trans. Faraday Soc.* **67**, 3127 (1971).

19 Martínez-Balbuena, L., Arteaga-Jiménez, A., Hernández-Zapata, E. & Márquez-Beltrán, C. Applicability of the Gibbs Adsorption Isotherm to the Analysis of Experimental Surface-Tension Data for Ionic and Nonionic Surfactants. *Adv. Colloid Interface Sci.* **247**, 178-184 (2017).

20 James-Smith, M. A., Alford, K. & Shah, D. O. A Novel Method to Quantify the Amount of Surfactant at the Oil/Water Interface to Determine Total Interfacial Area of Emulsions. *J. Colloid Interface Sci.* **310**, 590-598 (2007).

21 Carroll, M. K. *et al.* Interactions Between Methylene Blue and Sodium Dodecyl Sulfate in Aqueous Solution Studied by Molecular Spectroscopy. *Appl. Spectrosc.* **53**, 780-784 (1999).

22 Jurado, E., Fernandez-Serrano, M., Nunez-Olea, J., Luzon, G. & Lechuga, M. Simplified Spectrophotometric Method Using Methylene Blue for Determining Anionic Surfactants: Applications to the Study of Primary Biodegradation in Aerobic Screening Tests. *Chemosphere* **65**, 278-285 (2006).

23 Mukerjee, P. Use of Ionic Dyes in the Analysis of Ionic Surfactants and Other Ionic Organic Compounds. *Anal. Chem.* **28**, 870-873 (1956).

24 Zaghbani, N., Hafiane, A. & Dhahbi, M. Separation of Methylene Blue from Aqueous Solution by Micellar Enhanced Ultrafiltration. *Sep. Purif. Technol.* **55**, 117 (2007).

25 Sanders, J. V. Colour of Precious Opal. *Nature* **204**, 1151-1153 (1964).

26 Sanders, J. V. Diffraction of Light by Opals. *Acta Cryst. A* **24**, 427-434 (1968).

27 Torquato, S. Hyperuniform States of Matter. *Phys. Rep.* **745**, 1-95 (2018).

Chapter 2 - Surfactant Partitioning in Nanoemulsions

2.1 Introduction

A wide variety of amphiphilic surfactants are commonly used to form and stabilize droplets in emulsions, which can have a wide range of droplet volume fractions ϕ and droplet radii a.[1-2] In a frequently encountered scenario, surfactant molecules that are soluble in the bulk continuous phase (BCP) of a first type of liquid yet are not soluble in the dispersed droplet phase (DDP) of a second type of liquid, which is immiscible with the first, preferentially adsorb onto droplet interfaces. These surfactant molecules typically function in two primary capacities: first, they facilitate rupturing of larger droplets into smaller ones during flow-driven emulsification by reducing the interfacial tension between the DDP and the BCP; second, they act as stabilizers by providing a repulsive energy barrier between droplet interfaces,[3] thereby inhibiting droplet coalescence during and after emulsification. To be effective, surfactant molecules must be soluble to a significant degree in at least one of the two phases, and for many common oil-in-water (O/W) emulsions, they are soluble in the BCP. For such O/W emulsions, salts of ionic surfactant molecules that have a charged headgroup and a short aliphatic tail group are often used because they are highly soluble in the aqueous BCP; such molecules typically have high hydrophile-to-lipophile balances (HLBs). A classic example of a high HLB surfactant is sodium dodecyl sulfate (SDS), which fully dissociates in water to yield Na^+ (sodium cations) and DS^- (dodecyl sulfate anions), even up to very large concentrations well in excess of 100 mM at room temperature. Even in the absence of oil droplets, many types of surfactant molecules self-assemble to form micellar

phases, which establish an equilibrium with a monomer population in the BCP, above a critical micelle concentration (CMC, C^*) that depends on the type of amphiphile.

While the BCP is often viewed as a reservoir containing the vast majority of the surfactant in most common microscale and macroscale emulsion systems, this picture may not be true for nanoemulsions (i.e., metastable nanoscale emulsions) that have very high surface area-to-volume ratios, corresponding to an average droplet radius of $\langle a \rangle < 100$ nm and reasonably large $\phi > 0.1$. Although nanoemulsions can have droplet sizes that lie in a range similar to those of lyotropic liquid-crystalline mesophases (*i.e.*, so-called microemulsion phases),[4] including swollen micellar phases[5] which are sometimes described as low-energy routes for nanodroplet formation,[4] nanoemulsions are typically made by the top-down rupturing of larger droplets into smaller droplets driven by flow, not through bottom-up self-assembly of multiple components as a result of significant mutual solubility. To avoid droplet coarsening through Ostwald ripening,[6] the type of molecules in the DDP are often chosen to be highly insoluble in the BCP. Providing that Ostwald ripening is avoided, coalescence stability rules for microscale emulsion systems are often related to the concentration of surfactant molecules in the BCP and to the applied osmotic pressure.[7-8] For such stable nanoemulsions, it would therefore be interesting to investigate the partitioning of surfactant to the droplet interfaces, and this investigation, leveraged by the high surface area-to-volume ratios that are typical of nanoemulsions, could potentially lead to a useful means of measuring adsorption isotherms.

During the process of high flow rate emulsification (HFRE) that is typically applied to transform premixed microscale emulsions into naneomulsions in a now-common route,[9] both the number of droplets and their total interfacial area increase dramatically. These substantial increases could potentially affect the relative thermodynamic partitioning of surfactant as monomers in the

bulk, in micellar self-assemblies in the bulk, and at droplet interfaces through adsorption after amphiphile equilibrium is re-established following HFRE.

Given the prevalence and broad utility of HFRE in creating nanoemulsions, it is important to determine where surfactant molecules reside after a microscale premixed oil-in-water emulsion has been transformed into a nanoemulsion by HFRE processing. The reduction in droplet sizes by HFRE has been previously studied and well characterized using dynamic light scattering and neutron scattering.[4, 10] Here, instead, we primarily focus on measuring surfactant partitioning and the average area per surfactant molecule on the nanodroplet interfaces at equilibrium. After HFRE, the final equilibrium bulk ionic amphiphile concentration, $C_{b,f}$, could be very different than the initial bulk ionic amphilile concentration, $C_{b,i}$, as a consequence of the dramatic reduction in droplet size at fixed total droplet volume caused by extreme droplet rupturing. By mass conservation of the surfactant, the final post-HFRE surface concentration at equilibrium is $C_{s,f} = [(C_{b,i} - C_{b,f})V_b]/A_{s,f}$, where V_b is the volume of the BCP in the emulsion in which all of the nonadsorbed surfactant is assumed to reside and $A_{s,f}$ is the final post-HFRE total surface area of all nanodroplets. Here, the units of C_s are the number (or moles) of adsorbed molecules per area, whereas C_b refers to moles per volume. By developing a robust method of measuring $C_{b,f}$ following equilibration after HFRE in a nanoemulsion having a known $C_{b,i}$, we deduce $C_{s,f}$ and therefore the equilibrium partitioning of the surfactant and the adsorption isotherm of the surfactant at the oil–water interface.

A variety of experimental methods have been used previously to measure amphiphile adsorption on oil–water interfaces. For instance, the surface concentrations of fatty acids and triblock copolymers adsorbed at the hexane–water interface have been measured using neutron reflection.[11] In principle, the partitioning of surfactant to the highly curved oil–water interfaces of

droplets in a nanoemulsion could yield different values of surface concentration if the radius of the nanodroplets begins to approach the effective size of the adsorbed surfactant. Although this method can be quite sensitive, surfactant adsorption occurred at the flat interface of two bulk phases in contact, not on the curved interfaces of droplets. Small-angle neutron scattering can also be used to probe changes in scattering length density profiles at droplet interfaces, which can be related to surfactant adsorption.[12] By contrast to these neutron scattering approaches, which require access to specialized neutron scattering facilities, a different technique of filtering microscale emulsion droplets from the continuous phase and then quantifying the anionic surfactant, such as SDS, remaining in that phase by complexing it with an excess of positively charged dye, such as methylene blue (MB^+), has been developed[13] using optical absorption spectroscopy.[14-17] Monovalent cationic MB^+ combines in a 1:1 molecular ratio with monovalent anionic DS^- to form charge-neutral complexes that can then be extracted into chloroform and analyzed spectroscopically. Yet another method for obtaining an adsorption isotherm is to make IFT measurements of an oil phase and aqueous surfactant solution, such as PDMS and SDS(*aq*), and then determine the surface coverage through the Gibbs derivative.[18-19] Even this approach has a significant potential drawback because the Gibbs derivative of the IFT at higher concentrations, where the activity is not equal to the concentration, can lead to substantial inaccuracies.

While neutron scattering and complexing–extraction spectroscopic methods may be necessary for measuring adsorbed surface concentrations when the quantities of surfactant are very limited, even simpler and more accessible methods, such as gravimetric analysis (e.g., using a common 0.1 mg analytical balance) or electrical conductivity, could be useful for studying surfactant partitioning in nanoemulsions provided that the quantities of surfactant and oil are not extremely restricted. For instance, analytical gravimetric methods, when combined with

amphiphile precipitation and separation methods, could be used to measure the equilibrium surfactant concentration in the BCP, allowing the surfactant concentration on the interfaces of droplets to be deduced. Moreover, if the surfactant used in an aqueous BCP is ionic, then electrical conductivity can potentially be used to measure its concentration, provided that sufficient control studies have been performed in advance using solutions having a wide range of known concentrations.

Here, we have developed new experimental methods to measure surfactant adsorption and the partitioning of an anionic amphiphilic surfactant, DS^-, to surfaces of nanodroplets in O/W nanoemulsions that have been made by HFRE and subsequently size-fractionated. Such fractionated nanoemulsions have a better characterized total interfacial area than unfractionated nanoemulsions, which typically have a considerably larger polydispersity. Thus, using fractionated nanoemulsions can improve the accuracy of the average adsorbed surface concentration of surfactant measured using gravimetric and electrical conductivity analyses. For such fractionated nanoemulsions, we measure the adsorption isotherm of DS^- onto water–silicone oil (polydimethylsiloxane, PDMS) interfaces of nanodroplets at room temperature, and we show that this measured isotherm can be described using a simple Langmuir model, yielding a maximum equilibrium adsorbed surface concentration $C_s°$ and an adsorption equilibrium constant K. We also adjust this isotherm on the basis of a Gibbs derivative that we obtain by measuring the IFT versus bulk concentration. Thus, a relatively simple macroscopic experimental method can be used to obtain useful information about the thermodynamic energetics of the equilibrium adsorption reaction of amphiphiles on oil–water interfaces. Beyond fractionated nanoemulsions, we also study bulk-surface partitioning of DS^- in unfractionated PDMS silicone oil-in-water nanoemulsions over a wide range of SDS concentrations directly following HFRE for fixed emulsification conditions

and ϕ. In these studies, we clearly detect the reduction in the bulk DS^- concentration as a consequence of the creation of a huge additional surface area of nanoscale droplets resulting from the HFRE process.

2.2 Theory

When an amphiphile in the aqueous BCP adsorbs on the interface of an oil droplet at equilibrium at a fixed temperature T, it loses some entropy associated with accessible translational and rotational microstates in the BCP, compared to the more limited accessible microstates available on the interfaces of droplets. In addition, when the aliphatic portion of the amphiphile leaves the aqueous environment and becomes solvated by the oil, there is an energy change that primarily arises from differences in van der Waals interactions, known as the adsorption enthalpy. For ionic amphiphiles, accounting for all contributions to the adsorption enthalpy, which can include electrostatic interactions and screening by mobile counterions, is complex, so we make simplifying assumptions that are typical of Langmuir's classic adsorption model.[20] We assume that screening by counterions is sufficiently strong that the concept of a surface adsorption site having an irreducible (*i.e.*, incompressible) area, $A°$, which can either be occupied or unoccupied, is valid. Moreover, we assume that the total surface area in the emulsion after HFRE is vastly larger than before HFRE, so the initial number of moles of adsorbed surfactant on droplet surfaces can be neglected.

The classic reversible adsorption reaction, when expressed in terms of amphiphiles (A) adsorbing onto vacant surfaces sites (S) to yield surface sites occupied by adsorbed molecules (AS) is $A + S \rightleftharpoons AS$. Suppose that the initial number of moles of amphiphiles in the BCP is $n_{b,i} = C_{b,i}V(1 - \phi)$ and that the initial number of moles of surface sites on droplets immediately after HFRE in the nanoemulsion is $n_{s,i} = A_s C_{s,i}$, where V is the volume of the system, $V_b = V(1 - \phi)$ is the volume

of the BCP, $A_s = 3\phi V/a$ is the total interfacial area of droplets, and $C_{s,i} = C_s^\circ$ is the initial surface concentration of unoccupied surface sites equivalent to one amphililic molecule per irreducible area A°: $C_s^\circ = 1$ molecule/A°, equivalent in a molar form to $C_s^\circ = (A^\circ N_0)^{-1}$, where N_0 is Avogadro's number. The number of droplets is $N_{drop} = V\phi/(4\pi a^3/3)$. Here, for simplicity, we have implicitly assumed that the emulsion is perfectly monodisperse and all droplets have the same radius a. Because the number of moles of surface sites, n_s, does not change during equilibration after HFRE, we can express $n_s = n_{s,i} = 3\phi V/(N_0 A^\circ a)$. At equilibrium, the law of mass action for the adsorption reaction implies that the dimensionless equilibrium constant K can be written as:

$$K = \frac{n/n_s}{[(n_{b,i} - n)/n_s][(n_s - n)/n_s]} \tag{2.1}$$

where n represents the equilibrium number of moles of adsorbed amphiphiles (or equivalently occupied surface sites, *i.e.*, AS) such that $n < n_{b,i}$ and $n < n_s$ for physical solutions. Here, we have used n_s as a reference number of moles for all factors in the law of mass action because n_s does not change during the process of equilibration. Following a common convention, we define the fraction of surface sites occupied by adsorbed amphiphiles at equilibrium to be $\theta = n/n_s$, so K reduces to:

$$K = \frac{\theta}{[(n_{b,i}/n_s) - \theta](1 - \theta)} \tag{2.2}$$

This leads to a quadratic equation for θ if K, $n_{b,i}$, and n_s are known:

$\theta^2 - [1 + K^{-1} + (n_{b,i}/n_s)]\theta + (n_{b,i}/n_s) = 0$. Solving this quadratic equation yields:

$$\theta = \frac{1}{2}(1 + K^{-1} + (n_{b,i}/n_s)) - \frac{1}{2}[(1 + K^{-1} + (n_{b,i}/n_s))^2 - 4(n_{b,i}/n_s)]^{1/2} \qquad (2.3)$$

where the physically meaningful root has been chosen. The above equation describes the dimensionless adsorption isotherm, expressed as the fractional coverage of the droplet surfaces as a function of the initial bulk-to-surface mole ratio $n_{b,i}/n_s$.

Alternatively, if an adsorption isotherm of the final equilibrium surface concentration $C_{s,f} = n/(3\phi V/a) = \theta/(N_0 A°)$ as a function of the final concentration of amphiphiles remaining in the BCP, $C_{b,f} = C_{b,i} - \{n/[V(1-\phi)]\}$, has been measured by varying $n_{b,i}$ over a wide range at fixed ϕ, then it is possible to deduce K and $A°$. For oil droplets in aqueous surfactant solutions, the values of K and $A°$ are key properties describing the adsorption behavior of a particular type of amphiphile on oil–water interfaces for a particular kind of oil. Reorganizing the law of mass action leads to a Langmuir isotherm, appropriate for emulsions and nanoemulsions, of the final surface concentration as a function of the final bulk concentration after HFRE at equilibrium:

$$C_{s,f} = \frac{(A°N_0)^{-1}}{1 + [K(1-\phi)aA°N_0C_{b,f}/(3\phi)]^{-1}}, \qquad (2.4)$$

where we can define a first fit parameter to be a saturated surface concentration $C_s° = (A°N_0)^{-1}$ at very high $C_{b,f}$ and a second fit parameter to be a modified equilibrium constant $K' = K(1-\phi)a/(3\phi)$, which is the slope of the isotherm at dilute $C_{b,f}$. The simplified Langmuir isotherm in terms of the two fit parameters is:

$$C_{s,f} = \frac{C_s°}{1 + [C_s°/(K'C_{b,f})]}. \qquad (2.5)$$

The fundamental amphiphile adsorption parameters $A°$ and K can thus be obtained from the fit parameters: $A° = (C_s°N_0)^{-1}$ (where fit parameter $C_s°$ is obtained in molar units)

and $K = K'(3\phi)/[(1-\phi)a]$.

A related quadratic formula can also be constructed to fit experimental measurements of $C_{b,f}$ as a function of $C_{b,i}$ directly, yielding both fundamental adsorption parameters K and $A°$. Thus, measuring post-HFRE $C_{b,f}$ as a function of $C_{b,i}$ can also be used to determine $C_s°$ and K through a least-squares fit to a solution of a quadratic equation without even requiring the construction of an isotherm. This is a useful direct route for nanoemulsions following the creation of a large additional surface area through flow-induced droplet rupture and size reduction. Using $C_{b,f} = C_{b,i} - \{n/[V(1-\phi)]\}$ and substituting $n = n_s(C_{s,f}/C_s°)$, which is proportional to the normalized isotherm of eq 2.5, we obtain a quadratic equation in $C_{b,f}$:

$$C_{b,f}{}^2 - \left[C_{b,i} - \frac{C_s°(K^{-1}+1)}{a'}\right]C_{b,f} - \frac{C_{b,i}C_s°}{Ka'} = 0 \qquad (2.6)$$

The physically relevant solution of this equation is:

$$C_{b,f} = \frac{1}{2}\left[C_{b,i} - \frac{(K^{-1}+1)C_s°}{a'}\right] + \frac{1}{2}\left\{\left[C_{b,i} - \frac{(K^{-1}+1)C_s°}{a'}\right]^2 + \frac{4C_{b,i}K^{-1}C_s°}{a'}\right\}^{1/2}, \qquad (2.7)$$

where $a' = a(1-\phi)/(3\phi)$ has been defined as a rescaled droplet radius.

In the above modeling, we have used a Langmuir isotherm equation to represent the adsorbed surfactant surface concentration versus the total bulk concentration. For surfactants such as SDS that have a CMC, we assume that this bulk concentration includes both monomers and micelles. For micelle-forming surfactants, when the bulk concentration exceeds the CMC, then the effective osmotic pressure of monomers does not increase in the same manner as below the CMC

since monomers have the additional option of forming micelles. Consequently, the plateau in the surface concentration of the Langmuir isotherm equation can reflect micelle creation in lieu of additional surface adsorption. Thus, the parameters that one might extract from nanoemulsion adsorption experiments should not necessarily be interpreted as corresponding to a Langmuir model in which micelle creation is entirely absent. While we find that the Langmuir isotherm equation can model our experimental findings empirically, we recognize that a more complete theoretical treatment would consider the three-phase equilibrium between surfactant molecules in the bulk continuous phase, surfactant molecules adsorbed onto droplet interfaces, and surfactant molecules in micelles.

2.3 Materials and Methods

Our investigations involve two primary sets of experiments: (1) measuring surfactant partitioning in fractionated uniform nanoemulsions, which have a total droplet surface area that can be more accurately determined as a consequence of reduced droplet polydispersity, and (2) measuring surfactant partitioning in unfractionated polydisperse nanoemulsions immediately after HFRE in order to detect the effective consumption of surfactant from the BCP via adsorption onto the newly created droplet interfaces. We first describe materials and methods that are common to both sets of experiments, and then we describe materials and methods specific to each set of experiments.

2.3.1 Common Procedures

Nanoemulsification

A premix emulsion is prepared using a standard emulsification technique:[21] poly(dimethylsiloxane) (PDMS, Gelest, viscosity 10 cSt, mass density 0.935 g/mL) is slowly

added to an SDS solution, which has been set to 50 mM, while agitating using a rotary hand mixer (PowerGen, model 125S1) until $\phi = 0.15$ is reached. The surfactant used for this emulsion is SDS (MP Biomedicals, Ultrapure, MW = 288.38 g/mol). Inspection using an optical microscope reveals that the resulting emulsion droplets are microscale and highly polydisperse (i.e., droplet radii range from ∼1 to ∼10 μm). This premix emulsion is then stirred to ensure that ϕ is uniform, loaded into the input vessel of a microfluidic homogenizer and subjected to HFRE (a Microfluidics M-110P homogenizer with a 75 μm Y-type diamond chamber, liquid pressure of 30 000 psi ≈ 2×10^3 atm, equipped with a cooling coil in an ice–water bath) for a total of eight passes to reduce the droplet size and improve the droplet uniformity.[4]

Characterizing Nanodroplet Radii

We dilute NEMs made at higher ϕ using a 10 mM SDS solution to a final highly dilute $\phi \approx 10^{-5}$, corresponding to the single-scattering limit. From dynamic light scattering (DLS) measurements (Photocor, wavelength $\lambda = 633$ nm, scattering angle 90°, temperature $T = 23$ °C), we obtain intensity-weighted average hydrodynamic radii $\langle a \rangle$.

Deducing the Equilibrium Adsorbed Surface Concentration of Surfactant

Using the measured $C_{b,f}$, we calculate the equilibrium final surface concentration of adsorbed amphiphiles as follows. For a volume V of nanoemulsion having a droplet volume fraction ϕ, the total number of moles of ionic amphiphile added to create the nanoemulsion is $n_{b,i} = C_{b,i}V(1 - \phi)$. The final number of moles of ionic amphiphile in the BCP after HFRE and equilibration is $n_{b,f} = C_{b,i}V(1 - \phi)$. By mass conservation, the number of moles of adsorbed surfactant on the surfaces of nanodroplets is $n_{s,f} = n_{b,i} - n_{b,f}$, so the surface concentration of adsorbed amphiphilic ions on the surfaces of monodisperse spherical nanodroplets is

$C_{s,f} \approx n_{s,f}/[N_{drop}(4\pi\langle a\rangle^2)] \approx [(1-\phi)/(3\phi)](C_{b,i} - C_{b,f})\langle a\rangle$. Here, we indicate an approximation because we have not included the effects of polydispersity of the droplet size distribution; these expressions become more exact as the emulsion's size distribution approaches the monodisperse limit.

2.3.2 Procedures for Fractionated Nanoemulsions

Nanodroplet Size Fractionation

After HFRE at $\phi = 0.15$, the resulting NEM is ultracentrifuged (Beckman L8-55: swinging bucket SW-28 rotor, polycarbonate tubes) until the droplets cream, creating elastic plugs at the tops of the centrifuge tubes.[4] These plugs are removed from the centrifuge tube and similarly cut into pieces or fractions; each fraction has a different radial size distribution. The same fractions from multiple plugs are combined and resuspended in 10 mM SDS. This fractionation procedure is repeated three times, yielding a final NEM having an average hydrodynamic radius of $\langle a\rangle = 40.1 \pm 0.8$ nm, measured using dynamic light scattering. This nanoemulsion's polydispersity is $\delta a/\langle a\rangle \approx 15\%$, close to a value obtained in earlier neutron scattering experiments on similarly fractionated nanoemulsions.[22]

Measuring the Total Amphiphile Mass through Precipitation

To determine the total quantity of surfactant in an NEM, we have developed a gravimetric analytical method that relies on a precipitation reaction, thereby inducing complete droplet coalescence. Sulfates are known to be highly insoluble in electrolyte solutions containing several different types of divalent cations[23] (e.g., Ba^{2+}, Sr^{2+}), so we anticipate that it is possible to create insoluble precipitates by mixing an O/W NEM stabilized by DS^- (MW = 265.39 g/mol) with an aqueous solution of $SrCl_2$, yielding solid strontium dodecyl sulfate, $Sr(DS)_2$ (MW = 618.34 g/mol). To 1 g of a NEM, we add 3 g of a highly concentrated $SrCl_2$ solution (20 wt %), so the

concentration of Sr^{2+} is far in excess of the concentration of DS^-. This process also neutralizes the DS^- and thereby causes the global coalescence of all droplets, leading to complete oil breakout. The resulting $Sr(DS)_2(s)$ is then separated from the residual oil and water as follows. After precipitation, the entire coalesced nanoemulsion is loaded onto a piece of Whatman #5 filter paper, resting on a Büchner funnel. We apply vacuum filtration, rinsing with water followed by rinsing with low-molecular-weight PDMS (0.65 cSt PDMS, Gelest), which serves as a volatile solvent for the nonvolatile 10 cSt PDMS oil. The filter paper holding $Sr(DS)_2(s)$ is placed in an oven at 45 °C for at least 12 h to ensure complete evaporation of water and 0.65 cSt PDMS. Control studies confirm that no residual masses of water, PDMS, solid NaCl, or solid $SrCl_2$ remain on the filter paper. Assuming total recovery, the total mass of SDS, m_{SDS}, in the nanoemulsion can be calculated from the measured mass of $Sr(DS)_2(s)$.

Measuring Droplet Volume Fraction

An aliquot of a NEM (e.g., $\phi \approx 0.15$ to 0.3) is placed in a plastic weighing boat; its mass is measured to be m_{NEM}. This loaded weight boat is heated overnight in an oven set to 45 °C, thereby evaporating water from the NEM completely. By simple mass conservation and because the 10 cSt PDMS oil and SDS are nonvolatile, the mass of water present in the initial NEM sample, m_{H2O}, is given by the difference in masses before and after evaporation. If m_{SDS} is known through the precipitation method on a per mass of NEM basis for the same initial mass of NEM, then the mass of PDMS, m_{PDMS}, can be calculated as $m_{PDMS} = m_{NEM} - m_{SDS} - m_{H2O}$.

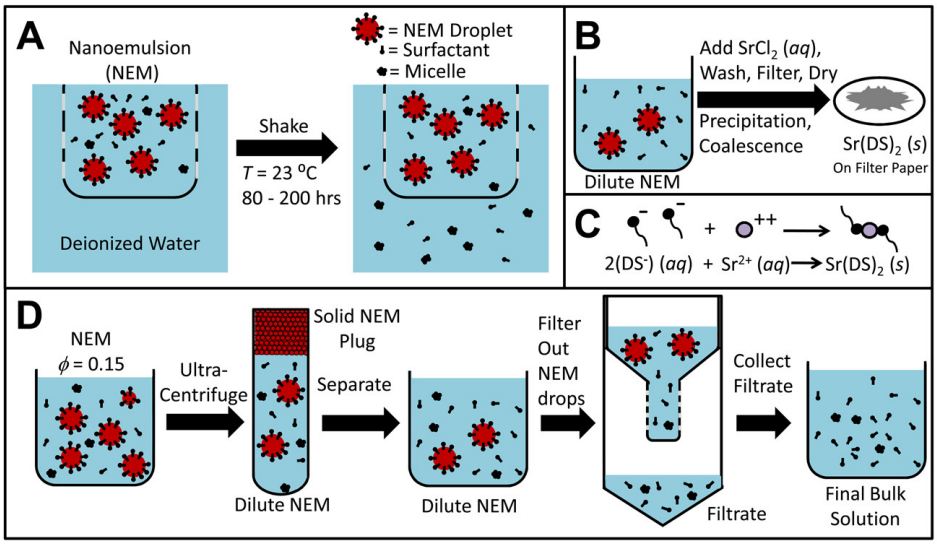

Figure 2.1. Schematics of analytical procedures used to measure the final bulk surfactant concentration, $C_{b,f}$, of an ionic amphiphile in oil-in-water (O/W) nanoemulsions (NEMs). (A) Fractionated monodisperse NEMs are placed in contact with deionized water via a semipermeable membrane (SPM) in a filter. Sodium dodecyl sulfate (SDS) surfactant in the NEM can pass through the SPM, but droplets cannot. SDS concentrations reach equilibrium, as monitored when the conductivity of the aqueous solution of SDS outside the filter stops changing. The steady-state conductivity of this yields a bulk concentration of SDS after desorption and dilution. **(B)** Dodecyl sulfate anions (DS^-) in the NEM after equilibration are reacted with an excess of strontium ions (Sr^{2+}) to form an insoluble solid, thereby causing the coalescence of all droplets; this solid is separated from the oil and water by vacuum filtration and two washing steps. **(C)** Precipitation reaction: Sr^{2+} reacts with 2 DS^- to form insoluble solid $Sr(DS)_2$. **(D)** Unfractionated NEMs only: $C_{b,f}$ is measured using a two-step process. First, nearly all NEM droplets are rapidly creamed into a solid plug that is removed. Second, remaining residual NEM droplets are centrifugally filtered out.

Measuring the Bulk SDS Concentration

In order to have access to bulk SDS concentrations without droplet contamination, we place an NEM with a known ϕ, $\langle a \rangle$, and m_{SDS} in contact with one side of a porous membrane of a centricon filter (EMD Millipore Amicon Ultra, 100 kDa molecular weight cutoff, MWCO), which is also in contact with a fixed volume (ranging between 17–40 mL) of deionized water on the other side. The selected pore size of the membrane allows water molecules, Na^+, DS^-, and micelles of DS^- to pass through, but not nanodroplets, as shown in Figure 2.1A.[24] Ultrapure water (Millipore Milli-Q Academic, resistivity ~15 MΩ·cm) is weighed in a container holding the ultrapure water

while an aliquot (ranging from ~0.5 to 1.5 g) of the NEM at $\phi \approx 0.15$ is weighed in a centricon filter. The filter is placed inside the container so that the levels of the NEM in the filter and water in the container are equal, and no external gravitational pressure is driving mass transport across the membrane. The container and inserted filter are placed on a shaker and agitated for >20 h at ~2 oscillations/s.

We measure bulk SDS concentrations using a slightly modified hand-held electrical conductivity meter (Digital Aid TDS-EC Meter, maximum limit of 9 mS/cm). To prevent trapped air bubbles from adversely influencing these conductivity measurements, we have removed three plastic fins on this meter near its electrodes. We have performed calibration trials to correlate the electrical conductivity with the concentration of SDS that is in a droplet-free aqueous solution before and after removal of the fins, thereby ensuring accurate conductivity measurements. The conductivity of multiple SDS solutions has been measured and plotted with respect to their concentrations (e.g., Figure 2.2B). Below the CMC of SDS, $C^* \approx 8$ mM, the conductivity is linear with concentration; however, just above the CMC, it is also approximately linear yet has a different slope and intercept. These calibrations extend to SDS concentrations well above the CMC.

To measure the increase in the surfactant concentration in the aqueous solution outside the filter over time, we monitor its electrical conductivity, σ_e, throughout the process of equilibration, which involves the transport of DS^- and Na^+ in equimolar proportions through the centricon filter from the NEM. The measured σ_e increases rapidly initially and then gradually trends toward a plateau. We plot σ_e versus t and fit this function using the empirical formula $\sigma_e(t) = \sigma_e^\circ(t/\tau)/[1 + (t/\tau)]$, where σ_e° is a long-time plateau conductivity and τ is a time constant. Correlation coefficients R^2 for all trials were $R^2 > 0.99$, and τ values ranged from 1 to 50 h. NEMs at higher

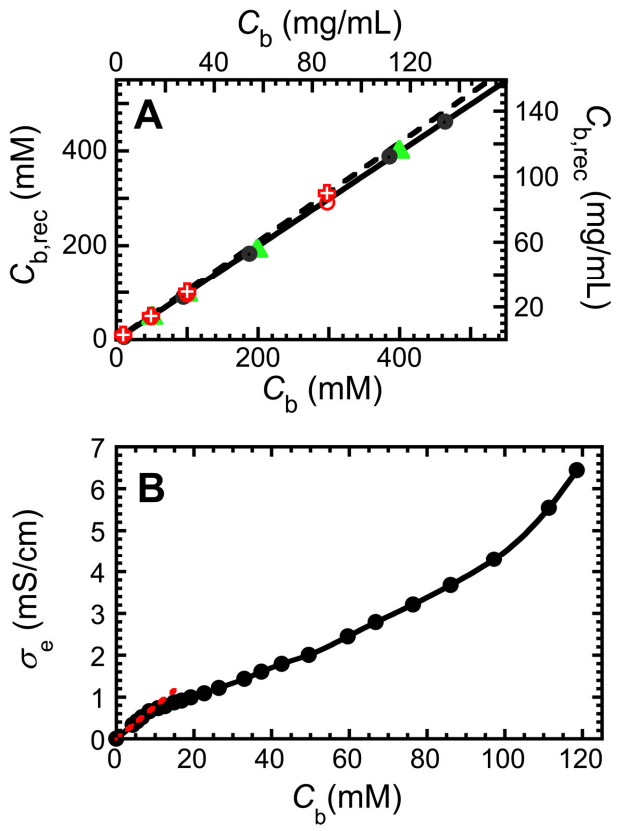

Figure 2.2. Calibration results for the massing of precipitated Sr(DS)$_2$ and the conductivity of dissociated SDS in aqueous solution. **(A)** Bulk surfactant concentration recovered, $C_{b,rec}$, using strontium precipitation, washing, and evaporation (solid symbols), is plotted as a function of the known prepared bulk concentration, C_b. For reference, concentrations are also shown in mg/mL on the right and top axes. Measured $C_{b,rec}$ as a function of prepared C_b in mg/mL (red open crosses: read using right and top axes only) from Sr^{2+} precipitation-evaporation. Dashed line: linear fit to open red crosses. Open symbols: calculated recovered bulk concentration of amphiphilic ions as a function of the prepared bulk concentration in mM (DS^-, open circles read using left and bottom axes only). Green solid triangles represent the recovered Sr(DS)$_2$ (converted to [SDS] using dimensional analysis) from NEM samples. The data all are very close to the solid line representing ideal 1:1 recovery. **(B)** Measured electrical conductivity σ_e as a function of bulk SDS concentration C_b (black solid circles). Black line: cubic spline fit over the entire measured range of C_b. Red dashed line: linear fit to $\sigma_e(C_b)$ for $C_b < 8$ mM (line is extrapolated up to 15 mM to highlight the nonlinear behavior of the measured $\sigma_e(C_b)$ above the CMC).

initial DS^- concentrations equilibrate more rapidly over smaller τ, whereas those at lower initial DS^- concentrations equilibrate more slowly over larger τ. Using the results of the calibration trials, we convert values of $\sigma_e°$ from the fit into final bulk surfactant concentrations, $C_{b,f}$. From this, we also quantify the total mass of SDS lost by the NEM.

2.3.3 Procedures for Unfractionated Nanoemulsions

Nanodroplet Separation by Ultracentrifugation and Filtration

We can separate the BCP from the nanodroplets by creating a process involving ultracentrifugation and filtration, shown schematically in Figure 2.1D. We ultracentrifuge a NEM at ϕ = 0.15 after HFRE (Beckman L8-55: swinging bucket SW-28 rotor, polycarbonate tubes), thereby concentrating the vast majority of droplets at the top of the centrifuge tubes into an elastic plug without causing droplet coalescence. For NEMs having larger $\langle a \rangle$ > 60 nm, corresponding to lower $C_{b,i}$, an ultracentrifugation speed of ~8000 rpm over 6 h is used, whereas for NEMs having smaller average radii, corresponding to higher $C_{b,i}$, a higher ultracentrifugation speed of ~18 000 rpm over ~24 h is used. These ultracentrifugation conditions have been chosen to prevent droplet coalescence and to keep the duration of ultracentrifugation to a minimum.

After ultracentrifugation, the elastic plug of a concentrated nanoemulsion that has formed at the top of the centrifuge tube is physically removed using a small spatula. After the plug is extracted, the remaining aqueous solution, which can still contain a small residue of very fine nanodroplets that did not adhere to the plug, is then filtered to remove all remaining nanodroplets (EMD Millipore Amicon Ultra, 100 kDa MWCO). The separated nanodroplets appear as a very thin translucent layer above the filter. The filtrate does not contain any nanodroplets, so it is essentially an SDS solution that we assume has the same SDS concentration as in the starting BCP of the post-HFRE nanoemulsion.

Measuring the Bulk SDS Concentration

We measure $C_{b,f}$ by gravimetric analysis of the filtrate resulting from ultracentrifugation and filtration. This is done in two different ways: simple evaporation (SE) or precipitation evaporation (PE). For SE, after ultracentrifugal separation and filtering, the water in a filtrate solution volume of about 10 mL is evaporated in a vacuum oven. We then measure the mass of the solid SDS (Denver Instruments, APX-200, 0.1 mg precision), yielding $C_{b,f}$.

Alternatively, for PE, we add a precipitation agent in excess (e.g., Sr^{2+} cation in a solution of $SrCl_2$), causing solid $Sr(DS)_2$ to form (Figure 2.1B,C). We then filter out the precipitates (Whatman, 55 mm filter paper #1, effective pore size of 11 μm), rinse the precipitates with deionized water, evaporate the residual water, and measure the mass of the resulting white precipitate of dry $Sr(DS)_2$. Through calibration trials using SDS solutions having known concentrations, we have ensured that the chosen filter paper effectively captures all precipitates for the conditions we have used, as shown in Figure 2.2A. The PE method is faster than the SE method, so we primarily use PE to measure concentrations of DS^-. The precipitation of DS^- using Sr^{2+} leads to a larger recovered mass per mole of DS^- as compared to that obtained through evaporation, shown in Figure 2.2A, because the molar mass of two SDS molecules is less than that of one $Sr(DS)_2$ molecule. We have performed control experiments on a set of unfractionated post-HFRE NEMs, each of which has a known mass percentage of SDS which has been fixed by the NEM's original composition prior to HFRE. The surfactant content in each of these NEM control samples is determined using the PE method, described above, and the SDS concentration is calculated on the basis of the mass of dry precipitate remaining on the filter (Figure 2.2A, solid green triangles). By plotting the mass determined using the PE method as a function of the known mass in the original composition (Figure 2.2A), we find good agreement. Least squares fitting of

these control data yield a slope of 1.02 ± 0.01 and a correlation coefficient of $R^2 = 0.999$, indicating that the PE method reliably reports the SDS content with only a few percent uncertainty.

2.3.4 Interfacial Tension Measurements

We measure the interfacial tension of 10 cSt PDMS oil and aqueous SDS solutions from 0 to 100 mM using a calibrated surface tensiometer. We use a platinum du Noüy ring[25] (CSC Scientific Company, no. 70537, mean circumference 6.00 cm, radius ratio 55.6). The SDS solution is poured into a crystallizing dish (Pyrex, no. 3140, 80 mm diameter × 40 mm height), filling to ~1.5 cm. After flame-cleaning, the ring is lowered into the SDS solution such that the top of the ring is ~1 cm below the air/solution interface. The less-dense oil phase is slowly poured on top of the SDS solution, reaching a sufficient thickness (~1.5 cm) which precludes the interaction of the ring with the air/oil interface. The container is slowly lowered, and the force is monitored using a through-hole balance. The point of maximum force is used to calculate the IFT.

2.4 Results

2.4.1 Gibbs Isotherm

We measure the IFT, σ, as a function of C_b for a PDMS–SDS(aq) interface as shown in Figure 2.3. For small C_b below the CMC, $\sigma(C_b)$ decreases as DS^- adsorbs onto the O/W interface. As C_b approaches the CMC, the slope in $\sigma(C_b)$ begins to change, becoming less negative. For C_b above the CMC, $\sigma(C_b)$ stays near 10 mN/m and decreases only slightly. We use the Gibbs derivative to obtain an adsorbed DS^- surface concentration C_s from the slope of $\sigma(C_b)$

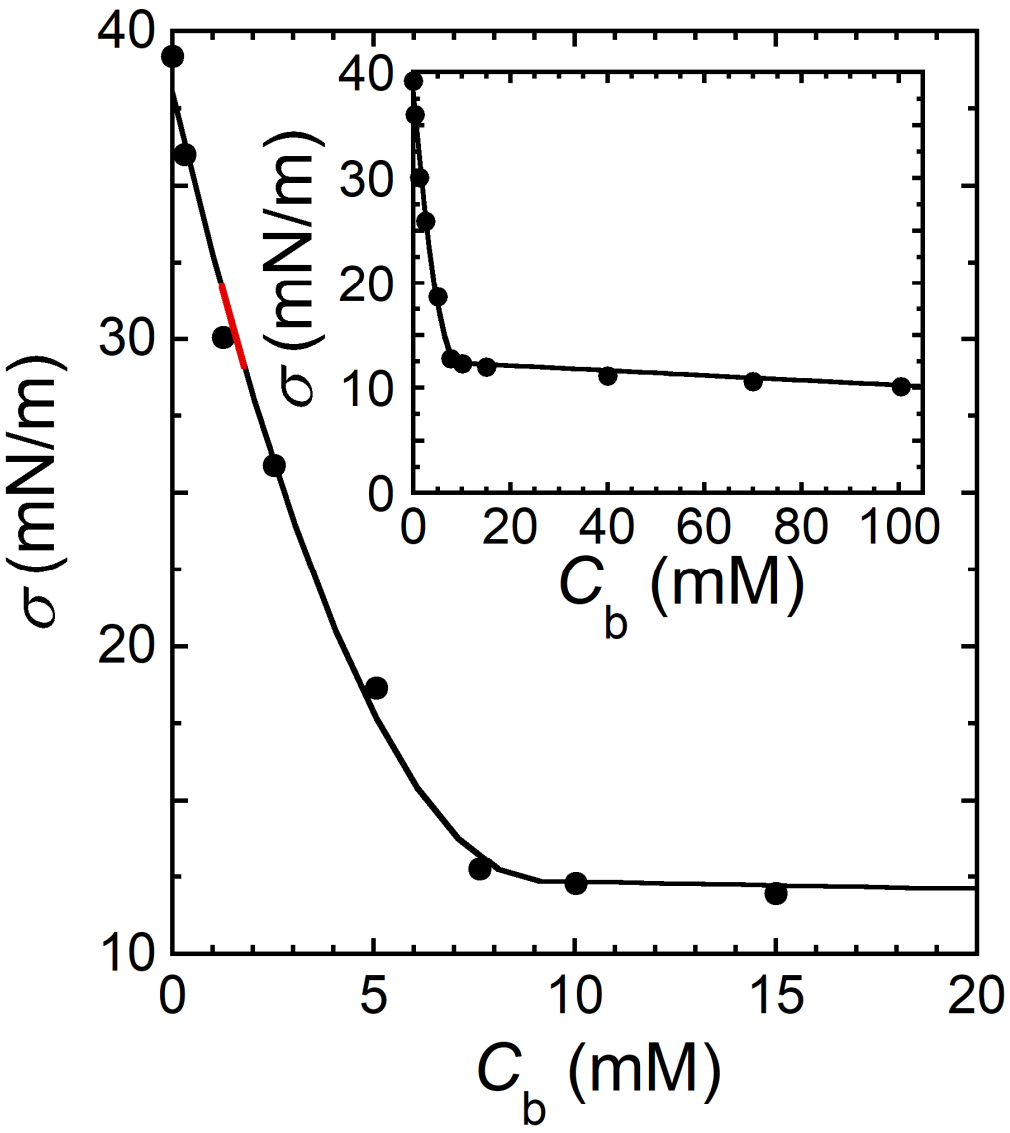

Figure 2.3. Interfacial tension (IFT) measurements of PDMS oil (10 cSt) and aqueous SDS solutions. The line shows the empirical fit using two second-order polynomials which converge to the same σ at the CMC. The red line shows where the Gibbs derivative was calculated to determine an accurate value of C_s, which is used to set the scale of surface concentration in the measured isotherm. **(Inset)** Measured IFT for bulk concentrations extending well above the CMC.

the Gibbs derivative to obtain an adsorbed DS^- surface concentration C_s from the slope of $\sigma(C_b)$ for C_b well below the CMC where the bulk activity of DS^- is reasonably represented by its bulk concentration:[19] $C_s = -C_b[d\sigma/dC_b]/(2RT)$, where C_b = 1.25 mM and $d\sigma/dC_b$ = 5.7 (mN/m)/mM, yielding C_s = 0.87 molecules/nm^2.

2.4.2 Adsorption Isotherm: Fractionated NEMs

For a fractionated NEM ($\langle a \rangle$ = 40.1 nm), we measure $C_{s,f}$ of DS^- adsorbed onto PDMS O/W interfaces of nanodroplets as a function of $C_{b,f}$, as shown in Figure 2.4. We employ gravimetric and conductivity methods to calculate the adsorbed DS^- by measuring the total mass of SDS and the concentration of $C_{b,f}$. (See section 3.3.2.) We observe that $C_{s,f}$ increases as $C_{b,f}$ increases and then transitions to a plateau at higher $C_{b,f}$. We scale the surface concentrations of this raw isotherm to match a reference value obtained from the Gibbs derivative of the IFT measurement. Using eq 2.5, we empirically fit the raw and adjusted (i.e., scaled) isotherm, based on a Langmuir equation, as shown in Figure 2.4. The resulting fit parameters for the adjusted isotherm are $C_s° = 2.3 \pm 0.5$ molecule/nm^2 (i.e., $\sim 43 \pm 9$ Å^2 per DS^- molecule) and $K' = (1.8 \pm 0.2) \times 10^{-6}$ m. To obtain K' in MKS units, $C_{s,f}$ is converted to mol/m^2, and $C_{b,f}$ is converted to mol/m^3 before performing the fit. The correlation coefficient of the fit for both isotherms is $R^2 = 0.96$, which is close to unity, indicating reasonably good agreement between the shape of the fitting function and the data. At the CMC of SDS (i.e., $C^* = 8.1$ mM), an evaluation of the fit for the adjusted isotherm yields $C_{s,f} = 1.8 \pm 0.1$ molecule/nm^2 (~ 55 Å^2 per DS^- molecule). Using $K = K'(3\phi)/[(1 - \phi)a]$, the value of K' from the fit corresponds to dimensionless $K = 25 \pm 3$.

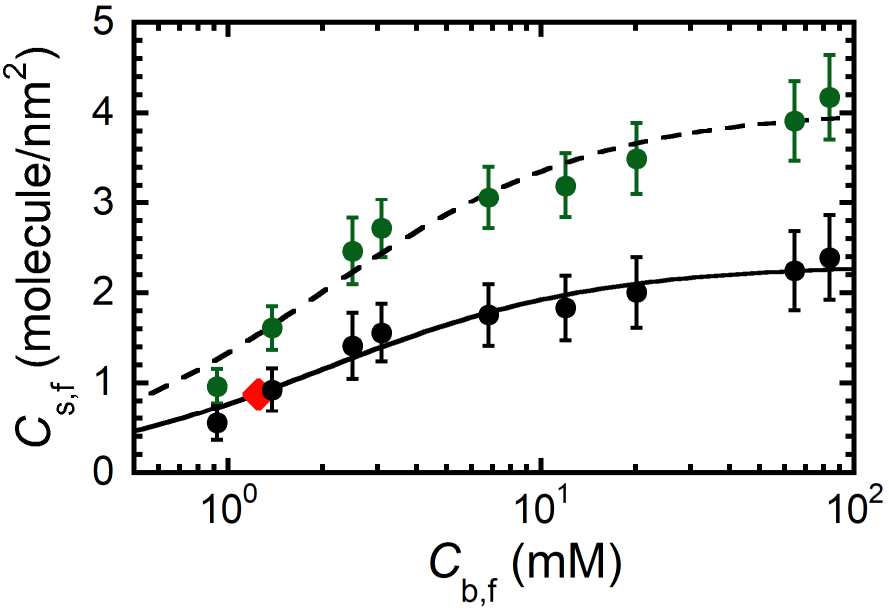

Figure 2.4. Raw and adjusted equilibrium adsorption isotherm of dodecyl sulfate anions onto water–silicone oil (poly(dimethylsiloxane)) interfaces obtained from the final surface concentration $C_{s,f}$ and final bulk concentration $C_{b,f}$ measured using a fractionated nanoemulsion. Raw measured surface concentrations (solid green circles) are scaled downward by a factor of 1.7 to match the surface concentration obtained by the Gibbs derivative of IFT measurements at low $C_{b,f}$ (solid red diamond, see Figure 2.3), yielding the adjusted surface concentration (solid black circles). Dashed line: fit of the raw isotherm to a Langmuir isotherm equation (eq 2.5), yielding $C_s° = 4.0$ molecules/nm^2 and $K = 44$. Solid line: fit of the adjusted isotherm to eq 2.5 using $K = K'(3\phi)/[(1 - \phi)a]$, yielding $C_s° = 2.3$ molecule/nm^2 and $K = 25$. (See section 2.4.1.) Given the experimental uncertainties in the measured surface concentrations (error bars on the black circles), the uncertainty in $C_s°$ of the adjusted isotherm is ±0.5 molecules/nm^2.

2.4.3 Adsorption Isotherm: Unfractionated NEMs

For unfractionated, polydisperse, post-HFRE NEMs, the measured $\langle a \rangle$ and measured $C_{b,f}$ are shown as functions of $C_{b,i}$ in Figure 2.5A,B, respectively. At fixed ϕ and for the same HFRE conditions, increasing $C_{b,i}$ results in smaller nanodroplets, consistent with prior observations, and we fit $\langle a \rangle$ versus $C_{b,i}$ to a semiempirical power-law function[4, 21]:

$$<a> = <a_{b,i}*>(C_{b,i}/C*)^{-\alpha} \quad (2.8)$$

yielding $R^2 = 0.98$ and parameter values of $\langle a_{b,i}^* \rangle = 72 \pm 3$ nm and $\alpha = 0.27 \pm 0.01$. This function captures the measured behavior well, and the values of $\langle a_{b,i}^* \rangle$ and α are close to those found previously for nearly the same SDS-stabilized PDMS silicone O/W composition but somewhat different emulsification conditions. [4, 21]

As a result of the significant adsorption of DS^- onto the area of nanodroplet interfaces after HFRE, $C_{b,f}$ is lower than $C_{b,i}$, and this effect is particularly pronounced for lower $C_{b,i}$. We substitute eq 2.8 for $\langle a \rangle$ in place of a in $a' = a(1 - \phi)/(3\phi)$ and fit the measured $C_{b,f}$ in Figure 2.5B using eq 2.7. This equation fits the measurements well over the entire range with $R^2 = 0.99$, yielding $C_s^\circ = 7 \pm 2$ molecule/nm^2 ($\sim$14 Å^2/molecule) and $K = 38 \pm 8$. Here, we emphasize that the total surface area of the polydisperse post-HFRE NEM is not well characterized by only a single parameter $\langle a \rangle$. This highlights the significant inaccuracies that can be encountered when attempting to obtain quantitatively valid isotherms using polydisperse emulsions that have only crudely estimated total surface areas based on average radii without regard to other aspects of the full droplet size distribution.

To quantify the partitioning of the surfactant in the resulting nanoemulsions, we next calculate the measured fraction of DS^- in the nanoemulsion system that has adsorbed onto droplet interfaces (i.e., post-HFRE), which we define to be $f_{ads} = 1 - (C_{b,f}/C_{b,i})$, as shown in Figure 2.5C. We note that f_{ads} is not the fraction of occupied surface sites but rather is equivalent to the mole fraction of surfactant in the system that has partitioned from the initial bulk continuous phase (i.e., pre-HFRE) to the surfaces of droplets in the post-HFRE NEM. At the

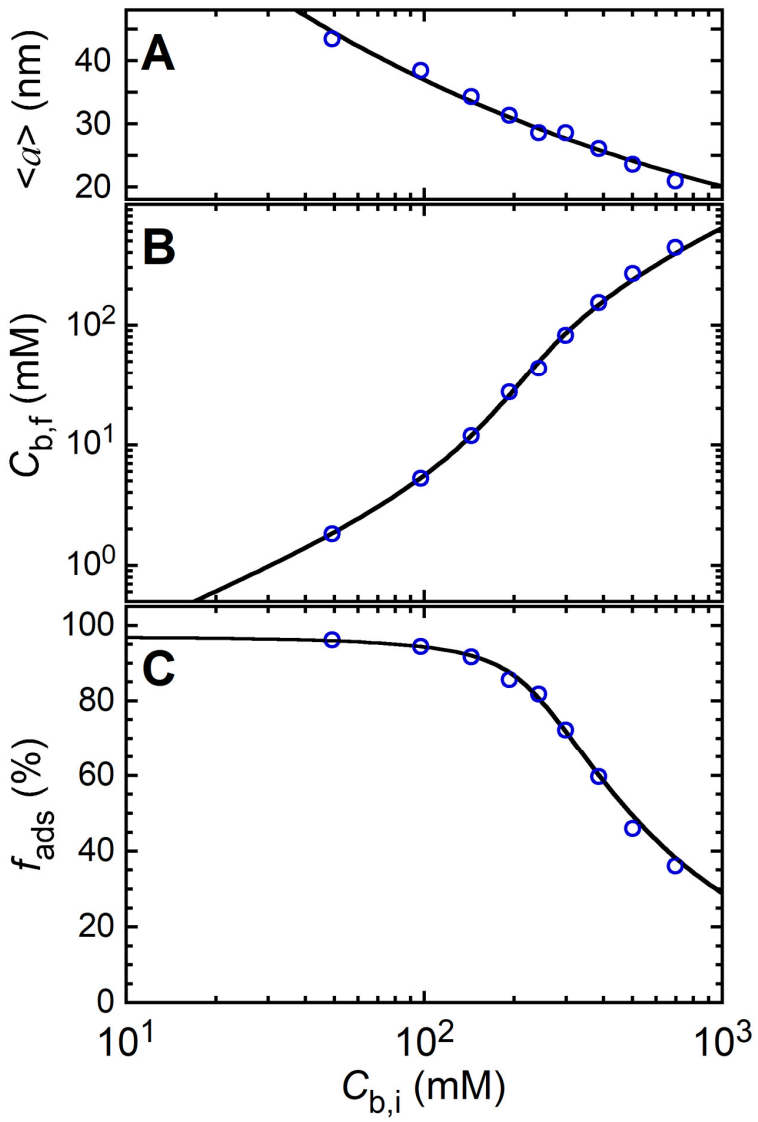

Figure 2.5. Partitioning of DS^- to droplet interfaces in unfractionated PDMS oil/water nanoemulsions after HFRE and equilibration. (A) Average hydrodynamic radius of nanoemulsion droplets, $\langle a \rangle$, determined by dynamic light scattering, as a function of $C_{b,i}$. (Line) Fit using eq 2.8. **(B)** Final bulk DS^- concentration, $C_{b,f}$, after HFRE and filtration (using the procedure in Figure 2.1D), plotted against the bulk initial DS^- concentration, $C_{b,i}$, before HFRE. (Line) Fit using eq 2.7. **(C)** Adsorbed fraction f_{ads} of DS^- onto nanodroplet interfaces after HFRE. (Line) Calculated $f_{ads} = 1 - (C_{b,f}/C_{b,i})$ using eq 2.7 and values of K and $C_s°$ from the fit in part B.

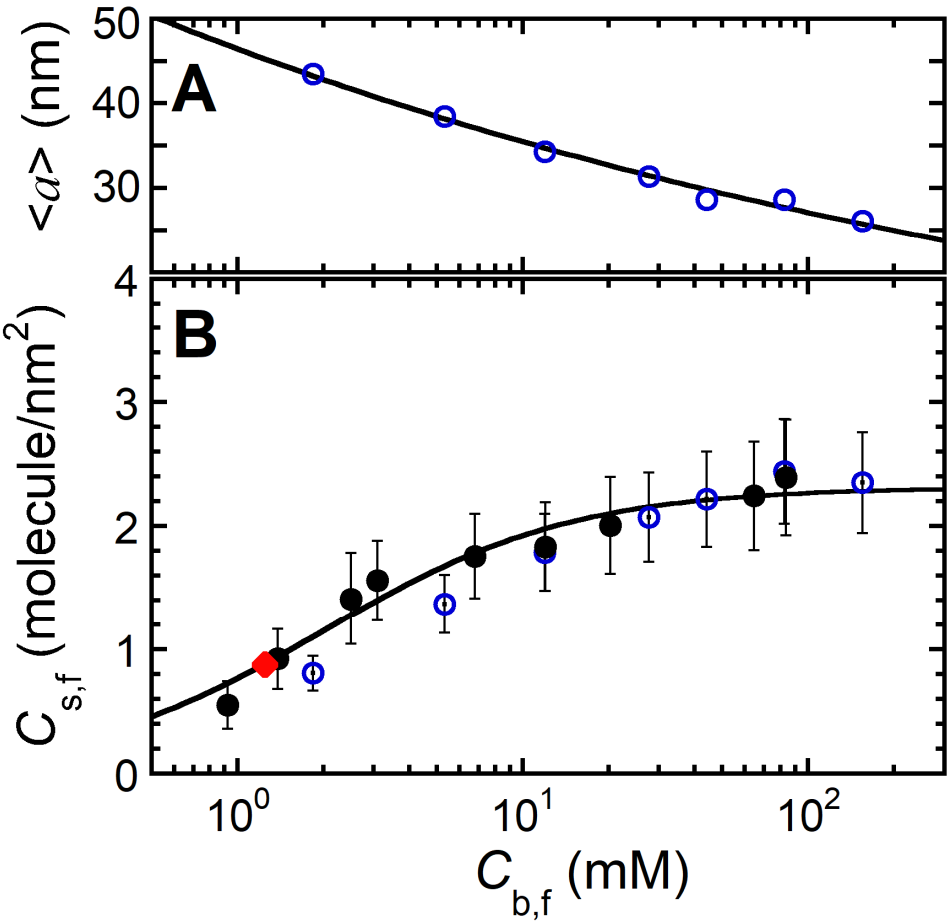

Figure 2.6. Comparison of equilibrium adsorption isotherms for dodecyl sulfate anions onto PDMS silicone oil–water interfaces for both fractionated and nonfractionated NEM systems. **(A)** Average hydrodynamic radius of nanodroplets, $\langle a \rangle$, from the nonfractionated NEM droplets, determined by dynamic light scattering, as a function of $C_{b,f}$. (Line) Fit using eq 2.9. **(B)** Combined measured isotherm of the final equilibrium DS^- surface concentration, $C_{s,f}$, as a function of the final bulk DS^- concentration, $C_{b,f}$. (Line) Fit of fractionated NEM data (black closed circles, see Figure 2.4), which has been adjusted using the Gibbs derivative of IFT measurements (red diamond, see Figure 2.3), to a Langmuir equation. $C_{s,f}$ data for the unfractionated NEM (blue open circles) have been scaled down uniformly by a factor of ~3 to match the adjusted $C_{s,f}$ data for the fractionated NEM.

lowest measured $C_{b,i} \approx 48$ mM, f_{ads} approaches 97%, indicating that the vast majority of bulk DS^- has been consumed in the HFRE process through adsorption onto newly created nanodroplet interfaces. By substituting eq 2.7 into the expression for f_{ads} and using the fit parameters from the fit in Figure 2.5B, we also plot a line describing $f_{ads}(C_{b,i})$ in Figure 2.5C. If $C_{b,i}$ is specified, then

this line describes the relative partitioning of DS^- between interfacial and bulk phases in the post-HFRE NEM for the particular conditions of HFRE that we have used.

For the post-HFRE NEMs, we reparametrize $\langle a(C_{b,i})\rangle$ from Figure 2.5A into $\langle a(C_{b,f})\rangle$, shown in Figure 2.6A, using $C_{b,f}(C_{b,i})$ in Figure 2.5B. Using a power-law function similar to the one in eq 2.8, we can describe the measured trend as a function of $C_{b,f}$ well using:

$$<a> = <a_{b,f}^*>(C_{b,f}/C^*)^{-\beta}, \quad (2.9)$$

yielding fit parameters $\langle a_{b,f}^*\rangle = 36.4 \pm 0.3$ nm and $\beta = 0.117 \pm 0.006$ with $R^2 = 0.99$. Equation 2.9 is useful because this function can be substituted for a into eq 2.4 when fitting isotherm data $C_{s,f}(C_{b,f})$ to obtain $C_s°$ and K.

We co-plot all isotherm results from fractionated and unfractionated NEMs after scaling the surface concentrations using the measured Gibbs derivative based on the IFT in Figure 2.6B. The shape of the isotherm of the unfractionated nanoemulsions (i.e., rise and plateau) is in reasonable accord with the adjusted isotherm of the fractionated nanoemulsion.

2.5 Discussion

Our IFT measurements are in good agreement (i.e., less than 10% deviation) with those for a similar system reported by Kanellopoulos and Owen.[18] For the 10 cSt PDMS oil and water interface, we have measured 39.9 mN/m at 0 mM SDS and 12.5 mN/m at SDS's CMC. Kanellopoulos and Owen have reported values of 42.7 mN/m at 0 mM SDS and 12.7 mN/m at the CMC of SDS. From Figure 2.3, we calculated the surface concentration to be 0.87 molecule/nm^2 at 1.25 mM using the Gibbs isotherm expression, given above. The derivative that is used to determine this C_s was taken analytically using points from the polynomial fit around the lowest measured points on our isotherm. Since $\langle a\rangle$ of this NEM is much larger than the effective size of

DS^-, the interfacial curvature of the nanodroplets would most likely create only a minor deviation in the adsorbed surface concentration as compared to that of a perfectly flat interface. Therefore, we have used the measured IFT, based on a nearly flat interface, to adjust the surface concentration on the nanodroplets.

The surface concentrations that we have measured and adjusted, $C_s° \approx 2.3$ molecule/nm^2 at very large $C_{b,f}$ and $C_{s,f} \approx 1.8$ molecule/nm^2 at SDS's CMC, are in reasonable agreement with the surface concentrations of adsorbed DS^- on O/W interfaces reported in some other prior experiments. For example, an adsorption isotherm of DS^- onto hexadecane/water interfaces in unfractionated O/W emulsions at $\phi = 0.064$, prepared by ultrasonication and probed using highly systematic small-angle neutron scattering (SANS),[12] has a reported $C_{s,f} \approx 3.01 \times 10^{-10}$ mol/cm^2 (i.e., ≈1.8 molecule/nm^2) at the CMC.

Reported values of $C_{s,f}^{-1}$ for DS^- at aliphatic oil–water interfaces at the CMC based on a variety of different techniques range from as small as 44 Å^2/molecule by a titration method[26] to as large as 71 Å^2/molecule by the drop volume method.[27] Our measured and IFT-normalized value of $C_{s,f}^{-1} \approx 55$ Å^2/molecule for DS^- adsorbed onto 10 cSt PDMS O/W interfaces is within this range. Using the drop-volume method[28] and the drop-shape analysis method[29] of measuring surface tension, the adsorption of DS^- from a bulk aqueous phase onto *n*-alkane/water interfaces (i.e., ranging from hexane to heptadecane) has been examined. For $C_{b,f} = C^*$, the conversion of this surface tension into an adsorbed surface concentration yielded $C_{s,f}^{-1} \approx 45$–51 Å^2/molecule for both methods. Our range of $A° \approx 43 \pm 9$ Å^2/molecule is in reasonable agreement with this prior published range.

Accurately measuring the total surface area of all droplets in a nanoemulsion is necessary in order to calculate quantitatively valid surface concentrations, from which an isotherm could

then be reliably constructed without reference to IFT measurements. In our experiments, there are several sources of systematic error that appear to have led to inaccuracies in measuring this total surface area. DLS provides an intensity-weighted average hydrodynamic radius according to the Stokes–Einstein relation (i.e., the first cumulant).[30-31] However, for the purposes of determining the total droplet surface area, using an average bare radius weighted by surface area and not intensity would be more appropriate. In addition, the width and shape of the droplet size distribution can play a role if one seeks to obtain surface-area-weighted $\langle a \rangle$ instead of intensity-weighted $\langle a \rangle$. The log-normal function is frequently used to characterize monomodal size distributions, and in this case, the surface-area-weighted $\langle a \rangle$ will be smaller than the intensity-weighted $\langle a \rangle$.[31-33] Moreover, even after converting from intensity-weighted to surface-area-weighted hydrodynamic $\langle a \rangle$, the bare radius, corresponding to that for adsorption, is a few nanometers smaller than this hydrodynamic $\langle a \rangle$ since the hydrodynamic radius effectively includes a thin shell of water and screening counterions which move together with the droplets as they diffuse.[34] Taken together, corrections both for weighting and for hydrodynamic aspects would combine to reduce $\langle a \rangle$, leading to a more accurate determination of a larger measured total surface area for adsorption compared to what we have measured and reported using intensity-weighted hydrodynamic $\langle a \rangle$. Thus, for fixed ϕ, this lower value of $\langle a \rangle$ would increase the total surface area in the nanoemulsion compared to what we have used, and this would simply reduce all values of measured $C_{s,f}$ in the isotherm by a constant factor. While we have accounted for this factor by adjusting $C_{s,f}$ values in the isotherm using the Gibbs derivative of IFT measurements, in principle it may be possible in future experiments to avoid pinning the scale of $C_{s,f}$ in the isotherm to this Gibbs derivative entirely if a better characterization of surface-area-weighted bare $\langle a \rangle$ can be obtained.

While fractionated nanoemulsions were not used by James-Smith et al.,[13] they demonstrated a loss of DS^- from the bulk to the interfaces of microscale and submicroscale hexadecane droplets (i.e., $\langle a \rangle > 200$ nm measured using DLS) in unfractionated polydisperse O/W emulsions made by vortex mixing. They measured surfactant concentrations using optical absorption based on the complexing of cationic methylene blue dye with DS^-. As a consequence of their unknown size distributions and total surface areas, they did not report absolute surface densities but instead used pre-existing literature values in constructing $C_s°$ in their isotherm (see Figure 5 of James-Smith et al., based on $A° = 50$ Å^2/molecule reported by Kong et al.[35]), which showed only saturation behavior at high $C_{b,f}$, thereby precluding any independent experimental determination of K. Moreover, their reported $C_{b,f}$ versus $C_{b,i}$ (see Figure 3 of James-Smith et al.) was fit to a straight line rather than the quadratic form of eq 2.7 that we have shown to match our measured $C_{b,f}$ versus $C_{b,i}$ over a wider range of $C_{b,i}$ very well. (See Figure 2.5B herein.) This quadratic form is based on a Langmuir isotherm equation, and the trends over a wide range of $C_{b,i}$ are clearly nonlinear.

There are some similarities between the method employed by James-Smith et al. and our method. Both methods use centrifugal filtration to separate the emulsion droplets from the BCP, and the surface concentration relies on measuring initial and final surfactant concentrations; however, the method provided herein is an improvement over James-Smith et al.'s method. This improvement can, in part, be attributed to the use of fractionated nanoemulsion droplets and the manner in which the system reached equilibrium. In addition, by using concentrated nanoemulsions which have smaller droplet radii ($<a> \approx 40$ nm), we have increased the total surface area per volume by more than an order of magnitude over that in all prior experiments. We also employ the novel use of Sr complexation to determine the SDS concentration in stable NEMs,

although we also use conductivity to track the bulk electrolyte concentration of our NEM as it approaches equilibrium. We have developed a simplified description of partitioning (i.e., eqs 2.1–2.7) based on a Langmuir isotherm equation. Empirically, this description provides reasonable fits to trends in our measured post-HFRE $C_{b,f}$ as a function of $C_{b,i}$ (Figure 2.5B). Since obtaining highly accurate measurements of the total surface area of nanoemulsions can be challenging, we have relied upon IFT measurements to determine, through the Gibbs derivative, an accurate magnitude of $C_{s,f}$ at low $C_{b,f}$.

By using a fractionated NEM, we have measured the partitioning of amphiphilic DS^- ions onto PDMS O/W interfaces at room temperature, yielding a quantitative adsorption isotherm which is reasonably described by a Langmuir isotherm equation. Moreover, NEMs offer the advantage of a much larger surface area/volume ratio as compared to that of microscale emulsions, making adsorption effects much more pronounced for the same total volume at the same ϕ. Our measurements are macroscopic in nature, yet they provide a quantitative measure of the equilibrium adsorbed surface density (i.e., $C_{s,f}$) of charged surfactant ions that stabilize the nanodroplets. The techniques that we have developed are appropriate for many different surfactants other than SDS and immiscible oils other than PDMS, but these techniques are primarily directed toward simple ionic surfactants that are soluble in water but insoluble in oil. We anticipate that these techniques can be readily adapted to a useful yet limited range of other oils and surfactants.

Our results have important implications for those who make nanoemulsions using HFRE. The final bulk surfactant concentration after HFRE is typically not the same as the initial bulk surfactant concentration, as we have demonstrated in Figure 2.5B. The degree of partitioning of the surfactant to O/W interfaces in emulsions depends on many factors. These include ϕ, the

emulsification conditions (e.g., chamber type and channel dimensions, operating peak pressure, number of passes, and temperature), and the final post-HFRE droplet size distribution, from which $\langle a \rangle$ may be an inadequate description since all of these factors can affect the total surface area in the post-HFRE nanoemulsion. Charge interactions, although screened, can still play a major role in the adsorption of charged amphiphiles onto interfaces, especially at high surface concentrations. Our results clearly demonstrate that the bulk surfactant concentration is not the same before and after HFRE in a nondilute nanoemulsion system; even for modest ϕ, $C_{b,f}$ is typically smaller than $C_{b,i}$ and in some cases very substantially by more than an order of magnitude. Using data from Figure 2.5B, we have plotted the measured f_{ads} (points) and also have shown the calculated f_{ads} (line) in Figure 2.5C using the same $C_s°$ and K determined by fitting in Figure 2.5B. At low $C_{b,i}$, after HFRE much of the surfactant has repartitioned to the newly created surfaces of the nanodroplets, leaving very little remaining in the bulk continuous phase. Our measurements are consistent with a $C_{b,f}$ /$C_{b,i}$ ratio that is nearly constant and remains in the range from ~0.03 to ~0.05 for $C_{b,i}$ < 100 mM at fixed ϕ = 0.15. In this same range of $C_{b,i}$ < 100 mM, f_{ads} also remains nearly constant and ranges from ~0.97 to ~0.95. Therefore, in this range, the surfactant on a mole basis predominantly partitions to the surfaces of droplets in the NEM. By contrast, for larger $C_{b,i}$ > 100 mM at the same fixed ϕ, some limited repartitioning of DS^- from the bulk continuous phase to the surfaces of droplets in the NEM occurs, yet a relatively larger percentage of surfactant on a mole basis remains in the bulk continuous phase and so f_{ads} decreases.

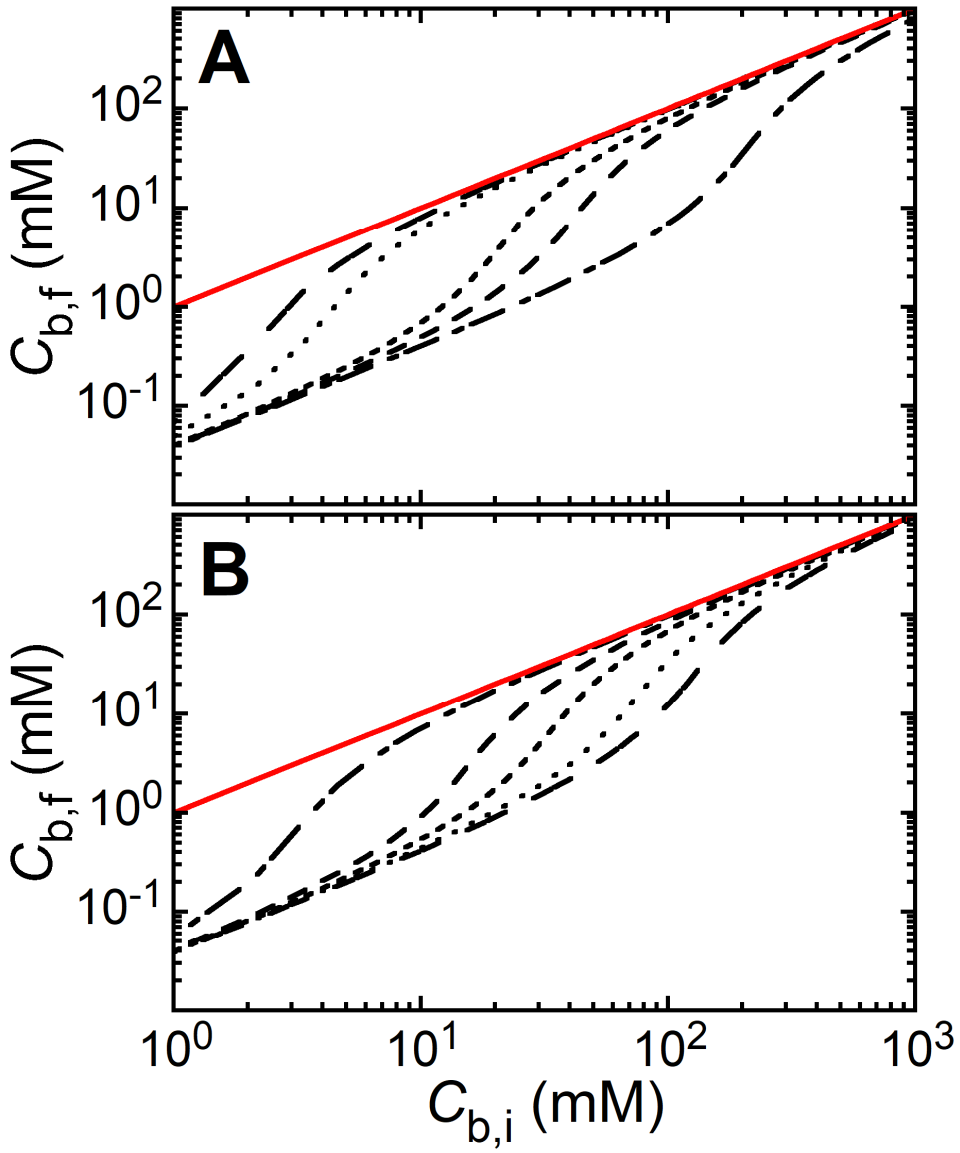

Figure 2.7. Final bulk DS^- concentration, $C_{b,f}$, calculated using eq 2.7 as a function of the bulk initial DS^- concentration, $C_{b,i}$. K and $C_s°$ values are from the fit to the adjusted isotherm in Figure 2.4. (A) Calculated $C_{b,f}(C_{b,i})$ for emulsions having fixed ϕ = 0.15 and different monodisperse radii (in order from right to left, black): a = 10, 50, 100, 500, and 1000 nm. **(B)** Calculated $C_{b,f}(C_{b,i})$ for emulsions having a fixed monodisperse radius a = 40 nm and different droplet volume fractions (in order from left to right, black): ϕ = 0.01, 0.05, 0.10, 0.20, and 0.30. Red lines in parts (A) and (B): zero adsorption line, $C_{b,f} = C_{b,i}$ (for reference).

Using parameters for K and $C_s°$ obtained from the fit to the adjusted isotherm (solid black line) in Figure 2.4, we can predict the behavior of $C_{b,f}$ as a function of $C_{b,i}$ for DS^- adsorbed onto

droplet interfaces of monodisperse PDMS O/W emulsions and nanoemulsions. In Figure 2.7A, we plot predictions for $C_{b,f}(C_{b,i})$, based on eq 2.7, for a series of different values of a, keeping $\phi = 0.15$ fixed. As a decreases from the microscale to the nanoscale regime and the total surface area of droplets increases, the transition region where $C_{b,f}$ becomes significantly less than $C_{b,i}$ shifts toward larger $C_{b,i}$. At very large $C_{b,i}$, we recover $C_{b,f} \approx C_{b,i}$ (red line in Figure 2.7A), indicating that there is such an excess of surfactant in the bulk that adsorption onto droplet interfaces is negligible by comparison. However, at very small $C_{b,i}$, where interfacial adsorption is dominant, the calculated curves all approach a well-defined line having a slope of 1 on the log–log plot. This line lies a factor of K below the red line, indicating that K controls the reduction in $C_{b,f}$ relative to $C_{b,i}$ in this surface-dominated limit. Conversely, in Figure 2.7B, we also show examples of the calculated $C_{b,f}(C_{b,i})$ for different ϕ by keeping $a = 40$ nm fixed. As ϕ is increased, the transition region where $C_{b,f}$ becomes significantly less than $C_{b,i}$ shifts toward larger $C_{b,i}$. This indicates that the increasing surface area in the nanoemulsion toward larger ϕ at fixed volume is adsorbing more surfactant molecules from the bulk, thereby reducing $C_{b,f}$ more. Again, in the limit of extremely high $C_{b,i}$, all of the curves approach $C_{b,f} \approx C_{b,i}$ (see red line in Figure 2.7B), and at very low $C_{b,i}$, the ratio given by $C_{b,f}/C_{b,i}$ approaches $1/K$.

In addition, using eq 2.7 and values of K and $C_s°$ from the fit in Figure 2.4, we calculate the fraction of DS^- adsorbed onto droplet interfaces over a wide range of a for ideally monodisperse emulsions at fixed $C_{b,i} = C^*$. In Figure 2.8A, we plot $f_{ads}(a)$ for a series of different ϕ values. Only a small fraction of the surfactant is adsorbed onto the surfaces of the droplets for microscale and larger emulsions, whereas for submicrometer and especially nanoscale emulsions

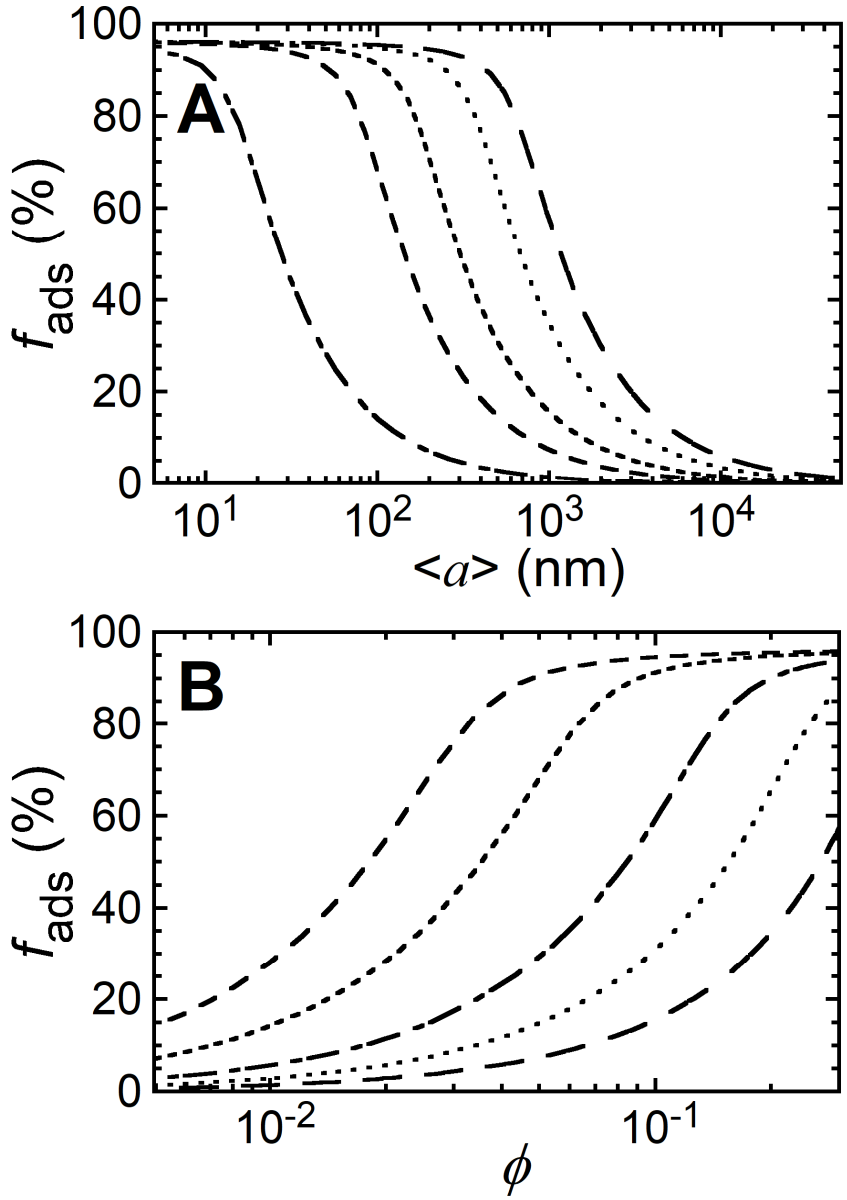

Figure 2.8. Adsorbed fraction f_{ads} of DS^- on PDMS oil/water droplet interfaces after HFRE calculated using eq 2.7 and $f_{ads} = 1 - (C_{b,f}/C_{b,i})$ for fixed $C_{b,i} = C^* = 8.1$ mM and values of K and $C_s°$ from the fit to the adjusted isotherm in Figure 2.4. (A) Calculated $f_{ads}(a) = f_{ads}(\langle a \rangle)$ for emulsions having different droplet volume fractions (in order from left to right): ϕ = 0.01, 0.05, 0.10, 0.20, and 0.30. **(B)** Calculated $f_{ads}(\phi)$ for emulsions having different average droplet radii (in order from left to right): a = 50, 100, 250, 500, and 1000 nm.

a very high percentage of the surfactant in the system has partitioned to the interfaces of the droplets. In the limit of very small a, f_{ads} approaches $(1 - K^{-1}) \times 100\% \approx 97\%$. Likewise, in Figure 2.8B, we plot $f_{ads}(\phi)$ for a series of different a values at fixed $C_{b,i} = C^*$; as ϕ increases, the total

surface area of the droplet interfaces also increases, which leads to a larger fraction of adsorbed DS^-. For the same ϕ, nanoemulsions have a much larger f_{ads} than microscale and larger emulsions because nanoemulsions have a much greater total surface area of droplet interfaces.

While these detailed measurement and results provide a clear empirical picture of surfactant partitioning for a well-defined case of HFRE applied to oil-in-water NEMs, many important questions remain. For instance, when considering different nanoemulsion systems that cover a wide range of other types of surfactants, the isotherm equations may be more sophisticated and complex than Langmuir's isotherm. However, we have provided the general framework upon which such complex isotherm models might be used in the context of post-HFRE nanoemulsions in order to obtain different functional dependences of $C_{b,f}$ versus $C_{b,i}$. Such equations describing the partitioning of surfactant based on these more sophisticated isotherms could be solved numerically, if necessary. Regarding a different question, to the best of our knowledge, there is no analytical theory that treats the changes in partitioning among monomers, micelles, and adsorbed surfactant due to significant increases in the droplet interfacial area caused by HFRE. Such changes are usually negligible when forming microscale emulsions, yet could be quite significant in nanoemulsions. A more advanced treatment could potentially capture the nonequilibrium transport features of flow-induced droplet rupturing and coalescence in a micellar solution, along with the adsorption and desorption of surfactant from the dynamically changing interfaces during the process of HFRE itself.

2.6 Conclusion

We have developed an experimental method for quantifying the interfacial and bulk partitioning of a nonvolatile amphiphilic surfactant, soluble only in the BCP, in a fractionated silicone oil-in-water NEM system after HFRE. The total surface area of droplet interfaces, as a

premix emulsion at a sufficiently large yet fixed ϕ is transformed into a nanoemulsion through HFRE, dramatically increases. In turn, these newly created droplet interfaces can adsorb a very high percentage of the surfactant from the bulk, causing the equilibrium $C_{b,f}$ to be reduced far below $C_{b,i}$. Beyond demonstrating this experimentally, we have also combined the Langmuir isotherm equation with an emulsification scenario at fixed ϕ and the total number of moles of surfactant, leading to useful equations for predicting changes in the post-HFRE partitioning of surfactant for nanoemulsions.

Even given these advances, there are still many complexities related to the thermodynamics of surfactant adsorption in real emulsion systems that require further attention. For example, the role of micelles of DS^- in the BCP for $C_{b,f}$ > CMC has not been directly addressed, and these micelles alter the effective osmotic pressure of monomeric DS^- in the BCP. Micelle formation could have a significant impact on the largest attainable saturated surface concentration. Our experiments provide at least preliminary evidence that micelles present in the premix emulsion can be entirely consumed through surface adsorption during the process of HFRE, even for $C_{b,i}$ far above the CMC.

In the future, further reducing the size polydispersity through additional fractionation steps and better characterizing the post-HFRE droplet size distribution, for instance, using a real-space technique such as cryoelectron microscopy, may enable more exact determinations of a nanoemulsion's total surface area, thereby obviating the need for independent IFT measurements. The DLS measurements might be further improved to provide a robust determination of the intensity-weighted geometric mean radius and geometric mean standard deviation of a log-normal distribution and then determine the surface-area-weighted $\langle a \rangle$ using these parameters.[32] An additional minor correction when converting from a hydrodynamic to a bare radius might further

improve the accuracy of the total surface area in the nanoemulsion. It would be interesting to apply this fractionation–precipitation–conductivity protocol to study the adsorption of other anionic and cationic surfactants as well as nonvolatile nonionic, zwitterionic, and polymeric surfactants on a variety of different O/W interfaces. These measurements could potentially be compared with predictive theoretical models or simulations of surfactant adsorption energies. In addition, exploring how salts, such as NaCl, which can be controlled over a wide range of concentrations, affect surfactant adsorption and partitioning would also be interesting. While the Langmuir isotherm sufficiently describes the simple ionic surfactant SDS, it is possible that other isotherms could be required to fully describe the adsorption characteristics of more complex interfacially active species. Beyond equilibrium adsorption, additional experiments and simulations are needed to explore the complex dynamic effects of surfactant partitioning during extreme HFRE, in which even nanoscale droplets can deform significantly.

References

1. Becher, P., *Emulsions: Theory and Practice*. 2nd ed.; Reinhold: New York, 1965.
2. Bibette, J.; Calderon, F. L.; Poulin, P., Emulsions: Basic Principles. *Rep. Prog. Phys.* **1999,** *62* (6), 969-1033.
3. Israelachvili, J. N., *Intermolecular and Surface Forces*. 2nd ed.; Academic Press: London, 2002.
4. Mason, T. G.; Wilking, J. N.; Meleson, K.; Chang, C. B.; Graves, S. M., Nanoemulsions: Formation, Structure, and Physical Properties. *J. Phys.: Condens. Matter* **2006,** *18*, R635-R666.
5. Meyers, D., *Surfaces, Interfaces, and Colloids*. 2nd ed.; Wiley: New York, 1999.
6. Taylor, P., Ostwald Ripening in Emulsions. *Advances in Colloid and Interface Science* **1998,** *75* (2), 107-163.
7. Bibette, J.; Morse, D. C.; Witten, T. A.; Weitz, D. A., Stability Criteria for Emulsions. *Phys. Rev. Lett.* **1992,** *69*, 2439-2442.
8. Walstra, P., Emulsion Stability. In *Encyclopedia of Emulsion Technology*, Becher, P., Ed. Marcel Dekker: New York, 1996; Vol. 4, pp 1-62.
9. Wilking, J. N.; Mason, T. G., Irreversible Shear-Induced Vitrification of Droplets into Elastic Nanoemulsions by Extreme Rupturing. *Phys.l Rev. E* **2007,** *75* (4), 041407.
10. Mason, T. G.; Graves, S. M.; Wilking, J. N.; Lin, M. Y., Effective Structure Factor of Osmotically Deformed Nanoemulsions. *J. Phys. Chem.* **2006,** *110*, 22097-22102.
11. Cosgrove, T.; Phipps, J. S.; Richardson, R. M., Neutron Reflection from a Liquid/Liquid Interface. *Colloids Surf.* **1992,** *62*, 199-206.
12. Staples, E.; Penfold, J.; Tucker, I., Adsorption of Mixed Surfactants at the Oil-Water Interface. *J. Phys. Chem. B* **2000,** *104*, 606-614.

13. James-Smith, M. A.; Alford, K.; Shah, D. O., A Novel Method to Quantify the Amount of Surfactant at the Oil/Water Interface to Determine Total Interfacial Area of Emulsions. *J. Colloid Interface Sci.* **2007,** *310*, 590-598.
14. Carroll, M. K.; Unger, M. A.; Leach, A. M.; Morris, M. J.; Ingersoll, M.; Bright, F. V., Interactions Between Methylene Blue and Sodium Dodecyl Sulfate in Aqueous Solution Studied by Molecular Spectroscopy. *Appl. Spectrosc.* **1999,** *53*, 780-784.
15. Jurado, E.; Fernandez-Serrano, M.; Nunez-Olea, J.; Luzon, G.; Lechuga, M., Simplified Spectrophotometric Method Using Methylene Blue for Determining Anionic Surfactants: Applications to the Study of Primary Biodegradation in Aerobic Screening Tests. *Chemosphere* **2006,** *65*, 278-285.
16. Mukerjee, P., Use of Ionic Dyes in the Analysis of Ionic Surfactants and Other Ionic Organic Compounds. *Anal. Chem.* **1956,** *28*, 870-873.
17. Zaghbani, N.; Hafiane, A.; Dhahbi, M., Separation of Methylene Blue from Aqueous Solution by Micellar Enhanced Ultrafiltration. *Sep. Purif. Technol.* **2007,** *55*, 117.
18. Kanellopoulos, A.; Owen, M., Adsorption of Sodium Dodecyl Sulphate at Silicone Fluid/Water Interface. *Trans. Faraday Soc.* **1971,** *67*, 3127.
19. Martínez-Balbuena, L.; Arteaga-Jiménez, A.; Hernández-Zapata, E.; Márquez-Beltrán, C., Applicability of the Gibbs Adsorption Isotherm to the Analysis of Experimental Surface-Tension Data for Ionic and Nonionic Surfactants. *Adv. Colloid Interface Sci.* **2017,** *247*, 178-184.
20. Chang, C.-H.; Franses, E. I., Adsorption Dynamics of Surfactants at the Air/Water Interface: a Critical Review of Mathematical Models, Data, and Mechanisms. *Colloids Surf. A* **1995,** *100*, 1-45.

21. Meleson, K.; Graves, S.; Mason, T. G., Formation of Concentrated Nanoemulsions by Extreme Shear. *Soft Mater.* **2004,** *2* (2-3), 109-123.

22. Scheffold, F.; Mason, T. G., Scattering from Highly Packed Disordered Colloids. *J. Phys.: Condens. Matter* **2009,** *21* (33), 332102.

23. Miyamoto, S., The Effect of Metallic Ions on Surface Chemical Phenomena. III. Solubility of Various Metal Dodecyl Sulfates in Water. *Bull. Chem. Soc. Jpn* **1960,** *33* (3), 371-375.

24. Duplâtre, G.; Ferreira Marques, M. F.; da Graça Miguel, M., Size of Sodium Dodecyl Sulfate Micelles in Aqueous Solutions as Studied by Positron Annihilation Lifetime Spectroscopy. *J. Chem. Phys.* **1996,** *100* (41), 16608-16612.

25. Zuidema, H.; Waters, G., Ring Method for the Determination of Interfacial Tension. *Ind. Eng. Chem., Anal. Ed.* **1941,** *13* (5), 312-313.

26. Cockbain, E. G., The Adsorption of Sodium Dodecyl Sulphate at the Oil-Water Interface and Application of the Gibbs Equation. *Trans. Faraday Soc.* **1954,** *50* (0), 874-881.

27. Deshiikan, S. R.; Bush, D.; Eschenazi, E.; Papadopoulos, K. D., SDS, Brij58 and CTAB at the Dodecane-Water Interface. *Colloids Surf., A* **1998,** *136* (1), 133-150.

28. Rehfeld, S. J., Adsorption of Sodium Dodecyl Sulfate at Various Hydrocarbon-Water Interfaces. *J. Phys. Chem.* **1967,** *71* (3), 738-745.

29. Gurkov, T. D.; Dimitrova, D. T.; Marinova, K. G.; Bilke-Crause, C.; Gerber, C.; Ivanov, I. B., Ionic Surfactants on Fluid Interfaces: Determination of the Adsorption; Role of the Salt and the Type of the Hydrophobic Phase. *Colloids Surf., A* **2005,** *261* (1), 29-38.

30. Koppel, D. E., Analysis of Macromolecular Polydispersity in Intensity Correlation Spectroscopy: The Method of Cumulants. *J. Chem. Phys.* **1972,** *57* (11), 4814.

31. Nobbmann, U.; Morfesls, A., Light Scattering and Nanoparticles. *Mater. Today* **2009,** *12* (5), 52-54.

32. Douglas, S. J.; Illum, L.; Davis, S. S.; Krueter, J., Particle Size and Size Distribution of Poly(butyl-2-cyanoacrylate) Nanoparticles: I. Influence of Physicochemical Factors. *J. Colloid Interface Sci.* **1984,** *101* (1), 149-158.

33. Thomas, J. C., The Determination of Log Normal Particle Size Distributions by Dynamic Light Scattering. *J. Colloid Interface Sci.* **1986,** *117* (1), 187-192.

34. Sasaki, S., Effect of Simple Electrolytes on the Hydrodynamic Radius of Polystyrene Latex. *Colloid Polym. Sci.* **1984,** *262*, 406-408.

35. Kong, L.; Beattie, J. K.; Hunter, R. J., Electroacoustic Study of n-Hexadecane/Water Emulsions. *Aust. J. Chem* **2002,** *54* (8), 503-511.

Chapter 3 - Hyperuniform Photonic Nanoemulsions and Biliquid Opals

3.1 Introduction

Brilliant gemstone opals[1] are inorganic solids containing highly ordered crystallites[2,3] of sub-micron hyperuniform[4] photonic structures[5] that strongly separate illuminating white light into intense flashes of vibrant colors by wavelength-selective Bragg diffraction[6] at backscattering angles. Beyond natural opals, synthetic opals[7,8] have been produced by ordering solid monodisperse colloidal nanoparticles[9,10] through self- and directed-assembly methods, yielding colloidal crystals[11-16]. Microfluidic technologies can produce highly monodisperse droplets of one liquid in a continuous liquid phase that is immiscible[17], thereby forming ordered emulsions reminiscent of Bragg's bubble rafts[18]. Yet, such droplets typically have microscale diameters and are thus too large for creating gemstone-like opalescence, although internal reflection and interference from curved interfaces in multi-phase droplets can produce color[19]. While colored

one-dimensional crystals have been created by magnetically inducing attractive assembly of depletion-fractionated sub-micron ferrofluid droplets into chains[20], and a thin layer of ordered gas nanobubbles in solid polymer films also generates structural color[21], synthesizing long-lived photonic nanoemulsions that are composed only of non-absorbing liquids, yet exhibit the exquisite beauty of solid opals through controllable color-selective backscattering Bragg diffraction in the visible wavelength range from highly charge-repulsive three-dimensional crystallites of nanodroplets, has not yet been achieved. Here, we make monodisperse oil-in-water nanoemulsions[22,23] that are stablized by an ionic surfactant having a sufficiently long tail, which precludes significant desorption upon dilution with deionized water, and thereby create ordered biliquid opals as well as structurally colored hyperuniform disordered states. By systematically controlling the average size and volume fraction of nanodroplets while ensuring droplet stability at highly reduced ionic strengths through a process that we call rejamming crystallization, we achieve long-lived photonic biliquid opals that exhibit tunable and brilliant color-selective backscattering of visible and ultraviolet light. Such photonic nanoemulsions extend the range of hyperuniform ordered and disordered materials to entirely liquid compositions, leading to exciting possibilities for controlling the visual appearance and color of biliquid soft-matter systems without absorbing dyes.

3.2 Results

To make photonic oil-in-water (O/W) nanoemulsions, we use a combination of high flow-rate emulsification[23] (HFRE) to reach nanoscale average droplet radii $\langle a \rangle$, subsequent centrifugal fractionation[23,24] to reduce droplet size polydispersity $\delta a/\langle a \rangle$, and centrifugal deionization to reduce the ionic strength I in the continuous aqueous phase (see 3.4 Methods, Table S3.1, Fig. 3.1a). Hot HFRE is performed at a temperature $T_{HFRE} \approx 50$ °C using a long-tail ionic surfactant,

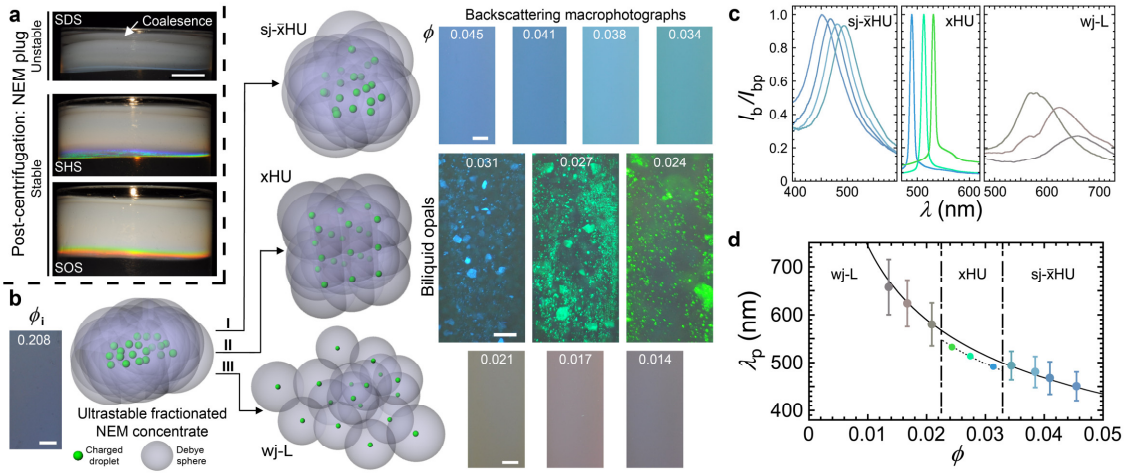

Figure 3.1 Photonic crystalline and non-crystalline hyperuniform structures of ultrastable fractionated ionic oil-in-water (O/W) nanoemulsions. a, Size-fractionated poly-dimethylsiloxane (PDMS) O/W nanoemulsions made using sodium dodecyl sulfate (SDS) surfactant coalesce after repeated centrifugation and dilution with deionized water to reduce ionic strength I. Using higher carbon-number surfactants sodium hexadecyl sulfate (SHS) and sodium octadecyl sulfate (SOS) yields ultrastable PDMS O/W nanoemulsions since HS^- and OS^- adsorption onto droplet interfaces is effectively irreversible (see 3.4 Methods, Figure S3.1). Small multi-color bands are observed at the bottoms of the SHS and SOS plugs. Scale bar: 5 mm (same for all images). **b,** Fractionated SOS-stabilized PDMS O/W nanoemulsion concentrate having average droplet radius $\langle a \rangle$ = 47.8 nm (A211, ϕ_i = 0.21, see Table S3.1 at reduced I (backscattering macrophotograph BMP, left) is diluted with different volumes of deionized water in a final step, lowering the final droplet volume fraction ϕ as well as I (schematic, see 3.4 Methods). Less dilution (path I) yields electrostatic strongly jammed non-crystalline hyperuniform (sj-x̄HU) disordered nanodroplet structures which have strong photonic colors and a uniform appearance (BMPs, upper right). Debye spheres around charged nanodroplets highly overlap, indicating strong electrostatic repulsion relative to thermal energy k_BT. More dilution (path II) yields crystalline hyperuniform (xHU) ordered nanodroplet structures that exhibit brilliant monochromatic opalescence as a consequence of Bragg scattering from a subset of crystallites having specific orientations (BMPs, middle right). Even more dilution (path III) yields weakly jammed liquid-like (wj-L) disordered nanodroplet structures that uniformly display only muted colors (BMPs, lower right). White scale bars: 1.0 mm. **c,** Visible backscattering spectra (intensity I_b normalized by peak intensity I_{bp} versus light wavelength λ, see 3.4 Methods) of photonic sj-x̄HU (left), xHU (center), and wj-L (right) nanoemulsions. Curves are color coded to BMPs in part b; xHU spectra exhibit very narrow peaks which are all normalized to unity. Peaks of disordered sj-x̄HU and wj-L structures are on a common intensity scale to show higher color saturation of sj-x̄HU, and only the peak at ϕ = 0.045 set to unity. **d,** Peak wavelength λ_p (circles, color coded to BMPs in part b) from backscattering spectra in part c as a function of ϕ. Bars: end-to-end length represents full-width-at half-maximum (FWHM) of spectral peaks. Vertical long/short-dash lines: separate wj-L, xHU, and sj-x̄HU regimes by ϕ. Solid curve: fit of $\lambda_p(\phi)$ for disordered sj-x̄HU and wj-L to $C_{\bar{x}}\langle a \rangle/\phi^{1/3}$ ($C_{\bar{x}}$ = 3.34 ± 0.01, R^2 = 0.994, see text). Dotted curve: fit of $\lambda_p(\phi)$ for ordered xHU to $C_x\langle a \rangle/\phi^{1/3}$ (C_x = 3.236 ± 0.005, R^2 = 0.996, see text).

such as sodium octadecyl sulfate (SOS), that has a higher solubility and greater capacity to adsorb onto newly created droplet interfaces. Alternatively, O/W nanoemulsions made by HFRE at room temperature ($T_r \approx 23$ °C) using a smaller chain length surfactant, such as sodium dodecyl sulfate (SDS), can be surfactant-exchanged through competitive adsorption-desorption using a heated SOS solution at $T_{exch} \approx 75$ °C, thereby populating nanodroplet surfaces predominantly with SOS. The resulting hot nanoemulsion is then cooled to room temperature, which greatly reduces the SOS desorption rate from droplet interfaces and confers a high degree of stability to the droplets through screened charge repulsion even after repeatedly fractionating and centrifugally deionizing (see 3.4 Methods, Figs. S3.1 and S3.2). The resulting nanoemulsion droplets have zeta potentials[25,26] ζ in the range from about -45 mV to -55 mV (see 3.4 Methods, Table S3.1) and remain stable against coalescence even when concentrated to high droplet volume fractions ϕ even after significant deionization. Such ultra-stable fractionated nanoemulsions (USF-NEMs) thus overcome limitations of desorption of other more common ionic surfactants that have shorter tails (e.g. SDS), which leads to droplet coalescence while lowering I through deionization, yet also provide reduced $\delta a/\langle a \rangle$ known to facilitate crystallization of charged solid colloidal particles through electrostatic repulsion[11]. Moreover, this highly parallel fabrication protocol provides bulk quantities of concentrated USF-NEMs of a variety of oils and long-chain surfactants that can be used for many different purposes, including exploring nanodroplet self-assembly and structure-dependent photonic material properties.

Starting with a concentrated washed USF-NEM, composed of jammed disordered droplets of poly-dimethylsiloxane (PDMS, Gelest; viscosity: 10 cSt; refractive index: $n = 1.40$) silicone oil and stabilized by SOS, we systematically dilute aliquots to different final ϕ using deionized water

(see 3.4 Methods, Fig. 3.1b). The range of final ϕ have been chosen to set average interdroplet center-to-center separations, $\langle r \rangle$, lower than but in the vicinity of the wavelength of light, λ, in the visible range, yet substantially larger than $\langle a \rangle$. The final I is low enough that the Debye screening length[26] λ_D associated with the repulsion between the charged nanodroplets is proximate to or in excess of $\langle r \rangle$, leading to strongly repulsive pair interactions compared to thermal energy $k_B T$, where k_B is Boltzmann's constant and T is the temperature, for all but the largest dilution volumes. Moreover, $\langle a \rangle / \lambda_D$ is typically considerably less than unity. For higher final ϕ, when directionally illuminating the diluted USF-NEMs with white light and observing backscattering macrophotographs (BMPs, see 3.4 Methods), we find vibrantly colored nanoemulsions (Fig. 3.1b), corresponding to strongly jammed[27,28] non-crystalline hyperuniform (sj-$\bar{x}$HU) droplet structures which do not have long range order but do have a very regular distribution of interdroplet separations. This hyperuniformity is also revealed through peaks in the measured optical backscattering spectra (OBS, 3.4 Methods, Fig. 3.1c-left). At intermediate ϕ, strikingly, we find a regime of differently colored self-assembled biliquid opals containing crystallites that all exhibit a single monochromatic opalescence in backscattering (Fig. 3.1c-center). We call this process of forming such biliquid opals of repulsive droplets by reducing ϕ and I 'rejamming crystallization', and these photonic nanoemulsions have crystalline hyperuniform structures (xHU). Further evidence of Bragg scattering from photonic xHU nanoemulsions is seen in the OBS, which have extraordinarily narrow peaks, even compared to sj-$\bar{x}$HU structures. Biliquid opals exhibit iridescence, or variation in selectively scattered color from xHU crystallites as the angle between the illumination and detector is varied away from 180 degrees, consistent with Bragg's scattering law (see 3.4 Methods, Fig. S3.3). At even higher dilutions and lower ϕ, the crystallites no longer form as a consequence of weakened repulsion, caused by larger interdroplet spacing compared to

λ_D, and we observe hazy and weak colors that result from a combination of multiple scattering as well as a very broad peak that moves progressively out towards infrared (IR) wavelengths (Fig. 3.1c-right). The droplet structure after very high dilution is disordered, at best weakly jammed and liquid-like (wj-L), and the presence of significant multiple scattering (loss of color saturation and increasingly milky appearance) indicates that strict hyperuniformity is lost for high dilutions towards gas-like ϕ well beyond the xHU region.

Disordered structures can be differentiated from ordered xHU by fitting the observed peak wavelengths λ_p versus a length scale $\langle a \rangle / \phi^{1/3}$, proportional to nearest-neighbor $\langle r \rangle$ (Fig. 3.1d). The coefficients for fits $\lambda_p = C\langle a \rangle / \phi^{1/3}$ to disordered and ordered structures (solid and dashed lines, respectively) are: $C_{\bar{x}} = 3.34 \pm 0.01$ (correlation coefficient: $R^2 = 0.994$) and $C_x = 3.236 \pm 0.005$ ($R^2 = 0.996$). The clear discontinuity in λ_p going from sj-$\bar{x}$HU to xHU regions indicates that nanodroplets can temporarily unjam and self-organize into xHU and then rejam in an ordered state that is both thermodynamically favored and also kinetically accessible over a limited range of ϕ. At kinetically accessible ϕ, crystallization lowers the electrostatic contribution to the system's free energy yet becomes increasingly frustrated by higher levels of polydispersity, which reduces the degree of crystallinity (see Fig. S3.4).

By controlling both $\langle a \rangle$ and ϕ of USF-NEMs formed by rejamming crystallization, we are able to systematically tune the backscattering color of crystallites in the biliquid opals seen in the BMPs (Fig. 3.2a) as well as the primary peak wavelength λ_{p1} in the OBS over the entire visible range (Fig. 3.2b), and even into the ultraviolet (UV, see Fig. S3.5). The measured $\lambda_{p1}(\langle a \rangle / \phi^{1/3})$ from OBS can be fit by a simple line (see 3.4 Methods, Fig. 3.2c):

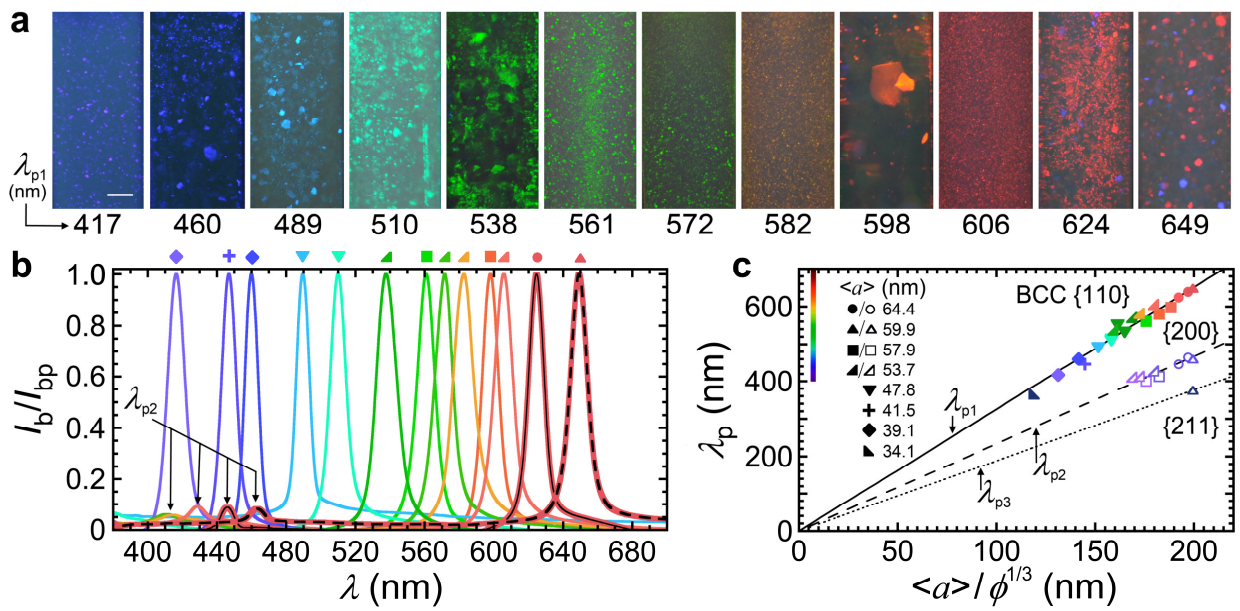

Figure 3.2 Controlling backscattered colors of crystalline biliquid opals through the volume fraction ϕ and average droplet radius $\langle a \rangle$ of fractionated nanoemulsions. a, Backscattering macrophotographs (BMPs) of crystalline hyperuniform (xHU) biliquid opals, made using path II in Fig. 3.1b, reveals monochromatic visible opalescence at lower primary peak wavelengths λ_{p1} and bichromatic visible opalescence for higher λ_{p1} near and above orange wavelengths. White scale bar: 1.0 mm (same for all images). **b,** Visible backscattering spectra (intensity I_b normalized by primary peak intensity I_{bp} versus light wavelength λ, see 3.4 Methods) of biliquid opals shown in part a. For larger λ_{p1}, smaller secondary peaks are also observed at visible wavelengths λ_{p2} (arrows). Symbol shapes above peaks designate $\langle a \rangle$ (see inset legend in part c, fractions identified in Table S3.1). **c,** Peak wavelengths λ_p from part b versus $\langle a \rangle/\phi^{1/3}$ for biliquid opals after final dilution (solid symbols: primary peaks λ_{p1}; open symbols: secondary peaks λ_{p2} and tertiary peaks λ_{p3}). Inset legend (upper left): symbol shape encodes $\langle a \rangle$; colors of visible λ_p are shown in a vertical bar. Solid line: Fit of solid symbols to $\lambda_{p1} = C_{p1}\langle a \rangle/\phi^{1/3}$ ($C_{p1} = 3.26 \pm 0.02$, $R^2 = 0.964$, see text), corresponding to 1st order Bragg backscattering from body-centered-cubic (BCC) with Miller indices {110}. Dashed line: fit of open λ_{p2} symbols to $\lambda_{p2} = C_{p2}\langle a \rangle/\phi^{1/3}$ ($C_{p2} = 2.34 \pm 0.02$, $R^2 = 0.996$, see text), corresponding to next allowed BCC {200}. Dotted line: prediction $\lambda_{p3} = C_{p3}\langle a \rangle/\phi^{1/3}$ with $C_{p3} = 1.88$ for next allowed BCC {211}.

$\lambda_{p1} = C_{p1}\langle a \rangle/\phi^{1/3}$, yielding $C_{p1} = 3.26 \pm 0.02$. Opalescence at longer visible λ_{p1} can be achieved by using USF-NEMs having larger $\langle a \rangle$ yet a similar degree of fractionation. Interestingly, for BMPs having orange and red λ_{p1}, we also observe a smaller population of violet and blue crystallites, respectively, and corresponding smaller secondary peaks λ_{p2} in OBS. We fit the locations of these secondary peaks to a different line (Fig. 3.2c): $\lambda_{p2} = C_{p2}\langle a \rangle/\phi^{1/3}$, yielding

$C_{p2} = 2.34 \pm 0.02$. The ratio of these fitted slopes is $C_{p1}/C_{p2} = 1.393 \pm 0.015$. This measured ratio is very close to $\sqrt{2} \approx 1.41$, so we deduce that λ_{p1} corresponds to first-order Bragg backscattering from certain BCC crystallites aligned with Miller indices {110}, whereas λ_{p2} corresponds to first-order Bragg backscattering from BCC {200} (*i.e.* the same type of BCC crystallites, yet differently oriented). Face-centered cubic (FCC) is effectively ruled out, since the first two allowed Miller indices of FCC would yield a ratio $[C_{p1}/C_{p2}]_{FCC}$ of $2/\sqrt{3} \approx 1.15$, and this would imply a secondary color at much higher λ_{p2} than what is observed. For the very highest observed $\lambda_{p1} = 649$ nm, in addition to $\lambda_{p2} = 460$ nm, we observe a weak peak in the UV at $\lambda_{p3} = 376$ nm (Fig. 3.2c). This λ_{p3} is consistent with the next allowed BCC {211} crystallite orientation (see 3.4 Methods).

To explore the ionic conditions over which xHU biliquid opals and uniformly colored disordered nanoemulsions can be formed, we have diluted USF-NEMs with saline, acidic, and basic solutions and examined the resulting photonic nanodroplet structures (Fig. 3.3). First, using a fractionated USF-NEM having $\langle a \rangle = 39.9$ nm that readily crystallizes after diluting with deionized water, we make the final dilution to the same $\phi = 0.018$ using NaCl salt solutions, yielding a wide range of final $I \approx$ [NaCl]. For final [NaCl] < 8 μM, green-teal crystallites of xHU are observed (Fig. 3.3a and 3.3b); the largest crystallite with spatial dimensions of $L_{max} \approx 2$ mm (Fig. 3.3a, e.g. teal crystallite at final [NaCl] = 4.4 μM) contains approximately $N_{droplet} \approx L_{max}^3/[(4\pi/3)(\langle a \rangle^3/\phi)] \approx 5 \times 10^{11}$ self-assembled nanodroplets. By contrast, for added [NaCl] near but above that value, the repulsion is more highly screened (see schematic in Fig. 3.3a), and we find uniform disordered wj-L structures and increasingly muted colors at higher [NaCl]. For higher [NaCl], the peaks in the observed backscattering spectra become increasingly wide and ultimately

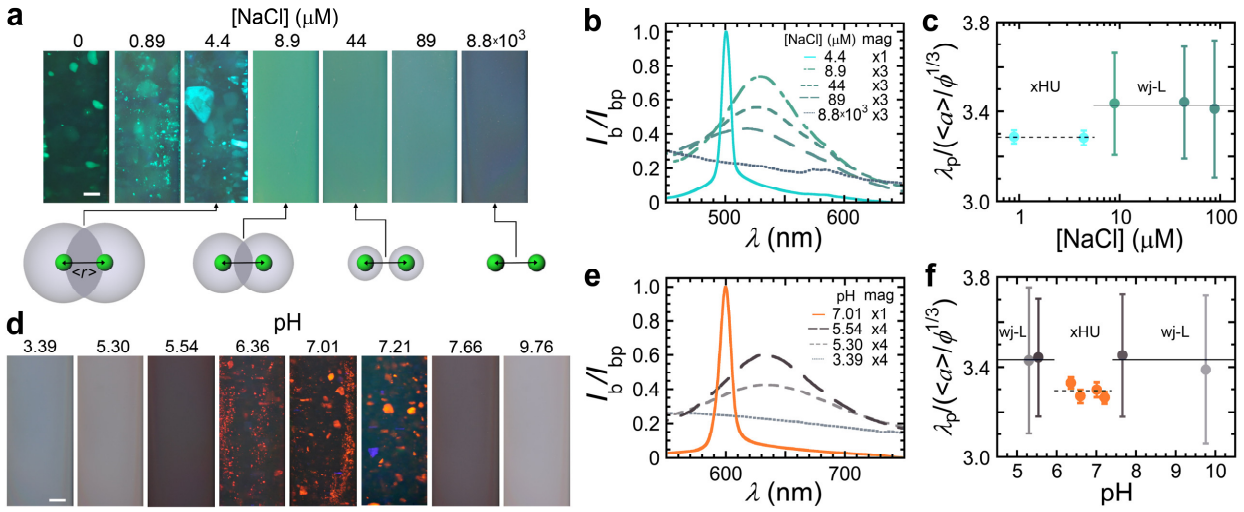

Figure 3.3 Tuning photonic nanodroplet structures through ionic strength *I* and pH in the aqueous continuous phase of ultrastable fractionated nanoemulsions. a, Backscattering macrophotographs (BMPs) of an ultrastable fractionated PDMS O/W nanoemulsion (B2221, $\langle a \rangle$ = 39.9 nm, see Table S3.1) diluted using sodium chloride (NaCl) salt solutions having controlled concentrations [NaCl], yielding the same approximate final $\phi \approx 0.018$ and over a wide range of *I* in the aqueous continuous phase. Monochromatic green crystalline hyperuniform (xHU) biliquid opals are observed at very low [NaCl] < 8 μM (final [NaCl] are above photographs) and less saturated wj-L colors transitioning to a whitish appearance are observed at even higher [NaCl]. White scale bar: 1.0 mm (same for all images). Schematics below certain images (arrows) show pairs of charged nanodroplets (green) at the same $\langle r \rangle$ yet with smaller Debye spheres (gray) as [NaCl] is increased. **b,** Visible backscattering spectra $I_b(\lambda)$ of the nanoemulsions in part a, showing very narrow Bragg backscattering peaks for low [NaCl] corresponding to xHU and much wider peaks for wj-L at high [NaCl]. **c,** Peak wavelengths λ_p (circles) and full-width at half-maximum (FWHM) of the peaks (end-to-end bar length), normalized by $\langle a \rangle / \phi^{1/3}$, as a function of [NaCl], summarizing measured regimes of xHU and wj-L. Horizontal solid line: $C_{\bar{x}} = 3.42 \pm 0.01$ for sj-$\bar{x}$HU and wj-L. Horizontal dashed line: $C_x = 3.29 \pm 0.01$ for xHU. **d,** BMPs of a photonic PDMS O/W nanoemulsion (A121, $\langle a \rangle$ = 59.9 nm, see Table S3.1) after diluting with acidic solutions of hydrochloric acid HCl, neutral deionized water, and basic solutions of sodium hydroxide NaOH having a range of diluent solution pH to the same $\phi \approx 0.035$. For added neutral pH = 7, xHU is observed; however, for slightly acidic and basic solutions, only regimes of wj-L are found. For strongly acidic and basic solutions, further away from neutral pH, hyperuniformity is lost as larger concentrations of hydronium ions [H_3O^+] and hydroxide ions [OH^-], respectively, screen the charge-repulsion between nanodroplets more strongly, ultimately causing droplet unjamming. White scale bar: 1.0 mm (same for all images). **e,** Backscattering spectra for nanoemulsions in part d as a function of pH in the neutral to acidic range. **f,** Summary of λ_p and FWHM from spectra in part e versus pH. Bars and lines have similar meanings and values as in part c.

disappear (Fig. 3.3c). Second, since pH can also significantly influence the equilibrium concentration of the hydronium H_3O^+ and hydroxide ions OH^- in the aqueous continuous phase,

which in turn can affect λ_D, we have also shown that rejamming crystallization, which gives xHU in near-neutral conditions, is hindered for pH outside of a near-neutral range (Fig. 3.3d and 3.3e, $\langle a \rangle$ = 59.9 nm, ϕ = 0.035, see 3.4 Methods). The values of the dimensionless coefficients for the scaled primary peak wavelength $\lambda_p/(\langle a \rangle/\phi^{1/3})$ of the less efficient disordered structures wj-L and more efficient ordered structures xHU (Fig. 3.3f) match those found for a differently sized USF-NEM in Fig. 3.1d.

The growth of crystallites of USF-NEMs through rejamming crystallization is rapid (see Fig. 3.4). Using OBS, we plot the growth of the integrated area under the primary xHU peak, I_a, normalized by its long-time value, $I_{a,\infty}$, as a function of time t (see 3.4 Methods) after diluting and briefly mixing a USF-NEM having $\langle a \rangle$ = 57.9 nm to form a monochromatic xHU biliquid opal at ϕ = 0.039 (see Figs. 3.4a, 3.4b, and 3.4c). The rejamming crystallization, driven by the free energy difference between the disordered droplet configurations and the ordered BCC structure, is amplified by the strong electrostatic repulsion and becomes so rapid that it does not follow first-order simple exponential kinetics. Instead, the normalized intensity growth curve is well described by a two-parameter fit capturing a super-exponential rise to a plateau: $I_a(t)/I_{a,\infty} = 1 - \exp[-(t/\tau)^{\beta}]$, where the characteristic time constant is $\tau = 89 \pm 1$ s and the stretching exponent is $\beta = 1.56 \pm 0.04$ with $\beta > 1$ indicating super-exponentiality ($R^2 = 0.998$). From BMPs, we measure the maximum linear spatial dimension L_{max} of observed growing crystallites (see 3.4 Methods), and this also follows superexponential kinetics: $L_{max}(t) = L_{max,\infty}\{1 - \exp[-(t/\tau)^{\beta}]\}$, where $L_{max,\infty}$ is the long-time value of the largest observed crystallite. Results of this fit yield: $\tau = 172 \pm 2$ s, $\beta = 1.94 \pm 0.04$, and $L_{max,\infty} = 0.720 \pm 0.005$ mm ($R^2 = 0.999$). Thus, the time scale for completion of crystal growth is only several minutes, and these two different physical measures of crystallization both exhibit

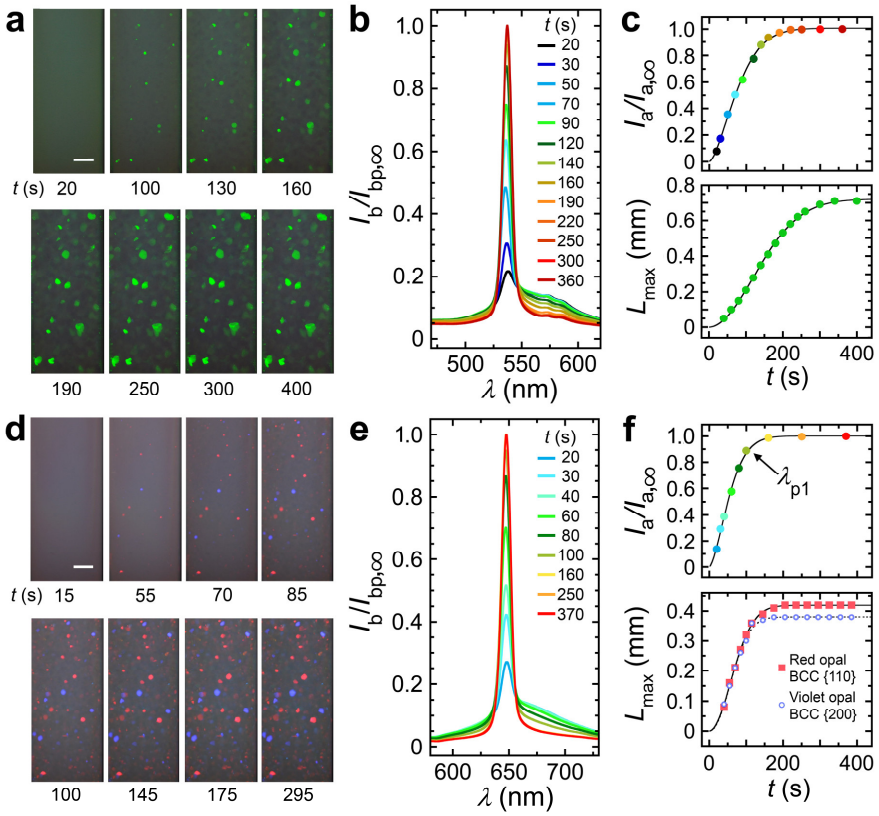

Figure 3.4 Kinetics of crystallite formation in monochromatic and bichromatic biliquid opals following dilution and ultrasonic mixing. a, Backscattering macrophotographs (BMPs) of a monochromatic biliquid opal (A112, $\langle a \rangle$ = 57.9 nm, see Table S3.1) forming at times t (listed below images) after diluting the concentrate to ϕ = 0.039 using deionized water and ending ultrasonic mixing (see 3.4 Methods). White scale bar: 1.0 mm (same for all images). **b,** Backscattering spectra, normalized to the final primary peak intensity at long time, $I_b(\lambda)/I_{bp,\infty}$. Inset (upper right): colors encode observation times t of spectra. **c,** Upper plot: integrated area of the primary peak, I_a, normalized by its long-time value $I_{a,\infty}$, from backscattering spectra (see 3.4 Methods) as a function of t. Symbol colors correspond to times in part b. Solid line: fit of $I_a(t)/I_{a,\infty}$ to a stretched exponential rise to a plateau (see text, R^2 = 0.999). Lower plot: largest spatial dimension of a crystallite, L_{max}, from BMPs (see Methods) versus t. Solid line: fit of $L_{max}(t)$ to a stretched exponential rise to a plateau (see text, R^2 = 0.999). **d,** BMPs of a bichromatic red-violet biliquid opal forming at times t (A121, $\langle a \rangle$ = 59.9 nm, see Table S3.1) after dilution to ϕ = 0.027 and ultrasonication (see 3.4 Methods). Red opalescence corresponds to 1st order Bragg backscattering of BCC {110}; violet opalescence corresponds to BCC {200}. White scale bar: 1.0 mm (same for all images). **e,** $I_b(\lambda)/I_{bp,\infty}$ of the primary red peak for the bichromatic biliquid opal in part d. Inset (upper right): colors encode observation times t of spectra. **f,** Upper plot: $I_a(t)/I_{a,\infty}$ of the primary red peak λ_{p1}. Symbol colors correspond to times in part e. Solid line: fit of $I_a(t)/I_{a,\infty}$ to a stretched exponential rise to a plateau (see text for parameters). Lower plot: $L_{max}(t)$ for red (red solid squares) and violet (violet open circles) crystallites from BMPs (see 3.4 Methods). Solid line: fit of red $L_{max}(t)$ to a stretched exponential rise to a plateau; dashed line: similar fit of violet $L_{max}(t)$ (see text for parameters).

superexponentiality yet with different exponents. For larger $\langle a \rangle$ = 59.9 nm, a similar experiment, diluting to ϕ = 0.027, yields bichromatic red-violet crystallites, and $I_a(t)/I_{a,\infty}$ of the primary λ_{p1} peak exhibits similar superexponential growth kinetics with τ = 64 ± 1 s and β = 1.56 ± 0.05 (R^2 = 0.998). Moreover, by similarly fitting $L_{max}(t)$ of red (BCC {110} orientation) and violet (BCC {200} orientation) crystallites in BMPs (see Fig 3.4f), we extract: τ = 83.3 ± 0.7 s, β = 1.96 ± 0.05, and $L_{max,\infty}$ = 0.419 ± 0.002 mm (R^2 = 0.998) for red, and τ = 78 ± 1 s, β = 2.06 ± 0.08, and $L_{max,\infty}$ = 0.381 ± 0.002 mm (R^2 = 0.996) for violet. The values of β and of τ for this bichromatic xHU from time-resolved OBS and BMPs are nearly the same those for the monochromatic xHU. Kinetics of regrowth of crystallites have also been observed after melting pre-existing xHU crystallites using ultrasound, and the time scale of regrowth is similar to that of initial formation (see Fig. S3.6).

Rejamming crystallization is a complex process that involves simultaneously lowering ϕ, which facilitates transient droplet unjamming and reorganization, and also I, which causes an increase in λ_D associated with electrostatic repulsion and thereby tends to increase jamming and inhibit melting. The interplay between these two effects is further compounded by the much faster ion transport compared to nanodroplet transport, making the non-equilibrium evolution even more complex. To convey this complexity, we have captured time-lapse movies (see 3.4 Methods) that show the appearance and evolution of photonic droplet structures as droplets of USF-NEM concentrates are added to deionized water, as well as the opposite scenario, without homogenization or mixing. Almost immediately, small crystallites grow near the boundary of the concentrate and the deionized water; as these xHU crystallites are convected towards more dilute ϕ, they change color towards longer wavelengths and melt into wj-L. In one striking case, we have

even observed the formation of a long crystallite that has a continuously varying lattice spacing along the gradient in ϕ and I, yielding a continuously varying multi-color single crystallite (see Fig. S3.7). Without mixing or ultrasonication, colorful non-equilibrium states containing spatially distinct sj-x̄HU, xHU, and wj-L regions along the gradient can continue to evolve slowly over many days. For more highly fractionated monodisperse USF-NEMs, the volume fraction of crystallites is large, and crystallites grow until they reach the boundaries of other crystallites. By contrast, additional polydispersity leads to the reduction in the volume fraction of crystallites[29], yet strong photonic colors can still be present at high levels of deionization (see Fig. S3.8). At least to a certain degree nanodroplets which are either too small or too large to be readily incorporated into the crystalline structure are rejected into a continuous disordered matrix that exists outside of the crystallites. For higher ϕ and lower I, his continuous disordered matrix can have a weak solid-like elasticity characteristic of a polydisperse repulsive glass. Once formed, crystallites in biliquid opals are weak elastic solids and do not melt if the cuvette is moved while maintaining a vertical orientation without causing large deflections of the upper meniscus; yet strong agitation or ultrasonication can melt crystallites, which reform different crystallites having the same structure after the agitation ceases.

3.3 Discussion

Photonic nanoemulsions provide a means of creating both tunable three-dimensional hyperuniform diffraction gratings as well as non-crystalline hyperuniform states made up entirely of liquid constituents. When BCC {110} planes are properly oriented, large USF-NEM xHU crystallites strongly Bragg-backscatter a very narrow range of wavelengths, yielding a photonic band gap[5] in a liquid-only composition, and virtually no incident light of that particular peak wavelength is transmitted. Remarkably, color mixing rules so widely taught for optically absorbing

materials (e.g. blue when added to red makes purple) are violated for photonic materials, as we have demonstrated using non-crystalline photonic nanoemulsions (e.g. blue when added to red makes *green*, because the peak wavelength is set by $\langle a \rangle / \phi^{1/3}$, see Fig. S3.9). Such structural color mixing rules would not necessarily apply to solid core-shell systems that have intercore spacings determined by the shell dimension at packing[30], not ϕ as in photonic nanoemulsions, but these structural color mixing rules can be generalized to other dispersions of charged uniform nanoparticulates at high λ_D. While sj-$\bar{x}$HU and xHU have optical spectral signatures that strongly indicate hyperuniformity, performing ultra-small-angle x-ray or neutron scattering (i.e. USAXS or USANS) to examine the behavior at low wavenumbers would further elucidate structural details related to the class of hyperuniformity and the disappearance of hyperuniformity in wj-L. Although we have established protocols and material conditions that yield excellent opalescence in macroscopic volumes, optimizing all parameters, including Δn, which could potentially be done by varying the oil type as well as through compatible additives that are soluble or miscible in the aqueous continuous phase, to achieve the most brilliant opalescence for certain desired wavelengths remains an interesting future direction. Furthermore, going beyond simple ultrasonic excitations, it may be possible to control and manipulate the size and orientation of crystallites by imposing mechanical shear or applying external electromagnetic fields (see Appendix A - Additional discussion). In addition, while we have focused on monodisperse monomodal size distributions, we anticipate that certain bimodal nanodroplet size distributions could yield other crystal structures than BCC, potentially expanding the variety of biliquid opal crystal structures and photonic properties that can be generated through a similar rejamming crystallization process. While our examples of photonic USF-NEMs have involved only anionic stabilizers, it is possible

that cationic stabilizers, such as similarly long alkyl-quaternary ammonium salts, could be readily used instead, leading to cationic O/W biliquid opals.

3.4 Methods

Oil-in-water nanoemulsion production by high flow-rate emulsification. In order to obtain bulk volumes of direct oil-in-water (O/W) nanoemulsions composed of an oil that is highly immiscible with water, we use high flow-rate emulsification (HFRE), generated by a microfluidic homogenizer (Microfluidics M110-P, 75 μm Y-type diamond/stainless steel interaction chamber, liquid pressure setting 30,000 psi ≈ 2 x 10^8 Pa, number of passes N_p = 8), to break up larger microscale droplets of poly-dimethylsiloxane (PDMS, Gelest Inc., average molar mass M_W ≈ 1,250 g mol^{-1}, kinetic viscosity 10 cSt, refractive index n_o = 1.40, mass density ρ_o = 0.935 g cm^{-3}) in a premix emulsion (PowerGen 125S1 rotary mixer, droplet volume fraction $\phi \approx 0.15$) that contains a water-soluble ionic surfactant[23]. Although modern lithographic soft microfluidics can produce very highly controlled monodisperse droplets[17,31,32], the throughput is typically limited and microfluidic homogenizers overcome this limitation albeit at the cost of a higher degree of droplet size polydispersity. The temperature of the emulsification is controlled by immersing the interaction chamber in a tank connected to a recirculating water bath (Thermo Scientific Neslab RTE7). Sodium alkylsulfates represent an important and useful class of water-soluble anionic surfactants. When dissolved in water having pH > pK_a(R-SO_4^-) (where the bound sulfate pK_a is ≈2.5 to ≈3.0 at room temperature $T_r \approx 23$ °C) such that protonation reactions are insignificant, sodium alkylsulfates dissociate resulting in negatively singly charged bound sulfate head groups (R-SO_4^-) and simple saturated hydrocarbon tails (R) with varying carbon number, N_C: sodium dodecyl sulfate (SDS, N_C = 12, Fisher, 99%), sodium tetradecyl sulfate (STS, N_C = 14, Alpha Aesar, 95%), sodium hexadecyl sulfate (SHS, N_C = 16, Alpha Aesar, 99%), and sodium octadecyl

sulfate (SOS, N_C = 18, Acros, 98%). The solubility of SDS in water is large enough over a wide temperature range, including T_r, that hot HFRE is not required to achieve nanoscale emulsions; yet, for $N_C \geq 14$, it is advantageous to perform hot HFRE at T_{HFRE} = 50 °C in order to increase the dissolved concentration of alkylsufate ions in the water, making these amphiphilic ions available for adsorption onto newly created nanodroplet interfaces and also leading to significantly smaller average droplet radius $<a>$ and enhanced stability.

Stability assessment of nanoemulsions made using different alkylsulfate stabilizers after repeated centrifugal deionization. We set all sodium alkylsulfate concentrations to 5 mM when making four separate hot premix PDMS O/W emulsions at $\phi \approx 0.15$, each containing SDS, STS, SHS, and SOS, respectively, and subsequently flow-rupture droplets using hot HFRE at 50 °C to achieve nanoscale $<a>$ (see Fig. 3.1a and Figure S3.1). We first centrifuge the resulting nanoemulsions at 17,400 rpm at T_r for 6 h, generating solid plugs at the tops of the centrifuge tubes (shown as number of centrifugal deionization steps N_{CDI} = 0, see Fig. S3.1). We then cut this plug in half, dilute the lower section with deionized water (≈ 10x), and centrifuge at 17,400 rpm for 6 h (yielding plugs shown at N_{CDI} = 1). We retain all of this plug, dilute it with deionized water and centrifuge again at the same conditions (yielding N_{CDI} = 2). Subsequent steps (e.g. N_{CDI} = 3, ...) repeat the same process. At each step we examine the plugs for macroscopic oil break-out which signals large-scale nanodroplet coalescence, and we record photographic images of the plugs (see Fig. S3.1). Nanoemulsions made using SOS and SHS remain stable even after repeated dilution with deionized water for large N_{CDI}, whereas those made using SDS and STS do not. For stable compositions, rainbow-like multi-colored bands appear at more dilute ϕ and lower I towards the bottoms of the plugs for larger N_{CDI}.

Centrifugal fractionation of polydisperse nanoemulsions. Micellar depletion fractionation[33] is impractical for nanoemulsions because extremely large surfactant concentrations are required; so instead, we centrifugally fractionate[23,24] post-HFRE SDS-stabilized nanoemulsions to reduce their droplet size polydispersities, $\delta a/\langle a \rangle$, where δa is the standard deviation of their droplet size distributions. We load an unfractionated PDMS O/W nanoemulsion ($\phi \approx 0.15$, SDS ≈ 50 mM, ≈1.5 L starting volume) into thick-wall poly-carbonate tubes (capacity ≈ 30 mL each) and centrifuge using a swinging bucket rotor (Beckman L8-55 ultracentifuge, SW28 rotor 6-tube, 18,000 rpm, 17 h) to form soft elastic plugs of dense nanoemulsion cream at the tops of the tubes. Given the mass density difference between the oil and aqueous surfactant solution of $\Delta\rho = \rho_o - \rho_w \approx -0.065$ g cm^{-3}, this centrifugation leads to a gradient in nanodroplet radius that is effectively the same in each plug as a consequence of different steady-state creaming rates. Near the top of a plug, larger nanodroplets predominate, whereas smaller nanodroplets are predominantly toward the bottom. We remove each elastic plug with a thin metal spatula without mixing and cut each plug into three sections (i.e. elastic plug pieces). First, the top 1/4 section of each plug is cut with the spatula and combined with other top sections; this represents the fraction labeled 1. Next, the remaining 3/4 section of each plug is cut in half, and the common sections are combined. The middle section is labeled fraction 2, and the bottom is labeled fraction 3. This process can be repeated as desired by diluting each fraction with [SDS] = 10 mM surfactant solution, thereby setting $\phi \approx 0.15$, and repeating the above centrifugation and sectioning procedures, yielding additional fractionation steps. Typically, 3 or 4 fractionation steps are required to reduce $\delta a/\langle a \rangle$ enough in order to achieve xHU biliquid opals (see Figs. 3.1, 3.2, and Fig. S3.4). Averaged, the typical yield of each fraction in a given fractionation step is about 30% nanodroplet retention. Although jammed disordered nanoemulsions that exhibit weak backscattering colors can be achieved directly from the

nanoemulsion resulting from HFRE without any fractionation, the color saturation becomes much stronger if we have fractionated at least 2 steps. In order to label different fractionated nanoemulsions, we have developed a nomenclature that attaches a unique letter to each polydisperse post-HFRE nanoemulsion, and then a set of successive fraction numbers, using the labels above, for each step (see Table S3.1). For example, the label C211 means a fractionated nanoemulsion that came from a polydisperse post-HFRE nanoemulsion labeled C after a first fractionation step (2- middle fraction), a second step (1- top fraction), and a third step (1- top fraction). The terminal † in a label of a fractionated nanoemulsion indicates that plugs have only been cut in half in each fractionation step: 1 corresponds to the top half, and 2 corresponds to the bottom half.

Hot surfactant exchange of fractionated monodisperse nanoemulsions. In order to reduce the quantities of more expensive alkylsulfates, particularly SOS, used in the rest of our studies as well as to achieve lower $\langle a \rangle$, we first make premix emulsions and perform HFRE using SDS at 50 mM without requiring hot temperatures for pre-mixing and HFRE. Moreover, we can then centrifugally fractionate the resulting nanoemulsions while simultaneously lowering [SDS] yet maintaining stability against coalescence. After nanodroplet size-fractionation is accomplished and [SDS] has been reduced to ≈ 10 mM, we can then mix a fractionated nanoemulsion with an aqueous solution of a sodium alkylsulfate having higher N_C (e.g. SOS) after heating both to 75 °C, causing competitive adsorption/desorption that drives off SDS and populates the droplet interfaces with higher N_C alkylsulfate ions. At room temperature, a fractionated O/W nanoemulsion concentrate ([SDS] ≈ 10 mM) is diluted using deionized water (MilliQ Academic, Millipore Inc., resistivity at T_r: ≈ 18.2 MΩ cm) to reach $\phi \approx 0.15$ and a typical starting volume ≈ 50 mL. Solid SOS is then massed and added to provide [SOS] ≈ 5 mM if fully dissolved and dissociated in the aqueous

continuous phase. This mixture of diluted nanoemulsion and partially dissolved solid SOS is heated to an exchange temperature $T_{exch} \approx 75$ °C in a water bath for 1 hour. At this T_{exch}, the SOS completely dissolves into the aqueous phase, and all octadecyl sulfate anions (OS^-) then become available to adsorb competitively onto the nanodroplets' oil-water interfaces while displacing dodecyl sulfate anions (DS^-), which are less strongly adsorbed and have a significantly higher desorption rate than OS^-. The nanoemulsion is removed from the water bath, allowed to cool back to T_r, loaded into a poly-carbonate centrifuge tube, and is then centrifuged (Beckman L8-55 ultracentrifuge, SW28 rotor, 12,000 rpm, 8 h) to concentrate the nanodroplets into a soft elastic plug. By inserting a spatula between the outer edge of the plug and the inner wall of the poly-carbonate tube and moving the spatula toward the center of the tube, the plug is irreversibly deformed enough to leave a drainage pathway for the aqueous solution below the plug. This aqueous solution, which contains most of the SDS, is drained out of the tube, leaving the elastic plug still attached to the tube's wall. Residual SDS that remains in the continuous phase of this plug can be removed through centrifugal deionization (see below), leaving only OS^- as the stabilizer that is effectively irreversibly adsorbed onto nanodroplet interfaces at T_r.

Centrifugal deionization and formation of nanoemulsion concentrates. To lower the ionic strength I and thereby increase the range of electrostatic repulsion, given by the Debye screening length λ_D, we repeatedly dilute elastic plugs of concentrated fractionated nanoemulsions (stabilized by SOS after surfactant exchange) to $\phi \approx 0.15$ using deioinized water, centrifugally concentrate these diluted nanoemulsions (Beckman L8-55 ultracentrifuge, SW28 rotor, 12,000 rpm, 8 h), remove the lower continuous aqueous solution below the resulting plug by draining (see prior 3.4 Methods section), and retain the elastic plug for a total of N_{CDI} centrifugal deionization

steps. At each N_{CDI}, the electrical conductivity σ_e is measured (Apera Instruments EC400S conductivity meter, brush-resistant platinum black probe): (1) of the nanoemulsion after it has been diluted with deionized water, and (2) of the lower continuous aqueous solution after it is drained (see Fig. S3.2). The decrease in σ_e for both the nanoemulsion and the continuous phase can be described by a decaying exponential function, and a corresponding rise in the Debye screening length λ_D (see caption of Fig. S3.2). After the final N_{CDI}, this plug is called the deionized fractionated nanoemulsion concentrate (see Fig. 3.1b). Its typical volume is ≈ 6 cm^3 for 3 fractionation steps. For adequately low $\delta a/\langle a \rangle$ and appropriate $\langle a \rangle$ and ϕ, when $N_{CDI} \approx 10$, corresponding to $\sigma_{e(2)} < 10$ μS/cm, we observe biliquid opal formation after a final dilution using deionized water (this corresponds also to reported ion concentrations in Fig. 3.3). Leaching of ions from the poly-carbonate tubes is below our meaurement limit, and we cap the stored nanoemulsion concentrate to reduce concentrations of dissolved CO_2 and acidification of the aqueous continuous phase. Nanoemulsion plug-concentrates after draining typically have $\phi \approx 0.4$; if stored for more than one week, we seal these plug concentrates in thickwall polycarbonate centrifuge tubes. This limits CO_2 dissolution in the aqueous continuous phase of the nanoemulsion and reduces acidification. A plug concentrate is then diluted with deionized water (≈2x-3x dilution factor) to obtain the initial volume fraction ϕ_i (see Table S3.1) before making sj-x̄HU, xHU, and wj-L nanoemulsions in a final dilution step with deionized water. This intermediate dilution decreases the elasticity of the nanoemulsion, thereby facilitating the final dilution for small volumes (typically less than 0.1 mL). Centrifugal deionization provides a very systematic, controlled way of reducing I and making a disordered nanoemulsion concentrate at high ϕ, similar in some respects to a prior method of fixing surfactant concentration in the bulk aqueous continuous phase sub-

micron and nanoscale O/W emulsions using repeated centrifugation and dilution with a surfactant solution at a constant concentration[34].

Calculating Debye screening length λ_D from aqueous electrical conductivity σ_e measurements. At each N_{CDI}, we convert the measured σ_e of the drained continuous aqueous phase to ionic strength I using a previously determined calibration curve for SDS (see Fig. 2B on page 10314 in Pagenkopp and Mason, *Langmuir* **34** (2018))[35]. We assume that σ_e in the drained aqueous solution predominantly arises from removed SDS, not SOS. Having monovalent I associated with the continuous phase in the plug-concentrate at each N_{CDI}, we then assume a 20x dilution using deionized water to a final $\phi \approx 0.02$. For each N_{CDI}, after dilution to that same final ϕ, we calculate $\lambda_D = 0.304/I^{1/2}$ (where I has units of M and λ_D has units of nm) at room temperature[26] (see Figure S3.2b). The resulting $\lambda_D(N_{CDI})$ can be reasonably fit using a semi-empirical equation: $\lambda_{D,0}/[1 - (N_{CDI}/N_{CDI}^{\dagger})^{\alpha}]$ for $N_{CDI} < N_{CDI}^{\dagger}$ (see legend of Fig. 3.2b for fit parameters).

Measuring nanodroplet volume fraction in a nanoemulsion concentrate. We accurately determine the initial oil droplet volume fraction ϕ_i of a nanoemulsion using an evaporative gravimetric analytical method that corrects for surfactant mass[36]. The SOS and PDMS are nonvolatile at 23 °C temperature, yet the water is volatile. The mass of water is determined by measuring the mass of ≈ 0.2 g of nanoemulsion concentrate before and after water evaporation (Fisher Scientific vacuum oven model 280, 23 °C, measured pressure under house vacuum ≈ 17 kPa, duration ≈ 24 h) using an analytical balance (Denver Instruments, APX-200 model, 0.1 mg). This causes the nanoemulsion to coalesce into 10 cSt PDMS oil and solid SOS on a plastic weigh boat. Next, the PDMS and SOS mixture are rinsed using a volatile low molar mass solvent

(dimethicone, Gelest, PDMS kinetic viscosity 0.65 cSt) through a filter (filter paper, Whatman 5). After rinsing away all 10 cSt PDMS oil and evaporating all dimethicone in a vacuum oven (≈ 17 kPa, 23 °C, ≈ 12 hours), the mass of solid SOS retained on the filter is measured, and the mass of 10 cSt PDMS is deduced by subtraction. These mass values are converted into volumes by using the known mass densities of 10 cSt PDMS oil and of water, and ϕ_i is subsequently calculated.

Final dilution of nanoemulsion using deionized water. We dilute aliquots of deionized fractionated nanoemulsions, which initially have volume fractions in the range $0.14 \leq \phi_i \leq 0.26$ depending on the particular fraction/name (see Table S3.1), using deionized water to final $0.01 \leq \phi \leq 0.06$. In a polystyrene spectrophotometry cuvette (BrandTech, 1.5 mL semi-micro, outer dimensions 12.5 x 12.5 x 45 mm, inner dimensions 4 x 10 x 20 mm), deionized water is massed (e.g. typical mass), and the concentrated deionized nanoemulsion is added; the mass is again recorded (e.g. typical mass of concentrate). The cuvette is inverted several times until no solid chunks of nanoemulsion are visible, and then the bottom half of the loaded cuvette is immersed in an ultrasonic bath (Branson model 5510, 40 kHz operational frequency, 30 s duration) and ultrasonically agitated at room temperature to ensure that the elastic nanoemulsion concentrate has been fully and homogeneously dispersed. This diffuse ultrasonic excitation by the ultrasonic bath is not strong enough to cause rupturing of nanodroplets, but it does quickly remove inhomogeneities in ϕ.

Backscattering macrophotography. Backscattering macrophotographs (BMPs) are taken using a digital single lens reflex (DSLR) camera (Nikon D5000, 24.5 megapixel 24-bit color RGB detector, XLT extension tube 36 mm length, Nikon DX 18-55 mm zoom lens set to 55, working distance ≈ 10 cm, silent mode); the camera's built-in full-spectrum white light flash serves as a highly directional visible light source in a near-backscattering configuration. A computer equipped

with DigiCam software is connected to the camera and is used to set its mode (M- manual), shutter speed (1/125 s), ISO (200), aperture (f5.6), and exposure compensation e_c ($-2.3 \leq e_c \leq -4.3$) and to take digital images and time-lapse image sequences. The focus is manually controlled to be about 0.3 mm inside the front inner surface of the cuvette, and we estimate the depth of field to be ≈ 0.6 mm. Only when photographing biliquid opals (xHU), the exposure compensation is adjusted to limit saturation in the detector arising from the very bright localized backscattering from crystallites. The location of the flash bulb on top of the camera gives ≈ 12 deg offset from perfect backscattering at 180 deg. Using Bragg's law, we estimate that a factor very close to unity, about 1/sin((180 deg - 12 deg)/2) = 1.006, would be required to correct the observed wavelength in order to obtain the wavelength corresponding to perfect backscattering, so the observed RGB color is not noticeably affected. To reveal angle-dependent iridescence of the biliquid opals (see Fig. S3.3), instead of the built-in flash, we illuminate the biliquid opals at different incident angles using a flexible fiber lamp (Dolan-Jenner Fiber-lite MI-150) that provides a highly directional visible light source.

Optical backscattering spectroscopy. Optical backscattering spectra (OBS) are measured using a digital optical fiber spectrometer (Ocean Optics USB 2000, 0.4 nm spectral resolution, equipped with a R400-7 UV-Vis backscattering fiber optic probe), a computer connected by USB to the spectrometer, and Ocean Optics acquisition software. A full-spectrum incandescent visible light bulb source is turned on and allowed to warm up to achieve a stable steady-state bulb spectrum, which is recorded. The end of the probe is placed against an optical cuvette containing the photonic nanoemulsion of interest; the single central collection fiber is connected to the spectrometer and the outer 6 fiber bundle transmits incident light from the source. The cuvette and probe end of the fiber are completely covered with a matte black curtain to eliminate stray light from other light

sources in the room. The real-time spectrum is displayed on the computer and allowed to stabilize for 10 s, and the backscattering intensity I_b as a function of wavelength λ is recorded. We also measure the backscattering spectra of a cuvette filled with water (i.e. water/cell reference) as well as a cuvette filled with an opaque white concentrated microscale O/W emulsion that highly multiply scatters all visible wavelengths and appears white (i.e. white/cell reference). We use spectra to remove scattering signal emanating from the source scattering off the surface of the cuvette and not the nanoemulsion. In order to more accurately measure OBS of biliquid opals having a primary peak in the ultraviolet (UV, see Fig. S3.5), we illuminated this photonic nanoemulsion using an Ocean Optics ISS UV-Vis light source which has a dedicated UV bulb and provides significantly more UV light than the incandescent visible light source. These backscattering spectra are very different than transmission spectra taken on nanoemulsion concentrates that did not show structural color at much larger I in prior studies[37]. In particular, OBS of biliquid opals show characteristics (i.e. strong peaks and narrow linewidths) that indicate at least a pseudo photonic band gap[5,38,39].

Time-lapse backscattering macrophotography and spectroscopy. To perform time-lapse BMP or OBS, after the final dilution of a deionized fractionated nanoemulsion concentrate to set ϕ, we remove the optical cuvette containing the nanoemulsion from the ultrasonic bath, and this cuvette is continually inverted as the cuvette is transferred to the BMP or OBS apparatus. This continuous inversion causes flow of the nanoemulsion inside the cuvette, thereby inhibiting crystallite growth. The nanoemulsion is placed in front of the fiber optic probe (thus, there is a delay in recording spectra after ceasing ultrasonication of ≈ 10 s to ≈ 30 s). Once the sample inversion has stopped, a stopwatch is started; this sets time t = 0 s for the crystallite growth kinetics studies (see Fig. 3.4). Data for time-lapse BMP and OBS are recorded on the computer every ≈10 s to ≈15 s, respectively.

To obtain out-of-equilibrium time-lapse BMP videos (see Fig. S3.7), the time between frames is also ≈10 s.

Dynamic light scattering: average size and polydispersity of nanoemulsions. We dilute a deionized fractionated nanoemulsion with an aqueous solution of SDS at 10 mM so that ϕ is in the highly dilute single-scattering range: $10^{-4} \leq \phi \leq 10^{-5}$. This SDS solution is used to reduce the Debye screening length so that repulsive interactions are highly screened. The intensity-weighted ensemble-average hydrodynamic radius $\langle a \rangle$ and polydispersity $\delta a/\langle a \rangle$ of this nanoemulsion are obtained from dynamic light scattering (DLS) at room temperature (Photocor FC, laser wavelength λ_{DLS} = 633 nm, scattering angle: 90°, T_r = 23 °C) measurements and cumulant analysis software (Photocor DynaLS).

Zeta potential and electrophoretic mobility of a fractionated nanoemulsion. A portion of a deionized fractionated nanoemulsion concentrate is diluted with 10 mM aqueous solution of sodium chloride to a final droplet volume fraction in the range: $10^{-3} \leq \phi \leq 10^{-4}$. This diluted nanoemulsion is loaded into a specialized electrophoretic light scattering cell, and this cell is placed in a dynamic light scattering system that is equipped for measuring zeta potential (Malvern, Zetasizer Nano ZS). An applied voltage induces electrophoretic motion of charged droplets at an average steady-state propagation speed, which is deduced using dynamic light scattering. From these measurements, the average zeta potential ζ and electrophoretic mobility μ_e of charged nanodroplets in this nanoemulsion are calculated (see Table S3.1 for values).

Analyzing spectra to determine peak wavelength, width, and integrated area. Because the spectrometer provides very fine spectral resolution, peak wavelengths λ_{p1}, λ_{p2} (if present), and λ_{p3} (if present) are determined by wavelengths associated with the maxima in the measured spectra. To determine a peak's width, any underlying residual broadband contribution to the spectrum

around the peak is removed by approximating this underlying trend using a first-order correction (straight line). Then, the full-width at half-maximum (FWHM) intensity of the peak is determined by interpolation, yielding FWHM = $\Delta\lambda$. For sj-$\bar{x}$HU and xHU photonic nanoemulsions, we find that the measured peaks can be reasonably fit using a Gaussian functional form, and its standard deviation σ_λ can be related to the FWHM by: FWHM = $2[2\ln(2)]^{1/2}\ \sigma_\lambda \approx 2.355\ \sigma_\lambda$. The integrated peak area I_a is determined by numerically integrating the region below the measured intensity yet above the linear approximation to any underlying residual contribution.

Bragg backscattering conditions: BCC versus FCC crystals. To interpret the peak wavelengths of backscattered light in terms of crystal structures, we consider two possible crystal structures, body-centered cubic (BCC) and face centered cubic (FCC), that have hard-sphere packing at higher sphere volume fractions, $\phi_{BCC} = 0.680$ and $\phi_{FCC} = 0.740$, respectively[40], than disordered maximal random jamming[27,28,41] at lower $\phi_{MRJ} \approx 0.644$. Simple cubic (SC) is precluded for charge-repulsive nanoemulsions, since it has a lower packing volume fraction $\phi_{SC} = 0.524$ and is therefore less efficient than disordered MRJ structures; moreover, SC is also unstable to repulsive interactions in systems experiencing Brownian excitations. Both BCC and FCC crystal structures have been observed previously in systems of charge-repulsive monodisperse solid colloidal spheres[15]. In a cubic unit cell having edge length L, for BCC there are $N_{BCC} = 2$ spheres per unit cell; whereas for FCC there are $N_{FCC} = 4$ spheres per unit cell. The coordination number, defined as the number of nearest neighboring spheres, is 8 for BCC, whereas it is 12 for FCC. The volume fraction of spheres having radius a in the respective unit cells are: $\phi = N_{BCC}(4\pi/3)a^3/L^3 = (8\pi/3)a^3/L^3$ for BCC; whereas, $\phi = N_{FCC}(4\pi/3)a^3/L^3 = (16\pi/3)a^3/L^3$ for FCC. These relationships can be re-expressed to give the cube's edge length L in terms of a and ϕ, even for repulsive spheres

that are not close-packed and therefore not touching: $L = [(8\pi/3)^{1/3}]a/\phi^{1/3}$ for BCC, whereas $L = [(16\pi/3)^{1/3}]a/\phi^{1/3}$ for FCC. The Bragg condition for optical diffraction of order m in a medium having refractive index n_{eff}, which yields a selected peak wavelength in air of λ_p, is: $m\,\lambda_p = [2d_{hkl}\sin(\theta_{hkl})]n_{\text{eff}}$, where d_{hkl} represent d-spacings between certain periodic crystal planes, and $2\theta_{hkl}$ are scattering angles defined relative to those planes, and h, k, l are non-negative Miller indices, designated by $\{h\ k\ l\}$, corresponding to these planes. The d-spacings in terms of the edge length of the unit cell are: $d_{hkl} = L/(h^2 + k^2 + l^2)^{1/2}$. Only certain values of h, k, l lead to constructive interference for particular crystal structures. For BCC, the first few allowed Miller indices are: {110}, {200}, {211}, {310}, ... ; whereas, for FCC, they are: {111}, {200}, {220}, {311}, ... First order Bragg scattering corresponds to $m = 1$; higher orders $m \geq 2$ would occur in the ultraviolet outside of the visible region. For perfect backscattering, the scattering angle is $2\theta_{hkl} = 180$ deg, relative to transmission at 0 deg, yielding sin(90 deg) = 1. Thus, the 1st order Bragg backscattering condition for the lowest allowed set of Miller indices simplifies to: $\lambda_p = 2n_{\text{eff}}d_{110}$ with $d_{110} = L/2^{1/2}$ for BCC; whereas it is $\lambda_p = 2n_{\text{eff}}d_{111}$ with $d_{111} = L/3^{1/2}$ for FCC. For $\phi << 1$, the effective refractive index can be well-approximated by that of water, so $n_{\text{eff}} \approx n_w = 1.33$ at room temperature. Substituting the appropriate relationships for L in terms of a and ϕ as well as the value of n_{eff}, we obtain $\lambda_p \approx 3.82\ a/\phi^{1/3}$ if the Bragg backscattering is from BCC {110}; whereas, we obtain $\lambda_p \approx 3.93\ a/\phi^{1/3}$ if the Bragg backscattering is from FCC {111}. Although BCC has a lower numerical coefficient than FCC, these coefficients are within 3% of each other, so determining these may not provide a definitive test of structure, given typical experimental uncertainties in a and ϕ. Moreover, considering the next allowed Miller indices for BCC, a secondary peak wavelength corresponding to {200} would be seen at $\lambda_{p2} = \lambda_{p1}/2^{1/2}$, where here λ_{p1} is the primary peak for BCC{110}. By

contrast, for FCC, the secondary peak corresponding to {200} would be seen at $\lambda_{p2} = \lambda_{p1}/(2/3^{1/2})$ where here λ_{p1} is the primary peak for FCC {111}. Thus, if both λ_{p1} and λ_{p2} can be observed spectroscopically by backscattering white light from the same types of crystallites, then the crystal structure can be reasonably differentiated by $\lambda_{p1}/\lambda_{p2} = 2^{1/2} \approx 1.41$ for BCC whereas $\lambda_{p1}/\lambda_{p2} = 2/3^{1/2} \approx 1.15$ for FCC. Using both primary and secondary peaks (i.e. 'indexing' a set of observed peaks based on conditions of constructive interference for particular crystal types) therefore provides a more sensitive means of differentiating BCC from FCC than the absolute coefficients related only to the primary peaks.

Controlling salt concentration and pH. Aqueous solutions of sodium chloride (NaCl, Fisher, 99%, M_w = 58.44 g/mol) are made using deionized water. These solutions vary in concentration from 10 mM to 1.0 μM and are used to dilute a deionized fractionated nanoemulsion to $\phi \approx 0.018$ (see Fig. 3 3a). Hydrochloric acid (HCl, 50% v/v in H_2O, Ricca, M_w = 36.46 g/mol) is diluted with deionized water to makes a series of acidic solutions, $3.39 \leq pH \leq 6.36$. These acidic solutions are used to dilute a deionized fractionated nanoemulsion to $\phi \approx 0.035$ (see Fig. 3.3d). Solid sodium hydroxide (NaOH, Fisher, 99%, M_w = 40.0 g/mol) is dissolved in deionized water to make a 0.1 M stock solution. Serial dilution of this NaOH(*aq*) stock solution with deionized water yields basic solutions, $7.21 \leq pH \leq 10.76$, which are used to dilute the same nanoemulsion concentrate to $\phi \approx 0.035$. The pH of the aqueous acidic and basic solutions are measured using a pH meter (Fisher Scientific Accumet AB150 with Orion 8220BNWP probe), which has been calibrated using buffer solutions over the appropriate ranges of pH..

Appendix A – Supplementary Information for Chapter 3

Additional Discussion

The striking monochromatic and bichromatic biliquid opals that we have made and described herein differ significantly from solid gemstone opals[1-3,42] both in their composition and manner of formation. Biliquid opals have not been produced previously because the necessary combination of physical characteristics, which depend on composition to maintain droplet stability and set small but non-zero $|\Delta n|$, HFRE conditions to achieve nanoscale $\langle a \rangle$, fractionation to reduce $\delta a/\langle a \rangle$, deionization to reduce I and raise λ_D, and dilution to reduce ϕ into a range that leads to spontaneous crystallization that is not kinetically inhibited, had not yet been found. Although monodisperse O/W nanoemulsions have been obtained by fractionation many years ago[23], none of these nanoemulsions had been combined with the ultrastabilization provided by ionic surfactants that have hydrophobic moieties that are extensive enough that these ionic surfactants become essentially irreversibly adsorbed onto nanodroplet surfaces. Such ultrastabilization is necessary in order to reduce the ionic strength down to very low levels that facilitate crystallization by charge repulsion without causing unwanted droplet coalescence. Moreover, it can be particularly advantageous to perform HFRE or surfactant-exchange at hot temperatures, in order to facilitate solubilty and adsorption of such surfactants, and then lower the temperature in order to reduce the surfactant desorption rate dramatically. The experimental approach for ultrastabilizing droplets to very low I that we have introduced for nanoemulsions is generalizable to sub-micron and microscale emulsions. In addition, the classes of surfactant extend beyond sodium alkylsulfates to amphiphilic molecules containing other charge groups and large hydrophobic regions, such as lipids.

Because deformations and reconfigurations of lubricated slippery nanodroplets are possible during centrifugation, precluding coalescence, USF-NEMs provide a flexible system suitable for obtaining biliquid concentrates that can have high ϕ_1 without irreversible aggregation that can occur when some types of dispersions of solid particulates are handled in a similar manner. The mobility of charged surfactant on nanodroplet interfaces provides additional degrees of freedom that could enable non-uniform charge densities on the surfaces of nanodroplets in anisotropic phases for sufficiently strong electrostatic repulsions. This mobility of the charge groups is not present in systems of solid particles that have charges covalently bonded to specific locations on the particle surfaces, and makes the structure and behavior of ionic nanoemulsions potentially different. So, it is non-obvious whether or not the phase behavior and location of phase boundaries of ionic nanoemulsions will be exactly the same for charged nanoemulsions as for charged solid nanoparticles.

Because we have focused on the extreme limit of very low I and large λ_D, we have formed and observed biliquid opals having BCC structures. However, it is possible that for larger I and smaller λ_D that other crystal structures, such as FCC, or even BCC-FCC coexistence, could also be observed in size-fractionated photonic nanoemulsions having larger $<a>$. Our spectroscopically determined structure of BCC for biliquid opals USF-NEMs at $\phi < 0.05$ at very low I is consistent with an extrapolation of the BCC region shown in a phase diagram of colloidal crystals of charged polystyrene nanospheres ('polyballs') determined using x-ray scattering[15], although in this x-ray scattering study the BCC region for polyballs was investigated only for $\phi > 0.05$ at low I. We note that the BCC structure has only 8 nearest neighbors, whereas the FCC structure has 12; so, the electrostatic repulsive energy would be lower for BCC than FCC if the Debye screening length is adjusted such that next-nearest-neighbor repulsive interactions are significantly more highly

screened than nearest neighbor repulsive interactions. Given the millimeter sizes of crystallites of biliquid opals that we can form, we anticipate that it will be possible to perform x-ray scattering studies on single BCC crystals nanodroplets, as has been done for single FCC crystals of solid particutes[43]. By simply substituting deionized D_2O instead of H_2O, we likewise anticipate that neutron scattering studies will be feasible with adequate contrast, thereby enabling structural investigations of crystalline and non-crystalline photonic nanoemulsions. By fluorescently labeling only the oil, super-resolution optical microscopy studies of the anisotropic elasticity of BCC crystals of charged nanodroplets may be possible, to augment what is known for FCC crystals composed of much larger solid microscale colloids[44].

The nucleation and growth process leading to the observed superexponential rise in both the integrated area under the primary backscattering peak in spectra, as well as in the maximum length of observed xHU crystallites in backscattering macrophotography, warrants further attention. By contast to the nucleation and growth of crystallites through intermolecular attractions, such as in supersaturated solutions[45,46], in rejamming crystallization, a non-equilibrium disordered concentrated state of USF-NEMs at a very high osmotic pressure is rapidly decompressed upon significant dilution with deionized; nanodroplet self-organization in the form of crystallization relaxes the system to a lower osmotic pressure facilitated by the greater packing efficiency of the BCC crystalline state compared to a disordered maximally random jammed state. Inadequate dilution leaves the system still in a disordered jammed state (sj-$\bar{x}$HU), and crystallization, which could in princple relax the system, is kinetically suppressed. Thus, determining the boundaries between sj-$\bar{x}$HU, kinetically allowed xHU, and wj-L as a function of ϕ and I for fixed $\langle a \rangle$ theoretically or by simulations, as well as the change in the kinetics of crystallization in xHU close to these boundaries, would be interesting. It is possible that existing understandings of crystal

nucleation and growth in solid colloids[46,47] could potentially be extended to photonic nanoemulsions. Beyond causing melting[48], externally applied excitations, such as large amplitude oscillatory shear[48-50], in excess of Brownian excitations, could potentially facilitate unjamming and strongly impact crystallization through shear-induced ordering near the boundary between sj-$\bar{x}$HU and xHU.

Supplementary Figures

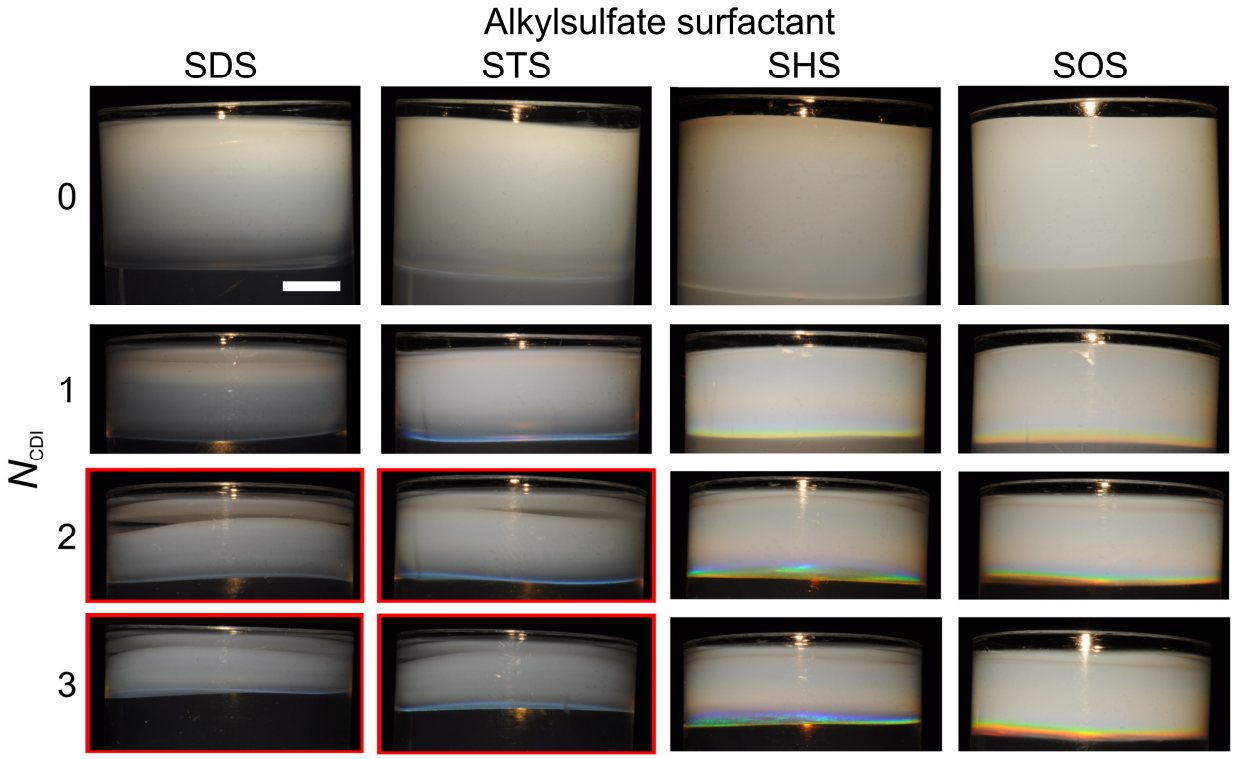

Figure S3.1 Centrifugal deionization probes nanodroplet stability against coalescence for sodium alkylsulfates having different carbon-numbers. PDMS oil-in-water nanoemulsions, made using hot HFRE (see 3.4 Methods) using several different alkylsulfate surfactants (columns: sodium dodecyl sulfate- SDS; sodium tetradecyl sulfate- STS; sodium hexadecyl sulfate- SHS; and sodium octadecyl sulfate- SOS), are repeatedly diluted with deionized water to $\phi \approx 0.15$ and centrifuged at 17,400 rpm for 6 h at room temperature T_r = 23 °C, yielding plugs of dense nanoemulsions at the tops of centrifuge tubes, as shown in backscattering macrophotographs taken immediately stopping the ultracentrifuge. The number of centrifugal deionization steps is designated by N_{CDI} (rows: 0, 1, 2, 3). The effective gravity imposed by the ultracentrifuge points down the page. Scale bar: 5 mm (same for all images). Macroscopic oil break-out at the top of the tube of SDS and STS (designated by red outline boxes) at N_{CDI} = 2 and 3 indicates increasing instability as deionization progresses. By contrast higher carbon-number SOS exhibits the greatest stability, and no oil breakout is seen even up to N_{CDI} = 10. Thus, For SHS and SOS, narrow rainbow-like colored bands can be seen towards the bottoms of the plug, and the colored bands become more intense as N_{CDI} increases. These rainbow colors arise from backscattering diffraction from uniformly spaced small-size nanodroplets at lower ϕ in local bands at the bottoms of the plugs, indicating the inhomogeneous, non-equilibrium gradient in ϕ present in the plug. Here, ϕ decreases towards the bottom of the page (i.e. towards red wavelengths and larger interdroplet separations).

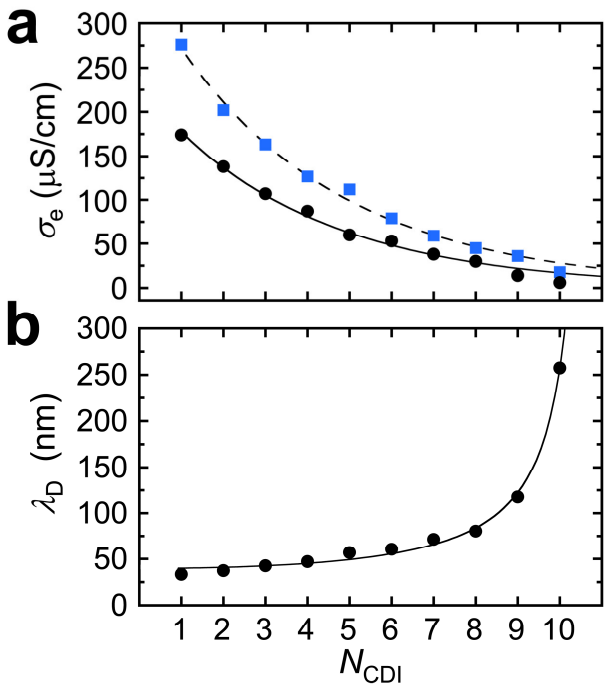

Figure S3.2 Centrifugal deionization decreases the electrical conductivity σ_e of nanoemulsions and their continuous phase solutions. a, After hot surfactant exchange with SOS and immediately before centrifuging, we measure $\sigma_{e,NEM}$ of a fractionated nanoemulsion concentrate (see 3.4 Methods) that has been diluted with deionized water (squares, A211, $\langle a \rangle$ = 47.8 nm, fixed $\phi \approx 0.15$ after each dilution). After centrifuging, we drain the nanodroplet-free clear aqueous solution below the plug (see 3.4 Methods) and measure its $\sigma_{e,soln}$ (circles). We repeat this sequence, keeping track of the number of centrifugal deionization steps, N_{CDI}. These measurements each can be reasonably fit to a decaying exponential function $\sigma_e(N_{CDI}) = \sigma_e^* \exp(-N_{CDI}/N_{CDI}^*)$, where N_{CDI}^* is a characteristic number of centrifugal deionization steps required to drop σ_e by a factor of $e^{-1} \approx 0.368$, and σ_e^* is the initial electrical conductivity before deionization. Owing to the presence of nanodroplets, which include adsorbed OS^- as well as screening Na^+, the conductivity of the nanoemulsion is higher than that of the aqueous solution. Dashed line: fit of squares, yielding $\sigma_{e,NEM}^* = 350 \pm 9$ μS/cm and $N_{CDI,NEM}^* = 4.0 \pm 0.1$ ($R^2 = 0.994$). Solid line: fit of circles, yielding $\sigma_{e,soln}^* = 231 \pm 6$ μS/cm and $N_{CDI,soln}^* = 3.8 \pm 0.2$ ($R^2 = 0.990$). After centrifugal deionization, for σ_e less than ≈10 μS/cm, subsequent dilution of the plug of deionized fractionated nanoemulsion concentrate with deionized water yields biliquid opals if ϕ is in an appropriate range and the degree of fractionation is sufficient (see Fig. 3.1). **b,** Calculated Debye screening length, λ_D, in the aqueous continuous phase after diluting a deionized fractionated nanoemulsion concentrate from part a with deionized water to a final $\phi \approx 0.020$ (see 3.4 Methods). Initial steps of deionization remove SDS both from the continuous phase as well as from droplet interfaces through desorption, so λ_D does not begin to increase much until after the SDS is effectively removed. Line: semi-empirical fit to $\lambda_D(N_{CDI}) = \lambda_{D,0}/[1 - (N_{CDI}/N_{CDI}^\dagger)^\alpha]$ for $N_{CDI} < N_{CDI}^\dagger$, where $\lambda_{D,0} = 40 \pm 3$ nm is the initial screening length before deionization, $N_{CDI}^\dagger = 10.8 \pm 0.1$ marks an effective step related to reduction in conductivity in the continuous phase to ≈0 causing divergence in λ_D, and $\alpha = 2.1 \pm 0.3$ is an exponent that controls the shape of the increase in λ_D at large N_{CDI} ($R^2 = 0.995$).

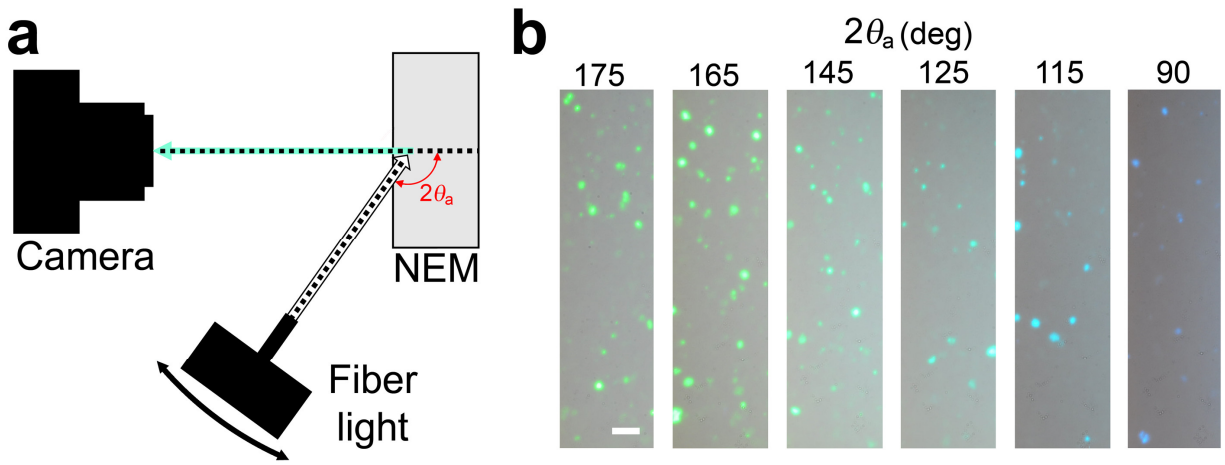

Figure S3.3 Iridescence of biliquid opals. a, Schematic of macrophotographic imaging using a variable-angle broad-spectrum visible illumination provided by a fiber light (see 3.4 Methods). We demonstrate that biliquid opals are iridescent: the color of the crystallites changes with viewing angle relative to the incident directional white light. Iridescence is a direct consequence of the Bragg scattering condition from planes of ordered nanodroplets within crystallites, which predicts an angular color dependence based on coherent optical scattering (see 3.4 Methods). **b,** We observe Bragg-diffracted green-yellow light from crystallites (B121, $\langle a \rangle$ = 48.2 nm, ϕ = 0.019) having a wavelength around ≈565 nm at a near-backscattering 175 deg observation angle, whereas we observe blue-violet light near 420 nm at a 90 deg observation angle. Bragg's scattering condition would predict a factor of sin(45 deg) = $2^{-1/2} \approx 0.71$ in the observed wavelength at 90 deg as compared to 180 deg; this value is close to the observed 420 nm/565 nm ≈ 0.74. Thus, biliquid opals exhibit iridescence similar to that known for solid-state gemstone opals. Scale bar: 1.0 mm (same for all images).

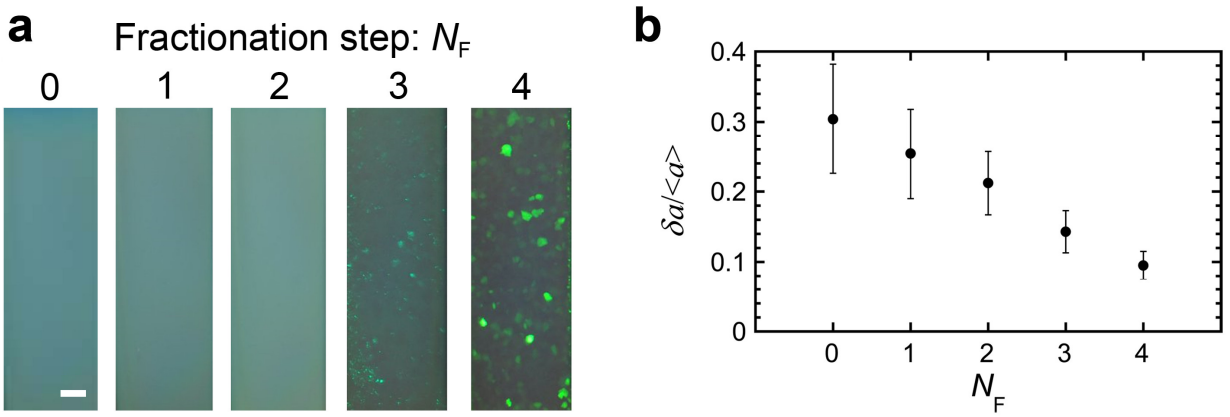

Figure S3.4 Repeated centrifugal fractionation reduces the polydispersities of nanoemulsions produced by multi-pass high flow-rate emulsification. a, Backscattering macrophotographs of deionized nanoemulsion concentrates having varying numbers of fractionation steps, N_F (see 3.4 Methods) after the final dilution using deionized water to set $\phi \approx 0.030$. i.e. in the range where crystallites of xHU are observed at higher $N_F \geq 3$. Fractions have been chosen so that measured $\langle a \rangle$ is approximately constant, near 54 nm: D, D2, D22, D222, D2222 for $N_F = 0, 1, 2, 3, 4$, respectively (see Table S3.1). Scale bar: 1.0 mm (same in all images). **b,** We dilute the deionized nanoemulsion concentrates from part a using an aqueous solution of SDS at ≈10 mM to $10^{-4} \leq \phi \leq 10^{-5}$ and perform several trials of dynamic light scattering (DLS, see 3.4 Methods) to measure average droplet hydrodynamic radius $\langle a \rangle$ and polydispersity $\delta a/\langle a \rangle$, based on cumulant analysis. We find that four fractionation steps are typically required to lower $\delta a/\langle a \rangle$ below ≈ 0.1. Bars represent ± s.d. of polydispersities obtained from multiple DLS trials.

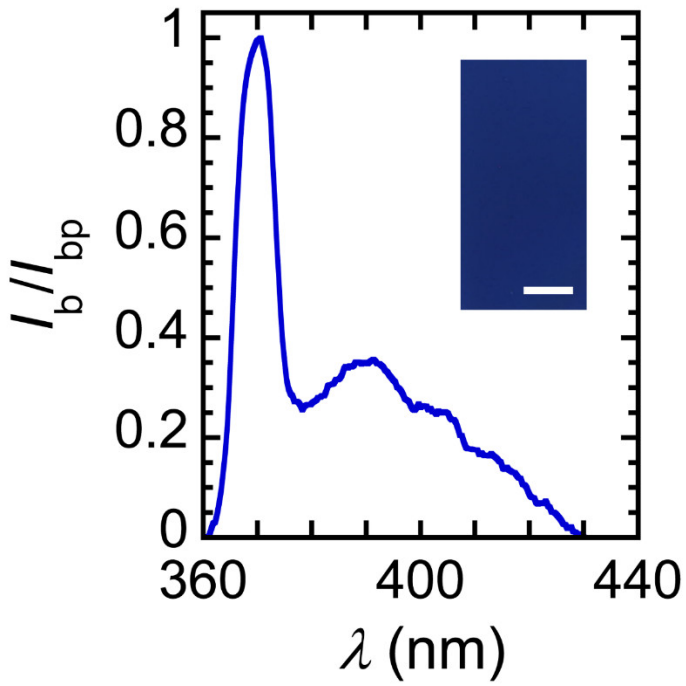

Figure S3.5 Optical backscattering spectrum of a biliquid opal showing a hyperuniform crystalline peak in the ultraviolet. A fractionated nanoemulsion concentrate (A222, $\langle a \rangle$ = 34.1 nm, see Table S3.1) is diluted to ϕ = 0.037 using deionized water. We detect a narrow UV peak at λ_p = 371 nm having FWHM of $\Delta\lambda$ = 10. nm (see 3.4 Methods), indicating crystal formation with a BCC {110} *d*-spacing that corresponds to Bragg backscattering. A broader scattering background is also seen into the visible region accounting for a slight violet appearance (inset: backscattering macrophotograph. Scale bar = 1.0 mm.)

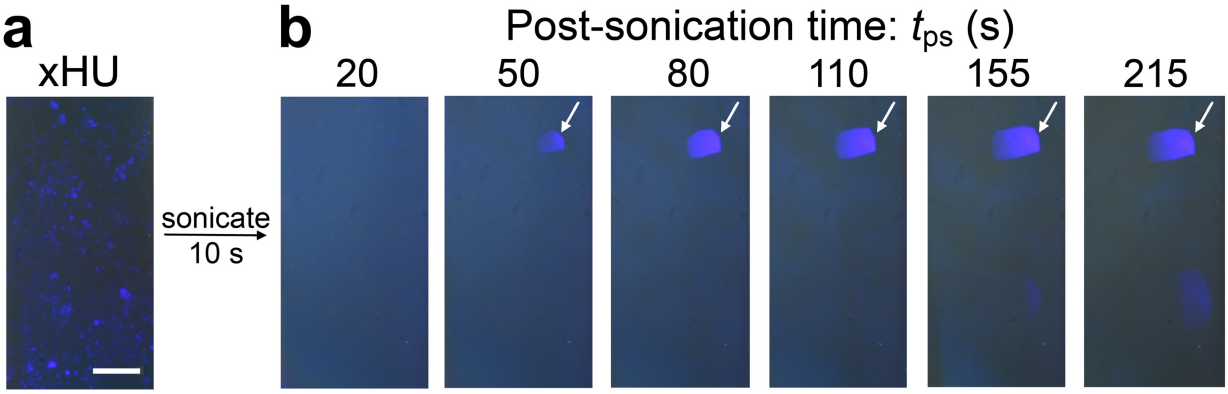

Figure S3.6 Ultrasonic destruction of nanoemulsion crystallites in a biliquid opal and subsequent crystallite regrowth. a, A crystalline xHU nanoemulsion is prepared by diluting a deionized concentrated nanoemulsion (B2222, $\langle a \rangle$ = 37.7 nm, ϕ_i = 0.162) to ϕ = 0.017 and allowing crystallites to grow and jam for a duration of ≈ 200 s. Many small blue-violet crystallites are observed in this stationary initial state. Scale bar = 1.0 mm. **b,** The poly-crystalline nanoemulsion of part a is placed in an ultrasonic bath (see 3.4 Methods, 10 s duration), causing destruction of the crystallites seen in the initial state of part a. Time-lapse backscattering macrophotographs at different post-sonication times, t_{ps}, reveal rapid growth of fewer yet much larger crystallites having the same color in the nanoemulsion. Scale: same as in part a.

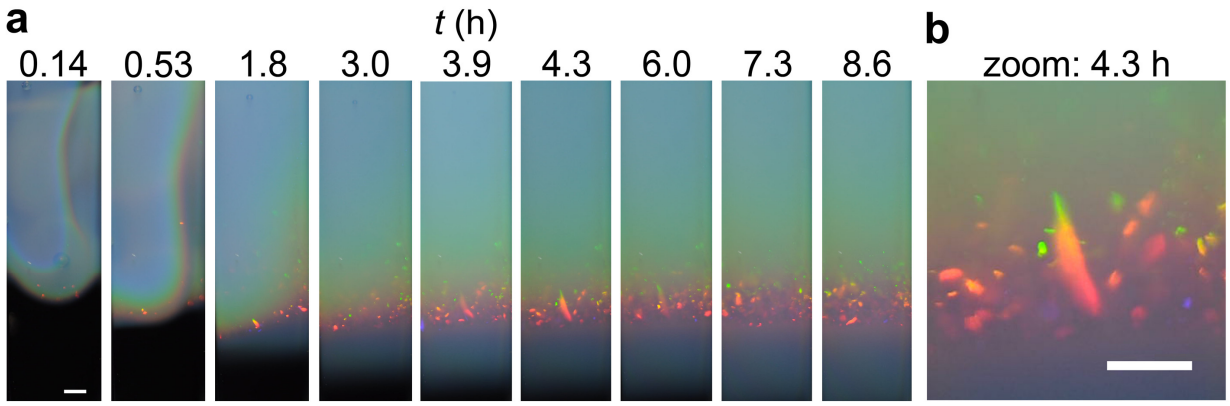

Figure S3.7 Out-of-equilibrium temporal evolution of a deionized fractionated nanoemulsion concentrate that is added to deionized water. a, Backscattering macrophotographs (see 3.4 Methods) are taken at times t after adding the concentrate (C2211, $\langle a \rangle$ = 56.3 nm, $\phi_i \approx 0.219$) from the top of the optical cuvette to the deionized water pre-loaded at the bottom of the cuvette. Almost immediately after adding the concentrate, near the interface of the concentrate and the deionized water, colorful mobile xHU crystallites begin to form and convect. At later times, opalescent crystallites (xHU) as well as colored sj-$\bar{x}$HU and wj-L structures are all apparent as a function of height within the cuvette. Interestingly, within this gradient, we observe a long multi-color crystallite that appears to have a continuously varying color as a function of distance within the spatial gradient in ϕ and ionic strength. The red color at the lower end corresponds to lower ϕ and green color corresponds to higher ϕ. Scale bar: 1.0 mm (same for all images). **b,** Zoomed view of the multi-colored crystallite at t = 4.3 h.

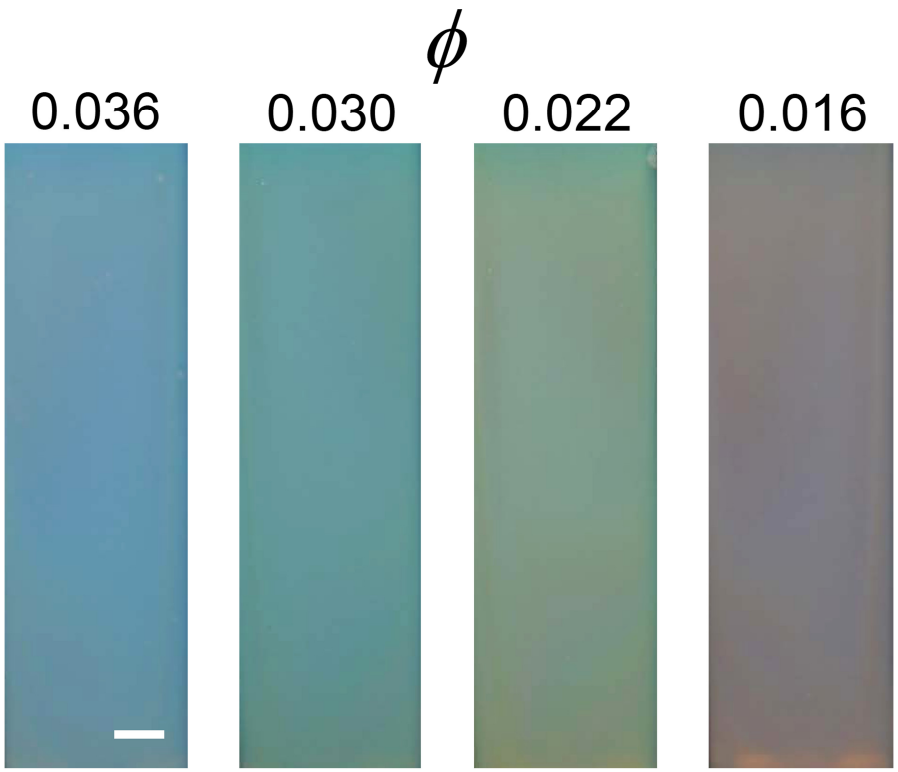

Figure S3.8 Uniform structural colors of polydisperse unfractionated photonic nanoemulsions that remain disordered despite deionization. An unfractionated polydisperse nanoemulsion (D, $\langle a \rangle$ = 54.1 nm, $\delta a/\langle a \rangle \approx 0.3$, see 3.4 Methods, Table S3.1) is surfactant exchanged with sodium octadecyl sulfate and then centrifugally deioinized to obtain a low conductivity in its aqueous continuous phase of $\sigma_e \approx 10$ μS/cm. Upon dilution with deionized water to ϕ that is known to crystallize more monodisperse nanoemulsions, such polydisperse nanoemulsions only exhibit structural colors reminiscent of disordered hyperuniform nanodroplet structures, since the higher degree of polydispersity effectively suppresses crystallization. Different structural colors can be obtained from the same polydisperse nanoemulsion by diluting to different ϕ. White scale bar = 1.0 mm (same for all images).

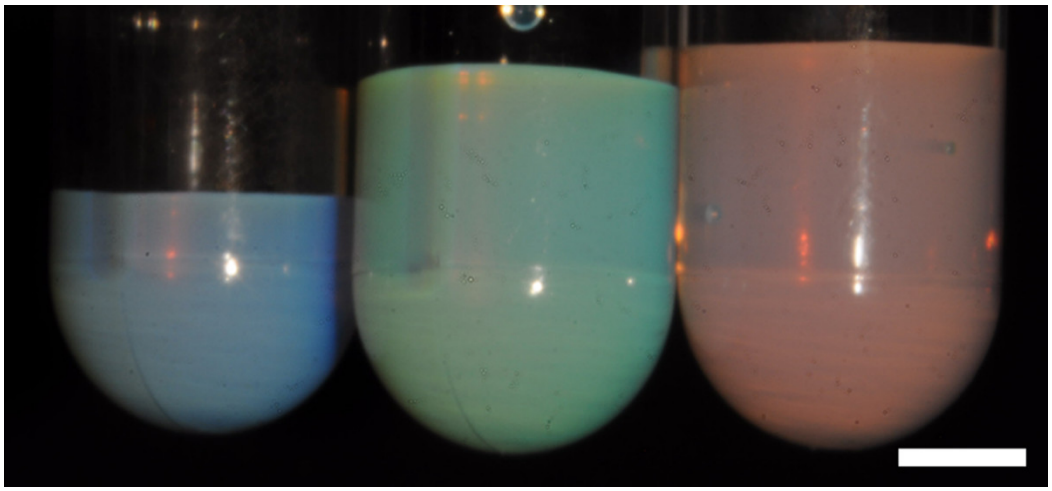

Figure S3.9 Color mixing rules for non-crystalline hyperuniform photonic nanoemulsions violate mixing rules commonly taught for absorbing colors. By selecting ϕ outside the range of crystalline xHU structures, it is possible to obtain strongly colored blue (left, $\phi \approx 0.051$), green (center, $\phi \approx 0.029$), and red (right, $\phi \approx 0.014$) non-crystalline photonic nanoemulsions (B121†, $\langle a \rangle$ = 48.2 nm, see Table S3.1, shown in round poly-carbonate centrifuge tubes) that have uniform, spatially homogeneous optical appearances, as shown in this backscattering photograph. Blue and green colors correspond to sj-$\bar{x}$HU structures, and the red color corresponds to wj-L structure yet very close to the xHU crystalline boundary. Thus, the commonly taught mixing rules for absorbing colors do not apply to photonic nanoemulsions that exhibit structural colors, such as those arising as a consequence of diffraction from disordered yet hyperuniform structures, when observed in backscattering. Remarkably, photonic blue- and red-colored nanoemulsions made from the same deionized fractionated nanoemulsion concentrate, if mixed together in a volume ratio of 40 : 60 (blue nanoemulsion : red nanoemulsion), effectively yield the green-colored nanoemulsion shown, not a purple color as would be the case for optically absorbing materials. Scale bar: 5.0 mm.

NEM fraction	$\langle a \rangle$ (nm)	$\delta a/\langle a \rangle$	μ_e (μm/s)/(V/cm)	ζ (mV)	ϕ_i
A111	64.4 ± 0.5	0.16 ± 0.04	-4.1 ± 0.2	-53 ± 3	0.263 ± 0.005
A112	57.9 ± 0.7	0.13 ± 0.06	-4.4 ± 0.2	-56 ± 4	0.179 ± 0.006
A121	59.9 ± 0.6	0.13 ± 0.04	-4.3 ± 0.1	-55 ± 3	0.149 ± 0.005
A122	53.7 ± 0.4	0.14 ± 0.05	-4.4 ± 0.3	-56 ± 4	0.139 ± 0.007
A211	47.8 ± 0.8	0.13 ± 0.05	-3.9 ± 0.5	-50 ± 7	0.208 ± 0.005
A212	41.5 ± 0.6	0.15 ± 0.06	-3.5 ± 0.2	-45 ± 3	0.179 ± 0.006
A221	39.1 ± 0.3	0.11 ± 0.04	-3.0 ± 0.4	-39 ± 5	0.165 ± 0.006
A222	34.1 ± 0.3	0.14 ± 0.04	-3.3 ± 0.1	-42 ± 1	0.155 ± 0.005
B121[†]	48.2 ± 0.4	0.18 ± 0.03	-3.5 ± 0.1	-45 ± 2	0.181 ± 0.007
B2221	39.9 ± 0.2	0.08 ± 0.02	-3.2 ± 0.1	-43 ± 2	0.173 ± 0.007
B2222	37.7 ± 0.4	0.07 ± 0.03	-4.4 ± 0.2	-56 ± 3	0.162 ± 0.005
C2211	56.3 ± 0.5	0.08 ± 0.03	-3.9 ± 0.2	-50 ± 4	0.219 ± 0.005
D	54.1 ± 0.8	0.30 ± 0.08	-3.4 ± 0.2	-43 ± 2	0.241 ± 0.006
D2	54.2 ± 0.8	0.25 ± 0.06	-3.4 ± 0.1	-44 ± 1	0.233 ± 0.007
D22	53.6 ± 1.3	0.21 ± 0.05	-3.5 ± 0.3	-44 ± 4	0.229 ± 0.007
D222	53.3 ± 0.4	0.14 ± 0.03	-3.5 ± 0.2	-45 ± 3	0.239 ± 0.005
D2222	53.3 ± 0.1	0.10 ± 0.02	-3.4 ± 0.1	-43 ± 1	0.212 ± 0.005

Table S3.1 Characteristics of deionized nanoemulsion concentrates. Each fraction name (left column) begins with a letter designating a particular starting unfractionated nanoemulsion, and provides the sequence of fractionation steps through an ordered list of numbers (see 3.4 Methods). We report average droplet hydrodynamic radii $\langle a \rangle$ and polydispersities $\delta a/\langle a \rangle$, measured using dynamic light scattering (see 3.4 Methods), as well as the average electrophoretic mobility μ_e and zeta potential ζ of constituent nanodroplets (see 3.4 Methods). Uncertainties in $\langle a \rangle$ represent s.d. of the respective means, calculated from cumulant analysis. Uncertainties in $\delta a/\langle a \rangle$, μ_e, and ζ represent s.d. of three trials for each. Initial (i.e. pre-dilution) volume fractions ϕ_i of the concentrates are measured gravimetrically (see 3.4 Methods); uncertainties in ϕ_i represent propagated s.d. using uncertainties of pre- and post-evaporation mass measurements.

References

1. Ward, F. *Opals*. (Gem Book Pub., Bethesda, MD, 2000).
2. Jones, J. B., Sanders, J. V. & Segnit, E. R. Structure of Opal. *Nature* **204**, 990-991 (1964).
3. Sanders, J. V. Colour of Precious Opal. *Nature* **204**, 1151-1153 (1964).
4. Torquato, S. & Stillinger, F. H. Local Density Fluctuations, Hyperuniformity, and Order Metrics. *Phys. Rev. E* **68**, 041113 (2003).
5. Busch, K. & John, S. Photonic Band Gap Formation in Certain Self-Organizing Systems. *Phys. Rev. E* **58**, 3896-3908 (1998).
6. Bragg, W. H. & Bragg, W. L. The Reflection of X-Rays by Crystals. *Proc. R. Soc. Lond. A* **88**, 428-438 (1913).
7. Nassau, K. *Gems Made by Man*. (Chilton, Radnor, PA, 1980).
8. van Blaaderen, A. Opals in a New Light. *Science* **282**, 887-888 (1998).
9. Goodwin, J. W., Hearn, J., Ho, C. C. & Ottewill, R. H. Studies on the Preparation and Characterization of Monodisperse Polystyrene Latices. III. Preparation without Added Surface Active Agents. *Colloid Polymer Sci.* **252**, 464-471 (1974).
10. Stöber, W., Fink, A. & Bohn, E. Controlled Growth of Monodisperse Silica Spheres in the Micron Size Range. *J. Colloid Interface Sci.* **26**, 62-29 (1968).
11. Gasser, U. Crystallization in Three- and Two-Dimensional Colloidal Suspensions. *J. Phys.: Condens. Matter* **21**, 203101 (2009).
12. Gast, A. P. & Monovoukas, Y. A New Growth Instability in Colloidal Crystallization. *Nature* **351**, 553-555 (1991).
13. Li, B., Zhou, D. & Han, Y. Assembly and Phase Transitions of Colloidal Crystals. *Nat. Rev. Mater.* **1**, 15011 (2016).
14. Pieranski, P. Colloidal Crystals. *Contemp. Phys.* **24**, 25-73 (1983).
15. Sirota, E. B. *et al.* Complete Phase Diagram of a Charged Colloidal System: A Synchrotron X-Ray Scattering Study. *Phys. Rev. Lett.* **62**, 1524-1527 (1989).
16. van Blaaderen, A., Ruel, R. & Wiltzius, P. Template-Directed Colloidal Crystallization. *Nature* **385**, 321-324 (1997).
17. Zhu, P. & Wang, L. Passive and Active Droplet Generation with Microfluidics: A Review. *Lab Chip* **17**, 34-75 (2016).

18. Bragg, W. L. & Nye, J. F. A Dynamical Model of Crystal Structure. *Proc. R. Soc. Lond. A* **190**, 474-481 (1947).
19. Goodling, A. E. *et al.* Colouration by Total Internal Reflection and Interference at Microscale Concave Interfaces. *Nature* **566**, 523-527 (2019).
20. Leal Calderon, F., Stora, T., Mondain Monval, O., Poulin, P. & Bibette, J. Direct Measurement of Colloidal Forces. *Phys. Rev. Lett.* **72**, 2959-2962 (1994).
21. Srinivasarao, M., Collings, D., Philips, A. & Patel, S. Array of Air Bubbles in a Polymer Film. *Science* **292**, 79-83 (2001).
22. Fryd, M. M. & Mason, T. G. Advanced Nanoemulsions. *Annu. Rev. Phys. Chem.* **63**, 493-518 (2012).
23. Mason, T. G., Wilking, J. N., Meleson, K., Chang, C. B. & Graves, S. M. Nanoemulsions: Formation, Structure, and Physical Properties. *J. Phys.: Condens. Matter* **18**, R635-R666 (2006).
24. Perrin, J. *Atoms*. (van Nostrand, New York, 1916).
25. Hunter, R. J. *Zeta Potential in Colloid Science: Principles and Applications*. (Academic Press, London, 1981).
26. Russel, W. B., Saville, D. A. & Schowalter, W. R. *Colloidal Dispersions*. (Cambridge Univ. Press, Cambridge, 1989).
27. Liu, A. J. & Nagel, S. R. Jamming is Not Just Cool Any More. *Nature* **396**, 21-22 (1998).
28. Torquato, S. & Stillinger, F. H. Jammed Hard-Particle Packings: From Kepler to Bernal and Beyond. *Rev. Mod. Phys.* **82**, 2633-2672 (2010).
29. Cabane, B. *et al.* Hiding in Plain View: Colloidal Self-Assembly from Polydisperse Populations. *Phys. Rev. Lett.* **116**, 208001 (2016).
30. Magkiriadou, S., Park, J.-G., Kim, Y.-S. & Manoharan, V. N. Disordered Packings of Core-Shell Particles with Angle-Independent Structural Colors. *Optical Mater. Express* **2**, 1343-1352 (2012).
31. Anna, S. L., Bontoux, N. & Stone, H. A. Formation of Dispersions Using Flow Focusing in Microchannels. *Appl. Phys. Lett.* **82**, 364-366 (2003).

32. Thorsen, T., Roberts, R. W., Arnold, F. H. & Quake, S. R. Dynamic Pattern Fomation in a Vesicle-Generating Microfluidic Device. *Phys. Rev. Lett.* **86**, 4163-4166 (2001).
33. Bibette, J. Depletion Interactions and Fractionated Crystallization for Polydisperse Emulsion Purification. *J. Colloid Interface Sci.* **147**, 474-478 (1991).
34. Mason, T. G., Krall, A. H., Gang, H., Bibette, J. & Weitz, D. A. Monodisperse Emulsions: Properties and Uses. In *Encyclopedia of Emulsion Technology* Vol. 4 (ed. P. Becher) 299-336 (Marcel Dekker, New York, 1996).
35. Pagenkopp, M. J. & Mason, T. G. Surfactant Partitioning in Nanoemulsions. *Langmuir* **34**, 10309-10320 (2018).
36. Zhu, X., Fryd, M. M., Huang, J.-R. & Mason, T. G. Optically Probing Nanoemulsion Compositions. *Phys. Chem. Chem. Phys.* **14**, 2455-2461 (2012).
37. Graves, S. M. & Mason, T. G. Transmission of Visible and Ultraviolet Light Through Charge-Stabilized Nanoemulsions. *J. Phys. Chem. C* **112**, 12669-12676 (2008).
38. John, S. Strong Localization of Photons in Certain Disordered Dielectric Superlattices. *Phys. Rev. Lett.* **58**, 2486-2489 (1987).
39. Yablonovitch, E. Inhibited Spontaneous Emission in Solid-State Physics and Electronics. *Phys. Rev. Lett.* **58**, 2059-2062 (1987).
40. Kittel, C. *Introduction to Solid State Physics*. 8th edn. (Wiley, New York, 2005).
41. Bernal, J. D. & Mason, J. Packing of Spheres: Co-Ordination of Randomly Packed Spheres. *Nature* **188**, 910-911 (1960).
42. Sanders, J. V. Diffraction of Light by Opals. *Acta Cryst. A* **24**, 427-434 (1968).
43. Vos, W. L., Megens, M., van Kats, C. M. & Bösecke, P. X-ray Diffraction of Photonic Colloidal Single Crystals. *Langmuir* **13**, 6004-6008 (1997).
44. Reinke, D. *et al.* Noncentral Forces in Crystals of Charged Colloids. *Phys. Rev. Lett.* **98**, 038301 (2007).
45. Karthika, S., Radhakrishnan, T. K. & Kalaichelvi, P. A Review of Classical and Nonclassical Nucleation Theories. *Cryst. Growth Des.* **16**, 6663-6681 (2016).
46. Sear, R. P. Nucleation: Theory and Applications to Protein Solutions and Colloidal Suspensions. *J. Phys.: Condens. Matter* **19**, 033101 (2007).

47. Herlach, D. M., Palberg, T., Klassen, I., Klein, S. & Kobold, R. Overview: Experimental Studies of Crystal Nucleation: Metals and Colloids. *J. Chem. Phys.* **145**, 211703 (2016).
48. Imhof, A., van Blaaderen, A. & Dhont, J. K. G. Shear Melting of Colloidal Crystals of Charged Spheres Studied with Rheology and Polarizing Microscopy. *Langmuir* **10**, 3477-3484 (1994).
49. Ackerson, B. J. & Pusey, P. N. Shear-Induced Order in Suspensions of Hard Spheres. *Phys. Rev. Lett.* **61**, 1033-1036 (1988).
50. Kim, H. S. & Mason, T. G. Advances and Challenges in the Rheology of Concentrated Emulsions and Nanoemulsions. *Adv. Colloid Interface Sci.* **247**, 397-412 (2017).

Chapter 4 - Summary and Future Directions

This dissertation has demonstrated the versatility and advantages of using size-fractionated nanoemulsions, compared to more common polydisperse nanoemulsions. This high surface area meta-stable material has great potential for more exciting academic research opportunities. As in almost all endevors in science, there is always room to grow and new avenues to explore.

In chapter 2, we present a new direct method to quantify the thermodynamic partitioning of sodium dodecyl sulfate surfactant molecules in an oil-in-water poly(dimethylsiloxane) nanoemulsion. The creation of new interfacial area drives more surfactant to adsorb onto the interface which, in the case of nanoemulsions, means a larger fraction of the total surfactant can be consumed in this process. This can cause the final bulk surfactant concentration to be much less than the initial surfactant concentration. We have shown that using a size-fractionated nanoemulsion yields more accurate results than an unfractionated nanoemulsion. The partitioning of sodium dodecyl sulfate can be sufficiently described by Langmuir adsorption and we have provided a theory to this effect written in terms which are pertinent to emulsion science.

In princple, these methods can be modified to accomidate other ionic sufactant and oil combinations, as long as the surfactact is insouble in the oil. It is also concievable that a variation of the separation technique, used to quanitfiy [SDS], could be modified to work with non-ionic sufactants as well. Along with studing other surfactants, studying surfactant partitioning while varying the concentration of a surface inactive salt (e.g. sodium chlordie) would be very insteresting.

In chapter 3, we describe different routes to obtain photonic nanoemulsions which can self-assemble into intensely colored biliquid opals. By using an alkyl sulfate surfactant with a long

hydrophobic chain, we create ultra-stable nanoscale droplets which do not coalesce when dispersed or concentrated in an aqueous phase with a low ionic strength. After several deionization steps, the Debye length has increased to be larger than the droplet radius. These poorly screened droplets are able to self-assemble to form large scale (mm) crystallytes or a non-crystalline hyperuniform state where the nanoemulsion can still scatter visible light and appear to be an intense monochromatic color.

It is still not clear if all of the variables that produced this color (refractive index difference between the disperse phase and continuous phase) are truly optomized to yield the most intesne and brilliant result. While we have demonstrated control over the color of the crystals produced (primarily dependant on $<a>$, I, and ϕ), we have not demonstrated the same level of control over the size and oreintation of the crystallites. It maybe possible to influence these factors through externally applied forces (e.g. mechanical shear and electromagnetic). It would also be interesting to explore if other crystal structures could be accessed by mixing droplets with different $<a>$ in different ratios.